EXTRACTING THE ASYMPTOTIC NORMALIZATION COEFFICIENTS IN NEUTRON TRANSFER REACTIONS TO DETERMINE THE REACTION RATES FOR ^{22}Mg(p,γ)^{23}Al AND ^{17}F(p,γ)^{18}Ne

A Dissertation

by

TARIQ ABDALHAMED AL-ABDULLAH

Submitted to the Office of Graduate Studies of
Texas A&M University
in partial fulfillment of the requirements for the degree of

DOCTOR OF PHILOSOPHY

August 2007

Major Subject: Physics

EXTRACTING THE ASYMPTOTIC NORMALIZATION COEFFICIENTS IN NEUTRON TRANSFER REACTIONS TO DETERMINE THE REACTION RATES FOR ^{22}Mg(p,γ)^{23}Al AND ^{17}F(p,γ)^{18}Ne

A Dissertation

by

TARIQ ABDALHAMED AL-ABDULLAH

Submitted to the Office of Graduate Studies of
Texas A&M University
in partial fulfillment of the requirements for the degree of

DOCTOR OF PHILOSOPHY

Approved by:

Chair of Committee,	Carl A. Gagliardi
Committee Members,	Robert E. Tribble
	Joseph B. Natowitz
	Che-Ming Ko
Head of Department,	Edward Fry

August 2007

Major Subject: Physics

ABSTRACT

Extracting the Asymptotic Normalization Coefficients in Neutron Transfer Reactions to Determine the Reaction Rates for ^{22}Mg(p,γ)^{23}Al and ^{17}F(p,γ)^{18}Ne.

(August 2007)

Tariq Abdalhamed Al-Abdullah, B.S., Yarmouk University;

M.S., Yarmouk University

Chair of Advisory Committee: Dr. Carl A. Gagliardi

The nucleosynthesis of the β^+-unstable ^{18}F and ^{22}Na nuclei in oxygen-neon novae is considered one of the crucial subjects in the field of nuclear astrophysics. They are produced in thermonuclear runaway processes via radiative proton-capture reactions and may be ejected into the stellar medium when the sudden outbursts of the envelope occur. Recent observations with γ-ray telescopes, however, have not detected those long-lived γ-ray emitters.

The problem is to study the importance of the rates of the ^{17}F(p,γ)^{18}Ne and ^{22}Mg(p,γ)^{23}Al reactions that may influence the abundances of ^{18}F and ^{22}Na, respectively. To investigate their productions, an indirect technique has been applied to determine these reaction rates at stellar energies through measurements of the asymptotic normalization coefficients (ANCs) in the mirror nuclear systems. The ANCs for ^{18}O and ^{23}Ne are obtained from the neutron transfer reactions ^{13}C(^{17}O, ^{18}O)^{12}C and ^{13}C(^{22}Ne, ^{23}Ne)^{12}C at 12 MeV/nucleon, respectively. The ANC of ^{13}C, which represents the other vertex in the transfer reactions, has also been measured to be $C^2_{p_{1/2}} = 2.31 \pm 0.08$ fm^{-1}.

The differential cross-sections for the reaction ^{13}C(^{22}Ne, ^{23}Ne)^{12}C because of transi-

tions from the $J^\pi = \frac{1}{2}^-$ in ^{13}C to the $J^\pi = \frac{5}{2}^+$ and $\frac{1}{2}^+$ states in ^{23}Ne, have been detected. Optical model parameters for use in the DWBA calculations were obtained from measurements of the elastic scatterings ^{22}Ne+^{13}C and ^{22}Ne+^{12}C at the same energy. The extracted ANCs in ^{23}Ne are transposed to their corresponding values in ^{23}Al. The astrophysical S-factor $S_{1-22}(0)$ was determined to be 961 ± 105 eV b. The reaction rate calculated from these results shows that the ^{22}Mg(p,γ)^{23}Al reaction may reduce the production of ^{22}Na in massive novae M ≈ 1.35 M$_\odot$.

A similar procedure has been followed in studying the ^{13}C(^{17}O, ^{18}O)^{12}C reaction. The ANCs related to the $J^\pi = (0^+_1, 2^+_1, 4^+_1, 2^+_2)$ states in ^{18}Ne were determined from their corresponding values in ^{18}O, then used to calculate $S_{1-17}(0) = 2.5 \pm 0.4$ keV b. These results show that the reaction rate of ^{17}F(p,γ)^{18}Ne is dominated by the direct capture to the 2^+_2 and 2^+_1 states at astrophysical energies. The calculated reaction rate is considered to be slow, which leads to an increase in the production of ^{18}F in oxygen-neon novae.

To my father and my mother

ACKNOWLEDGMENTS

I would like to express my sincere gratitude to Prof. Carl A. Gagliardi who has been a very generous and fair advisor. He has provided me with knowledge, encouragement, and support that assisted me to earn this Ph.D. He gave me the opportunities to interact with many researchers around the world and build several relationships that may open the door to improve my career in the future. His bright and creative way of thinking and addressing several important research issues inspired me all the time. It was my fortune and pleasure to work under his supervision.

I also would like to convey my special thanks to Prof. R. E. Tribble for his advice, guidance, and help, and Profs. J. Natwoitz and Che-Ming Ko for serving as committee members and for their valuable input to this work.

I would like to express my grateful appreciation to Prof. L. Trache for his patience and tremendous support throughout my study years. He is a very nice, great, and gracious person who shared his experience with me and showed me the proper ways to solve the difficulties in my research. A similar vote of thanks and appreciation goes to Prof. Florin Carstoiu who has done the theoretical part of the research, and Dr. G. Tabacaru for his great help.

I would like to extend my thanks to the MDM group, Dr. Y.-W. Lui, Dr. H. Clark, Dr. Y. Tokimoto, and Mr. X. Chen for their nice cooperation and generous help in preparing the experimental setup. Special thanks are due to my friends and collaborators, Dr. C. Fu and Mr. Y. Zhai.

I would like to express my gratitude to the Hashemite University for their sponsorship and providing me the option to pursue my Ph.D at Texas A&M University. I also gratefully appreciate the financial support that I received from the Robert A. Welch Foundation for five consecutive years.

TABLE OF CONTENTS

CHAPTER Page

LIST OF TABLES

LIST OF FIGURES

FIGURE Page

FIGURE Page

FIGURE Page

FIGURE Page

FIGURE Page

CHAPTER I

INTRODUCTION

Exploring the universe is as old as human kind. Four thousand years ago the Babylonians were known for their prediction of the position of the planets, the motion of the stars, and dates of eclipses. But the first model to describe the dynamics in the sky was built by Ancient Greeks, and then developed by Ptolemy and Copernicus in the following centuries. The inquiry about understanding the origin of the universe and its ultimate destination emerged in the twentieth century when Georges Lemaitre proposed in 1927 that the universe began with a tremendous explosion known as the big-bang, where all matter and energy were contained at a point. In 1929, Edwin Hubble's observations supported Lemaitre's theory when he noticed that the spiral nebulae are not local objects but autonomous groups of stars. He discovered that each galaxy takes the same amount of time to move from a specific starting point to its current position. This term of expansion formed the basis of the big-bang nucleosynthesis (BBN) of the primordial matter. BBN involves an event that happened at energies of order few MeV. Therefore, it is naturally essential to make a connection between cosmology and nuclear and particle physics to study the processes of the reactions that occur in stellar evolution systems, such as novae and supernovae, and cause the abundances of more than two thousand nuclei. This dissertation is a report on the determination of two particular nuclear reaction rates, chosen from many others to interpret the nucleosynthesis of specific nuclei in oxygen-neon nova events.

This dissertation follows the format of the journal Physical Review C.

A. The Nucleosynthesis of Elements

The framework for understanding the abundances of chemical elements in the stars and interstellar material is the evolution of the various constituents of the early universe. The study began with the pioneering work of Gamow and his associates in 1940 [1] when they recognized the significance of the hot big-bang in producing all the elements in the periodic table. The Gamow model imagined that the early stage of the matter was a highly degenerate neutron gas. As the pressure decreased due to the universal expansion, neutrons decayed into protons and electrons. The protons could then capture neutrons and build-up light then heavier elements. However, this assumption was invalid. The primeval fireball stage ($T = 10^{12}$ K) began when the particles and the high-energy photons in the plasma were in chemical equilibrium. The presence of energetic leptons, neutrinos and antineutrinos, changed protons and neutrons into each other via the reactions

$$\overline{\nu}_e + p \rightleftharpoons e^+ + n \tag{1.1}$$

$$\nu_e + n \rightleftharpoons e^- + p \tag{1.2}$$

$$n \rightleftharpoons e^- + p + \overline{\nu}_e. \tag{1.3}$$

At this stage, all nucleonic matter was free and the universe was in baryonic charge symmetry. The initial number of neutrons per proton in thermal equilibrium is given by the Saha equation

$$\frac{n}{p} \approx exp(-\Delta mc^2/kT) \tag{1.4}$$

with $\Delta mc^2 = 1.293$ MeV, the mass difference between neutron and proton. As the universe expanded , the temperature dropped down. When the temperature decreased to 10^{11} K, the weak interactions in Eq. (1.1) and (1.2) suddenly switched

off. At $T = 10^9$ K, the photons no longer had sufficient energy to generate new electron-positron pairs. Hence, the neutron-to-proton ratio fell out of equilibrium. One second after the big bang a significant fraction of neutrons were left at the freeze-out temperature, $T_9 \approx 7.5$ (in units of 10^9 K) [2]. Substituting in Eq. (1.4), it follows that the relative amount of neutrons to protons, 13% n and 87% p, is nearly fixed from there on.

Although the rate for neutrons and protons to collide and form deuterons is rapid,

$$n + p \rightarrow d + \gamma, \tag{1.5}$$

the low binding energy of 2.22 MeV for the deuteron and their very small density compared with the density of photons [3] resulted in an instantaneous photodisintegration that prevented nuclear reactions from building-up other nuclei. The BBN was delayed until the temperature fell to $T_9 \approx 1$, when further n, p, and d reactions led to the abundance of light elements ^{3}H, ^{3}He, ^{4}He, and ^{7}Li in the sequence shown in Fig. 1.

The success of the standard BBN model in presenting an explanation for the abundance of He, in agreement with the observed mass fraction 0.26 ± 0.04 [4], as well as the abundance of d [3], provides strong support for this model. On the other hand, making all the elements during BBN was blocked by the lack of stable nuclei of mass 5 and 8. In addition, the fast decrease of the thermal energies due to the expansion implied that highly charged nuclei could not overcome their Coulomb repulsion. An environment of higher densities and longer lifetime were required. Thus, the BBN scenario does not account for the production of elements beyond ^{7}Li, but the nuclei already formed are used as tracers in the study of the chemical evolution.

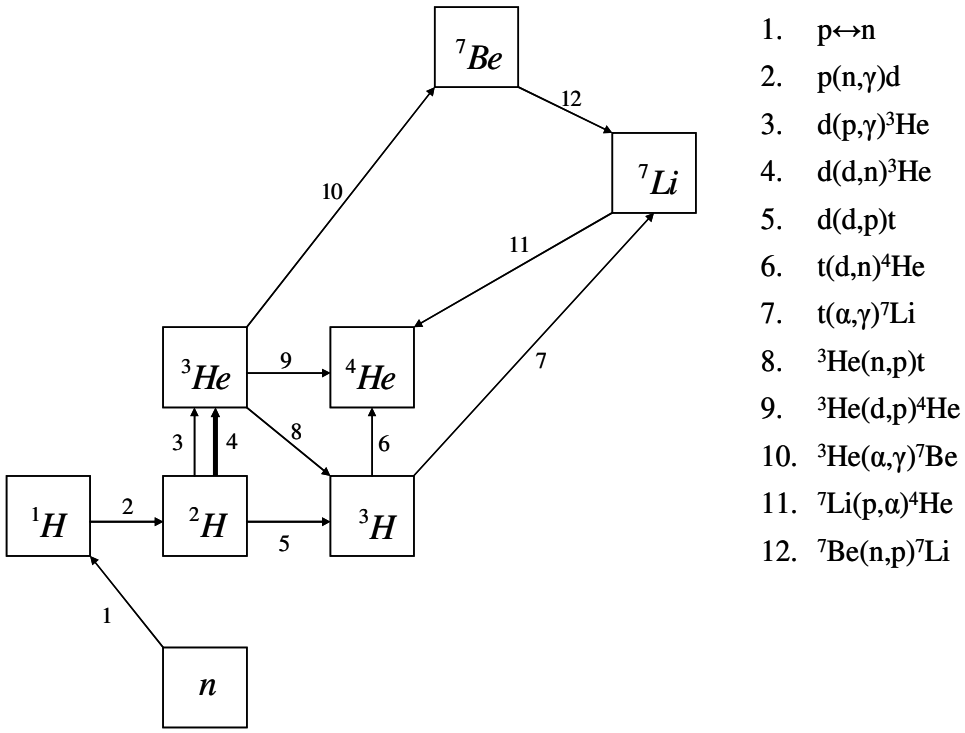

FIG. 1. The reaction network that leads to the synthesis of light nuclei in standard BBN.

When the temperature decreased below 5000 K, the atomic nuclei combined with the electrons to create neutral hydrogen gas. The formation of H_2 via the following reactions cooled the gas clouds to 1000 K and increased the gas density

$$H^- + H \rightarrow H_2 + e^- \tag{1.6}$$

$$H + e^- \rightarrow H^- + \gamma. \tag{1.7}$$

Under appropriate conditions [5], fluctuations in the density of the homogeneous clouds produced a net gravitational force that enabled the clouds to collapse and condense to form the first generation objects, which are named population III stars [6]. Those stars may have been quite massive ($\sim$ 100-300 $M_\odot$) [7] with very high temperature. Due to their short lifetimes, they might have ended as energetic super-

nova events, or giant thermonuclear events, which enriched the intergalactic medium by ejecting all the heavy elements that they previously synthesized in their stellar interiors.

Since hydrogen is the most abundant element, the main mechanism for the energy-production in stars comes from converting hydrogen into helium. In population III stars, the fusion process is dominated by the proton-proton (pp) chain of reactions, where the basic process to burn the hydrogen is

$$4p \rightarrow {}^4\mathrm{He} + 2\beta^+ + 2\nu. \tag{1.8}$$

The high nuclear binding energy for the reaction, 26.73 MeV, indicates that the chain must go through a series of steps to produce helium. The process starts with the spontaneous weak decay of a proton in the field of a second proton

$$p + p \rightarrow d + e^+ + \nu, \tag{1.9}$$

which is followed by the fast and strong interaction

$$p + d \rightarrow {}^3\mathrm{He} + \gamma. \tag{1.10}$$

Then, depending on the temperature of stars, the conversion process proceeds through three possible paths to generate ^{4}He isotopes as shown in Fig. 2, where the PPI chain occurs at the lowest temperature and does not create nuclei heavier than helium. The remaining two branches generate elements up to beryllium. The total amount of energy released from any pp chain is 26.73 MeV. The fraction of the energy lost entirely from the stars for PPI, PPII, and PPIII are 2%, 4%, and 28%, respectively. The substantial energy output in neutrinos makes the PPIII chain an important source for the neutrino flux in the main sequence stars [8].

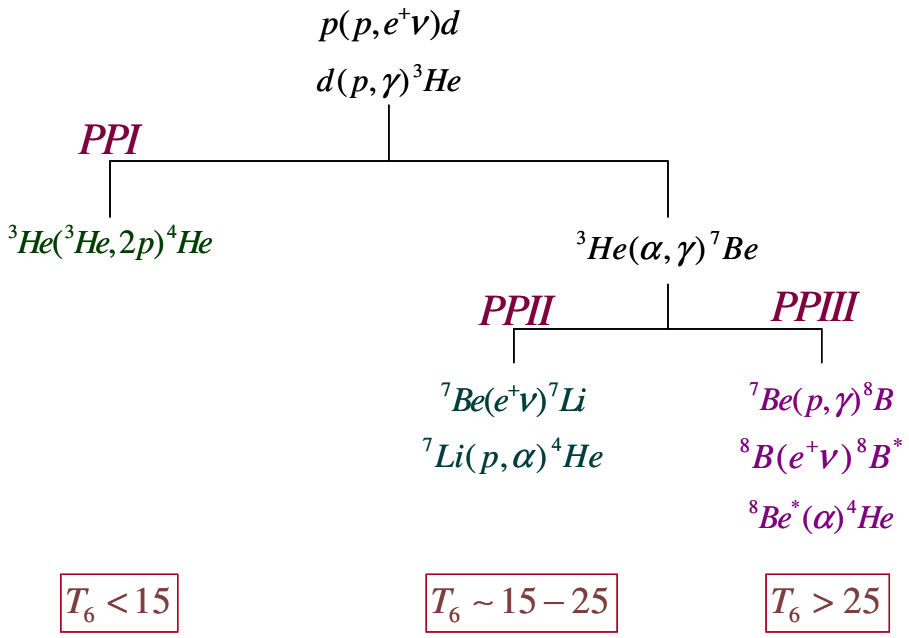

FIG. 2. A diagram shows the three pp chains of reactions, where the net result is to produce alpha particles from the fusion of four hydrogen nuclei. ^{4}He act as a catalyst in PPII and PPIII since the interaction of an α-particle leads to the production of two.

Once the hydrogen is exhausted in the core of a star, it starts to contract slowly because the helium core has no source of energy. As a consequence an increase in the density and temperature of the star allows the He-rich region to fuse hydrogen in the overlying layers. The resulting thermal pressure wave will expand the outer region and cool the star at the phase of a red giant branch. The addition of helium from the shell to the core leads to helium flashes, in which the collapsed core becomes hot and dense enough to produce nuclear reactions among He-nuclei. During this quiescent He-burning stage, direct triple α-particle collisions form ^{12}C. If ^{12}C captures another α-particle, ^{16}O will be produced in one of the most important reactions for stellar evolution. After H and He, ^{12}C and ^{16}O have the highest concentrations in the universe. The C/O ratio equals 0.6 [9]. If the temperatures are sufficiently high, the

α-capture process can keep on producing heavier nuclei in the core of collapsing stars such as ^{20}Ne, ^{24}Mg and so on, but with a moderate rate to maintain the ^{12}C to ^{16}O ratio.

B. Thermonuclear Runaways in Oxygen Neon Novae

Half of the observed stars are members of binary systems, which may be composed of two massive main sequence stars such as a 10 $M_\odot$ primary and its 5 $M_\odot$ companion [10]. Since the lifetime of the star is shorter when its mass is higher, $\tau \propto M^{-3}$ [11], the primary star undergoes two evolution stages that are accompanied by losing mass either through stellar winds in all directions or through Roche lobe overflows (ROLF). The Roche lobe is the critical maximum radius that the expanded star can not exceed without losing mass to its companion. The two ROLFs, which occur due to hydrogen and helium burning, contaminate the primary's core with carbon and oxygen nuclei and reduce the mass of the primary to approximately 1 $M_\odot$. According to the virial theorem, when the thermal energy is decreased, the gravitational potential forces the star to successive contractions until the next thermonuclear runaways (TNR) begin. Thus, the density and the temperature in the core should increase sufficiently for carbon to interact with itself and produce neon and sodium ashes

$$^{12}\mathrm{C} + {}^{12}\mathrm{C} \rightarrow {}^{23}\mathrm{Na} + \mathrm{p} \tag{1.11}$$

$$^{12}\mathrm{C} + {}^{12}\mathrm{C} \rightarrow {}^{20}\mathrm{Ne} + \alpha. \tag{1.12}$$

The nucleosynthesis of nuclei is associated with the mass and evolutionary phases of the star. The gaseous matter is considered as an ideal gas, which is completely ionized by the induced pressure after contractions. Electrons are fermions that follow the Fermi-Dirac statistics, where the Pauli exclusion principle should be satisfied.

Under high pressure, the electrons are forced to fill all the quantum states up to the Fermi energy level. An electron degenerate gas is formed to resist the extra compressibility of the star and stabilize its last volume. A white dwarf (WD) exists under these circumstances, which is identified as the inert core of a dead star that has lost its peripheral layers. The mass of a WD is comparable to the solar mass and can not exceed the Chandrasekhar limit [9], where the maximum M_{WD} that could be supported by the electron degeneracy is less than 1.4 $M_\odot$. But because of its high density, it is approximately the size of the Earth ($R = 6378$ km). Depending on the chemical composition and mass, WDs are classified into two main categories. If the core is made of equivalent concentrations of carbon and oxygen uniformly distributed throughout the star and $M_{WD} \leq 1\ M_\odot$ [12], the final result is a Carbon-Oxygen (CO) white dwarf. For massive WD, $1\ M_\odot \leq M_{WD} \leq 1.4\ M_\odot$, and when the carbon in the core is completely converted to neon and oxygen, as mentioned above, an Oxygen-Neon (ONe) WD will be formed.

At the end of the mass transfer processes from the massive primary to its lighter companion, a close binary is left with a 1.1-1.4 $M_\odot$ ONe white dwarf and $\sim 6\ M_\odot$ large main sequence star [10]. When the secondary evolves to a red giant as part of its life cycle, its matter fills the Roche lobe and starts to transfer and accrete through the inner Lagrangian point onto the surface of the WD as shown in Fig. 3 [13]. The impact between the material of the outer layer of the WD and the hydrogen gas that spirals into it at high velocity mixes them and forms a thin shell on top of the WD. The strong gravitational field compacts the gas in the envelope, then compresses it to high density, of the order of $5 \times 10^3\ \mathrm{g\,cm^{-3}}$ [14], as more material falls in. In the meantime, the collisions convert the kinetic energy of the gas to radiation that heats up the envelope to 20 MK. Since ONe WD, where 85% of its mass is considered

as a degenerate ONe core surrounded by a light CO mantle [10], is unresponsive to heat, fusing the hydrogen homogenously in the accretion disk is indeed the main radiation source that sets the stage later for a classical nova outburst. The explosion is associated with the occurrence of a TNR, in which the fresh hydrogen starts new chains of reactions to synthesize heavier elements, where the nuclear reactions that take place are similar to those in the stellar interiors.

FIG. 3. Simulation of a binary system showing the flow of the material from the Red Giant through the Roche lobe and its accreting on the surface of the white dwarf [13].

Unlike normal stars, where the gas expansion is proportional to the increased temperature, the scenario in ONe novae is different. Earlier stages of TNR, $T_9 \sim 0.1$, proceed through nuclear reactions that may give crucial indications about the type of nuclei formed in the accreted disk [15]. During the peak stage of the TNR, $T_9 \sim 0.2 - 0.4$, the temperature is sufficiently high to dredge up neon seeds from the core of the WD by convection into the accumulated hydrogen layer. Heavy-element production and β^+-unstable nuclei may occur at this step via radiative proton-capture reactions.

Their subsequent decays inhabit the envelope with a gamma-ray flux. At the late

stages when the released gamma energy exceeds the Eddington luminosity limit [9], a sudden explosive outburst will eject the envelope into the stellar medium. This cataclysm occurs when radiation pressure is greater than the gravitational force, where the material density may reach $\rho > 10^4$ gm/cm^3 [16]. As a consequence, universal enrichments of the produced radioactive isotopes in TNR may provide significant information about the nucleosynthesis of light and intermediate nuclei in the galaxy.

The energy generation and the type of the ejected elements are very sensitive functions of the temperature of the envelope, the mass of the WD, and the primary composition of its core. Determination of the abundances of the chemical compositions, which represent the ejecta, depends on the detection of the ultraviolet, optical, and mainly infrared (IR) emission-line spectra. IR observations are important to distinguish between CO and ONe novae. Although both types have similar IR spectra directly after the outburst, an ONe nova is characterized by strong IR forbidden emission lines in the range of 2-40 μm [14], which indicate the abundances of heavy elements up to calcium. Recent studies are exploring the reaction chains that build up several nuclei in nova events, particularly the CNO and NeNa cycles.

C. CNO and HCNO Cycles

The two main sequences of reactions to fuse hydrogen are the pp-chains and the carbon-nitrogen-oxygen (CNO) cycle. The pp-chains are the dominating source of energy in old stars and the sun. In stars more massive than the sun the pp-chains may still occur, but the CNO cycle is more favorable to convert hydrogen to helium [17]. The cycle also controls the nuclear reactions at the beginning of TNR in a nova outburst, where C, N, and O act as catalysts and their concentrations are constant,

while H nuclei are consumed.

The CNO cycle shown in Fig. 4 starts with the ^{12}C(p,γ)^{13}N reaction that is followed, depending on the local temperature, by a sequence of β^+-decay, proton capture, or (p,α) steps. The created elements are among those that have the smallest Coulomb barriers and the highest abundances. Its main mechanism as originally discussed by Bethe [18] can be summarized in the following loop

$$^{12}\mathrm{C}(p,\gamma)^{13}\mathrm{N}(\beta^+\nu)^{13}\mathrm{C}(p,\gamma)^{14}\mathrm{N}(p,\gamma)^{15}\mathrm{O}(\beta^+\nu)^{15}\mathrm{N}(p,\alpha)^{12}\mathrm{C}. \tag{1.13}$$

The net result is the conversion of four protons into one ^{4}He nucleus, similar to Eq. (1.8). Oxygen plays an important role in developing the cycle. The possibility for ^{15}N to collide with a proton to regain ^{12}C is much greater than capturing a proton by ^{15}N to produce ^{16}O [19]. However, once ^{16}O is present, a slow leakage out of the above cycle generates a new path via

$$^{15}\mathrm{N}(p,\gamma)^{16}\mathrm{O}(p,\gamma)^{17}\mathrm{F}(\beta^+\nu)^{17}\mathrm{O}(p,\alpha)^{14}\mathrm{N}. \tag{1.14}$$

Thus, the combination of the two cycles is known as the CNO bi-cycle. Model calculation shows an overproduction of ^{13}C, ^{15}N, and ^{17}O products in the ejecta [21]. When the temperature increases to $T_9 \sim 0.2$ in novae, nuclear reactions become so fast that ^{13}N has enough time to collide with protons to form ^{14}O before it decays to ^{13}C, as shown in Fig. 4. When this occurs, the energy production is limited by the slower β^+-decay lifetimes of ^{14}O and ^{15}O rather than the proton-capture rate of ^{14}N. This β^+-limited branch is known as the hot CNO cycle (HCNO). The cycle enhances the abundance of ^{18}O since its production relies on the ^{18}O(p,γ)^{19}F/^{18}O(p,α)^{15}N reaction branching. The competition of these two reactions may either close the cycle or open it up to proceed through (p,γ) reactions to create ^{19}F and ^{20}Ne. Once the

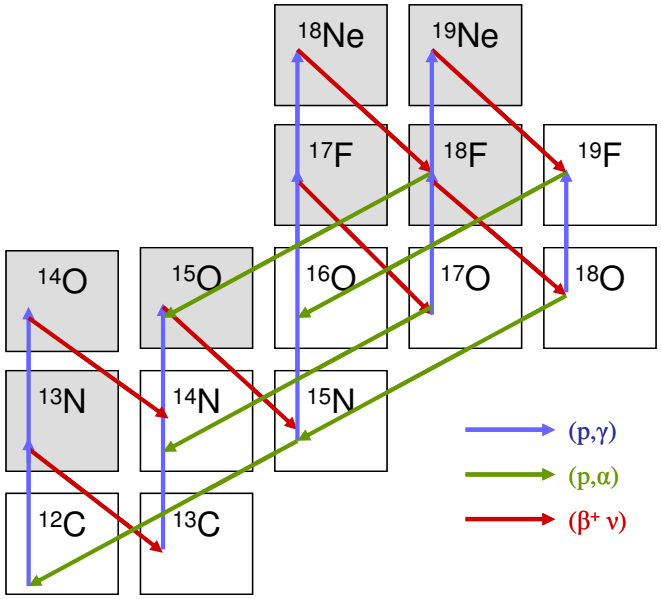

FIG. 4. Hydrogen burning in the HCNO cycles, which include proton capture reaction through the unstable nuclei ^{13}N, ^{17}F, and ^{18}F.

temperature is high enough to produce ^{20}Ne, $T_9 \sim 0.4$, a one way breakout can occur from the bottleneck of the HCNO loop to the onset of the rapid proton capture (rp) process [21].

D. The Ne-Na Cycle

In ONe novae, the possible pathway toward the more energetic rp-process takes place when the protons have sufficient thermodynamic energies to overcome the Coulomb barriers of the previously produced elements in the HCNO cycle in order to form heavier nuclei. Since the proton capture reaction must wait on the weak interaction of β^+-decay before the build up of heavier elements can continue, the nucleosynthesis of the process may not extend all the way to the proton drip line [9]. Thus, it is characterized by the competition between the β^+-decay and the proton-induced reactions. A new scenario to produce proton rich nuclei and fuse H into He occurs

through the NeNa cycle via the sequence

$$^{20}\mathrm{Ne}(p,\gamma)^{21}\mathrm{Na}(\beta^{+}\nu)^{21}\mathrm{Ne}(p,\gamma)^{22}\mathrm{Na}(\mathrm{p},\gamma)^{23}\mathrm{Mg}(\beta^{+}\nu)^{23}\mathrm{Na}(p,\alpha)^{20}\mathrm{Ne}. \tag{1.15}$$

Even though the NeNa cycle is not an important source for energy production in comparison with the pp-chains and CNO cycles, its importance lies in the fact that it synthesizes the elements between ^{20}Ne and ^{24}Mg with high abundances. The smaller Q-values for the proton capture allow measuring all the reactions in the cycle directly [22]. If the temperature stays high in the nova outburst, $T_9 \sim 0.2$-0.4 [23], the NeNa cycle opens up via the reactions ^{23}Na(p,γ) and ^{24}Mg(p,γ) to generate elements up to Si in what is known as the MgAl cycle.

E. The Missing Evidence of ^{22}Na

Massive ONe novae are common events in the Galaxy. The theoretical and astrophysical analysis of the spectroscopic lines reveals that their probability to occur accounts for approximately one-third of all the recently detected novae [14]. The neon concentration of these events in comparison with the solar system abundance is larger by a factor of ~ 300 [24]. Moreover, the enrichment of ^{22}Ne in the Ne-E meteorites, which contain grains that might be partially condensed in nova outbursts, provides other evidence of the preexistence of sodium isotopes, mainly ^{22}Na [25]. Taken all together, the above observations support the theory that the H-burning sequence of reactions by means of the NeNa cycle can yield substantial concentrations of ^{22}Na in ONe novae.

The radioactive ^{22}Na decays to ^{22}Ne via the reaction

$$^{22}\mathrm{Na} \rightarrow {}^{22}\mathrm{Ne} + \beta^{+} + \nu. \tag{1.16}$$

The mean lifetime of the reaction is $\tau = 3.75$ yr. The β^+-decay populates the short-lived first excited state in ^{22}Ne and leads to the emission of a 1.275 MeV γ-ray. The flux of these γ-rays is given by[9]

$$F_{\gamma,^{22}\mathrm{Na}} = 4 \times 10^{-5} \left(\frac{M_{eject}}{10^{-5} M_{\odot}}\right) \left(\frac{Z_{22}}{10^{-3}}\right) \left(\frac{D}{kpc}\right)^{-2} e^{-t/3.75yr} \left[\mathrm{cm}^{-2}\mathrm{s}^{-1}\right]. \qquad (1.17)$$

It is suggested that for a typical ONe nova, the ejected mass $\mathrm{M}_{eject} \approx 10^{-4} M_{\odot}$, and the fraction of ^{22}Na $\mathrm{Z}_{22} \approx 10^{-4}$, which translates to the possibility of observing almost 10^{-8} $\mathrm{M}_{\odot}$ ejected ^{22}Na per nova event [25]. If the nova is at a distance D $\sim$ 1 kpc, the detected γ-ray flux at the earth will be the order of 10^{-4} $\mathrm{cm}^2\,\mathrm{s}^{-1}$. These predicted concentrations are within the sensitivity limit of the space-based γ-ray telescopes, such as Compton Gamma Ray Observatory (CGRO) and INTEGRAL. However, observations of five ONe novae using CGRO have not found the signature of these γ-rays and have only been able to set an upper limit for its ejecta, which is below the theoretical estimations. For example, in Nova Her 1991 (V838 Her), which was expected to be one of the most favorable for observing, the detected flux limit was around a factor of three smaller than the level initially predicted by model calculations [25].

Although the real cause for this contradiction is not clear, the evolution of the nucleosynthesis in the rp-process may give an explanation for the missing flux of ^{22}Na γ-rays. Depending on the temperature achieved in the burning region, ^{22}Na is synthesized in novae following two possible ways, either in the cold NeNa cycle: ^{20}Ne$(p,\gamma)^{21}$Na$(\beta^+\nu)^{21}$Ne$(p,\gamma)^{22}$Na, or in the hot NeNa cycle through the chain ^{20}Ne$(p,\gamma)^{21}$Na$(p,\gamma)^{22}$Mg $(\beta^+\nu)^{22}$Na, as shown in Fig. 5. Studying the reaction rate for ^{21}Na$(p,\gamma)^{22}$Mg shows that the amount of the ^{22}Na abundance in ONe WD may be reduced in the hot cycle path [26], where the temperature and density are still high

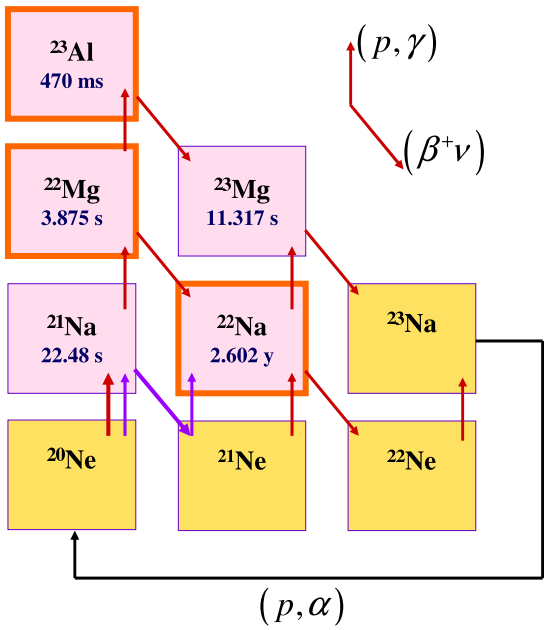

FIG. 5. The sequence of reactions in the NeNa cycles. The isotope ^{21}Na will either β decay into ^{21}Ne to produce the "cold" cycle, or capture a proton to form ^{22}Mg in the "hot" cycle.

enough to permit ^{21}Na burning to proceed more rapidly through the proton capture reaction. Once ^{22}Mg is produced, two reactions paths are available for it to reduce the residual ^{22}Na abundance. Either it β^{+}-decays to produce ^{22}Na, which may capture a proton via the radioactive reaction ^{22}Na$(p,\gamma)^{23}$Mg – this reaction is considered as the main depletion candidate [27] – or the ^{22}Mg is depleted to form ^{23}Al. In the explosive conditions, a fast and strong ^{22}Mg$(p,\gamma)^{23}$Al reaction may play the major role bypassing the production of ^{22}Na [52].

The nova explosion time scale for a TNR is $\sim$ 200 s [29]. Despite its low proton threshold Q-value, ^{22}Mg$(p,\gamma)^{23}$Al is so fast that the photodisintegration of ^{23}Al and its equilibrium may not be reached. Hence, sequential proton captures on ^{22}Mg and ^{23}Al may lessen the effective lifetimes of ^{22}Mg and its daughter ^{22}Na. The ^{22}Mg$(p,\gamma)^{23}$Al reaction is dominated by direct capture to the ground state ($d_{5/2}$) in ^{23}Al and resonant

capture through the ^{23}Al first excited state ($s_{1/2}$).

F. The Production of ^{18}F

The major sources of γ-ray lines are not only generated from the de-excitation of the daughter nuclei of β-unstable nuclei, as mentioned above, but also from positron-electron annihilation in the nova envelope. This annihilation leads to emission of a line at 511 keV and a continuum below it [20]. It is believed that ^{13}N ($\tau = 862$ sec) and ^{18}F ($\tau = 158$ min) are the main contributors to the production of observable positron annihilation radiation. Because of its short lifetime, ^{13}N will be consumed faster in the time scale of the expanding envelope, which may take a few hours. Therefore the decay of ^{18}F is more important for γ-ray astronomy since its γ-ray photons are emitted when the envelope starts to be transparent. The largest 511 keV fluxes are produced in the more massive ONe novae [30], and their yields depend on the nuclear reactions that create and destroy ^{18}F.

^{18}F is synthesized in the HCNO cycle via two main sequences

$$^{16}\mathrm{O}(p,\gamma)^{17}\mathrm{F}(p,\gamma)^{18}\mathrm{Ne}(\beta^{+}\nu)^{18}\mathrm{F} \tag{1.18}$$

$$^{16}\mathrm{O}(p,\gamma)^{17}\mathrm{F}(\beta^{+}\nu)^{17}\mathrm{O}(p,\gamma)^{18}\mathrm{F}. \tag{1.19}$$

The details are shown in Fig. 4. Its yield is mainly constrained by the destruction reaction ^{18}F(p,α)^{15}O. The reaction rate for ^{18}F(p,γ)^{19}Ne is 10^3 times smaller and hence makes a negligible contribution to ^{18}F destruction. According to the ONe models, when the temperature in the burning shell reaches $T_9 \sim 02$, ^{16,17}O concentrations are decreased by one to two orders of magnitude [31], and hence the main nuclear activity to produce ^{18}F is driven by the second chain through the dominant reaction

^{17}O(p,γ)^{18}F. However the uncertainty in this reaction rate, as well as the ^{18}F(p,α) rate, changes the ^{18}F abundances by factors of ≥ 500 [32]. ^{17}F also may affect the amount of ^{17}O, increasing its concentration in the envelope. At such a high temperature, a fast proton capture onto ^{17}F may increase the enrichment of ^{18}Ne by several orders of magnitude [31]. In this case, the synthesis of ^{18}F through the first path grows to be more important.

Experimental studies to extract information for ^{18}F are difficult not only because it has a relatively short lifetime, but also because it is a self-conjugate nucleus (N=Z). Efforts to determine the production and the destruction of this nucleus are in progress. If $T_9 \geq 0.3$ in the envelope, another chain may occur through: ^{14}O(α,p)^{17}F(p,γ)^{18}Ne($\beta^+\nu$)^{18}F(p,γ)^{19}Ne(p,γ)^{20}Na. As a result, ^{17}F(p,γ)^{18}Ne is an important nuclear reaction that is interesting to be studied to understand the absence of 511 keV lines after the explosion. The rate of this reaction may influence the abundances of ^{18}F, ^{18}Ne, ^{17}F, and ^{15}O, and explain the transition sequence from the HCNO cycle to the rp-process. This rate will be dominated by direct capture to the two lowest energy 2^+ states in ^{18}Ne [20].

G. Objectives

Although classical novae are frequent events in the Galaxy (~ 30 yr^{-1}), the mass of the ejected material is in order of 10^{-5}-10^{-4} M$_\odot$ per nova, which accounts for less than 10^{-3} of the Galactic mass [21]. However, novae are promising sites to produce a considerable amount of individual nuclei with high relative abundances. Among these nuclei are the long-lived γ-ray emitters, such as ^{18}F and ^{22}Na. Model calculations overestimate the observations of the γ-ray lines resulting from their β-decays [21].

The incentive of this research is to determine the rate of the precursor reactions that may contribute to the synthesis of ^{18}F and ^{22}Na isotopes. These reaction rates will be used to elucidate the possibilities of detection and to put constraints on TNR models.

H. Dissertation Outline

The dissertation consists of five chapters. Chapter I presents an introduction about the principles of nucleosynthesis in several evolutionary systems. This chapter includes the specific objectives of the research supported by the relevant literature reviews. Chapter II describes the general definitions of the TNR reaction formalism, and the extraction procedure of the asymptotic normalization coefficients (ANC) in peripheral transfer reactions. The importance of the ANC technique to determine proton capture reaction rates in nova outbursts will be also discussed. The experimental setup of the multipole-dipole-multipole (MDM) spectrometer along with the Oxford detector and data acquisition system will be introduced in Chapter III. It also includes the detector calibrations and explicit information concerning the experiments performed. Chapter IV presents a detailed discussion of the data analysis, and the last chapter provides the final results of the determined reaction rates for ^{22}Mg(p,γ)^{23}Al and ^{17}F(p,γ)^{18}Ne and their impact on ONe novae.

CHAPTER II

THEORY

Radiative capture reactions play an important role in nova explosions. They liberate energy through several nucleosynthesis processes that also change the chemical compositions of evolving stars. This chapter presents the theory of determining the radiative capture rates and describes the method of extracting the ANCs in peripheral transfer reactions, which are then used to evaluate the capture reaction cross sections and the reaction rates.

A. Kinematics of Nuclear Reactions

When a projectile a of mass m_a interacts nonrelativistically with a target X of mass m_X to produce a nucleus Y and a new particle b, the nuclear reaction is expressed as

$$a + X \rightarrow Y + b. \tag{2.1}$$

The output of the reaction is constrained by several physical conservation laws that simplify the description of the motion of the particles. The kinetic energy of the interacting particles in the laboratory system is

$$E = \frac{1}{2} m_a v_a^2 + \frac{1}{2} m_X v_X^2. \tag{2.2}$$

Using the definitions of the velocity of the CM and the relative velocities of a and X

$$\begin{aligned} \overrightarrow{V} &= \tfrac{m_a \overrightarrow{v_a} + m_X \overrightarrow{v_X}}{m_a + m_X} \\ \overrightarrow{v} &= \overrightarrow{v_a} - \overrightarrow{v_X}. \end{aligned} \tag{2.3}$$

The corresponding kinetic energy in the center of mass (C.M.) will be

$$E = \frac{1}{2}MV^2 + \frac{1}{2}\mu v^2, \tag{2.4}$$

where $M = m_a + m_X$ and $\mu = \frac{m_a m_X}{m_a + m_X}$ are the total and reduced masses, respectively. The Eq. (2.4) includes the kinetic energy of the C.M., which is a conserved quantity, plus the kinetic energy in the center-of-mass system, which is responsible for the interaction. If the target X is stationary before the collision, the kinetic energy in the C.M. is related to the laboratory system by

$$E = \frac{m_X}{M}E_{Lab}. \tag{2.5}$$

B. Reaction Rates

In stellar systems, particles exist in terms of gases. The projectile and the target a and X from the previous section have densities N_a and N_X particles per cubic centimeter, respectively. The rate of nuclear reactions r is defined as the number of reactions per unit volume per unit time. It depends on the flux $N_a v$ of the incident particles, the reaction cross section σ_v, and the number of target N_X, where v is the relative velocity. The reaction rate is then given by

$$r(v) = N_a N_X \sigma_v v. \tag{2.6}$$

where the cross section σ_v at a relative velocity v identifies the probability that the reaction will occur between the colliding particles. Because the velocity is not constant in stellar environments, its distribution can be described by the function $\Phi(v)$, which is defined such that $\int_0^\infty \Phi(v)\, dv = 1$. Hence the average reaction rate per

pair of particles $\langle \sigma_v v \rangle$ is given by

$$R = N_a N_X \int_0^\infty \Phi(v)\, v\sigma(v)\, dv. \tag{2.7}$$

For a nondegenerate gas and nonrelativistic motion of the particles, $\Phi(v)$ in a thermodynamic equilibrium state is given by the Maxwell-Boltzmann distribution

$$\Phi(v) = 4\pi v^2 \left(\frac{m}{2\pi kT}\right)^{3/2} \exp\left(-\frac{mv^2}{2kT}\right). \tag{2.8}$$

If a and X are both moving with v_a and v_X, respectively, Eq. (2.8) is generalized to be double folded with both distribution functions $\Phi(v_a)$ and $\phi(v_X)$. The reaction rate is then simplified in terms of the C.M., where v_a and v_X are defined in terms of the relative velocity and the CM velocity. Thus

$$\begin{aligned} &\Phi(v_a)\,\Phi(v_X) \overset{Jacobian}{\rightarrow} \Phi(v)\,\Phi(V) = \\ &(4\pi V^2)\left(\tfrac{m_a+m_X}{2\pi kT}\right)^{3/2} (4\pi v^2)\left(\tfrac{\mu}{2\pi kT}\right)^{3/2} \exp\left[-\tfrac{(m_a+m_X)V^2}{2kT} - \tfrac{\mu v^2}{2kT}\right]. \end{aligned} \tag{2.9}$$

Substituting in Eq. (2.4), the average reaction rate per particle pair $\frac{r}{N_a N_X}$ will be

$$\langle \sigma_v v \rangle = 4\pi \left(\frac{\mu}{2\pi kT}\right)^{3/2} \int_0^\infty v^3 \sigma(v) \exp\left(-\frac{\mu v^2}{2kT}\right) dv. \tag{2.10}$$

Since $E = \frac{1}{2}\mu v^2$, Eq. (2.10) can be written as

$$\langle \sigma_v v \rangle = \left(\frac{8}{\pi\mu}\right)^{1/2} \frac{1}{(kT)^{3/2}} \int_0^\infty \sigma(E)\, E \exp\left(-\frac{E}{kT}\right) dE. \tag{2.11}$$

1. Nonresonant Reactions

A direct nuclear reaction takes place when two nuclear systems make a glancing contact then immediately separate. As a consequence, the two systems may survive the collision without changing their internal states (elastic scattering), one or both

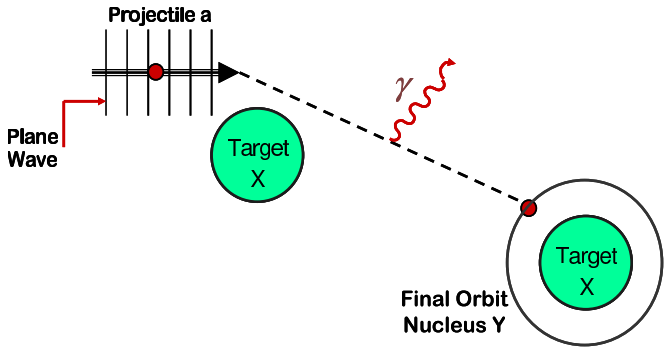

FIG. 6. An illustration of a direct capture reaction, where the transition goes directly to the final state in the nucleus with the emission of a γ-ray.

systems are left in an excited state (inelastic scattering), or nucleon(s) may transfer across from one nucleus to the other(transfer reaction). If the $a+X$ goes directly from the ground states in the entrance channel to the ground state or a specific excited state in the nucleus Y with the emission of γ-radiation, it will be named as a peripheral or direct capture reaction, as shown in Fig. 6. Because these reactions occur at all astrophysical projectile energies with a cross section varying smoothly with the energy, they are also called nonresonant reactions. Their importance is related to the tendency of populating the low-lying states of nuclei, and they are studied to give information about the overlap between the interacting nuclei.

For charged particles, the low-energy cross section $\sigma(E)$ that leads to a nuclear reaction depends strongly on the Coulomb barrier penetrability and the de Broglie wavelength. It is characterized by introducing the astrophysical S-factor, $S(E)$

$$\sigma\left(E\right)=\frac{1}{E}\exp\left(-2\pi\eta\right)S\left(E\right), \tag{2.12}$$

where η is the Sommerfeld parameter and is equal to

$$\eta=\frac{Z_aZ_Xe^2}{\hbar v}=\frac{31.29}{2\pi}Z_aZ_X\left(\frac{\mu}{E}\right)^{1/2}. \tag{2.13}$$

By substituting Eq. (2.12) in Eq. (2.11), the reaction rate becomes

$$\langle \sigma_v v \rangle = \left(\frac{8}{\pi\mu}\right)^{1/2} \frac{1}{(kT)^{3/2}} \int_0^\infty S(E) \exp\left(-\frac{E}{kT} - \frac{b}{E^{1/2}}\right) dE, \tag{2.14}$$

where

$$b = (2\mu)^{1/2} \pi e^2 \frac{Z_a Z_X}{\hbar} = 0.989 Z_a Z_X \mu^{1/2} \quad [\mathrm{MeV}]^{1/2}. \tag{2.15}$$

The behavior of the integral in Eq. (2.14) dominates the reaction rate. At low energies the $\exp(-bE^{-1/2})$ factor becomes very small, while at higher energies the factor $\exp(-\frac{E}{kT})$ goes rapidly to zero. The overlap between the tail of the Maxwell-Boltzmann distribution and the tail of the tunneling probability through the Coulomb barrier results in a distribution function centered around E_o, as shown in Fig. 7. Hence, nuclear reactions will take place in a narrow energy band that is known as Gamow peak, where

$$E_o = 1.22 \left(Z_a^2 Z_X^2 \mu T_6^2\right)^{1/3} \quad [\mathrm{keV}]. \tag{2.16}$$

Using Eq. (2.15), the maximum value of the integrand is

$$I_{\max} = \exp\left(-\frac{3E_0}{kT}\right). \tag{2.17}$$

The value of I_{max} decreases rapidly with increasing charge of the interacting nuclei, which implies that the nucleosynthesis during the TNR will produce nuclei with the smallest Coulomb barrier, while heavy nuclei do not contribute significantly to the energy production. For further simplification, the Gamow peak can be approximated with a Gaussian function:

$$\exp\left(-\frac{E}{kT} - \frac{b}{E^{1/2}}\right) = I_{\max} \exp\left[-\left(\frac{E - E_o}{\Delta/2}\right)^2\right], \tag{2.18}$$

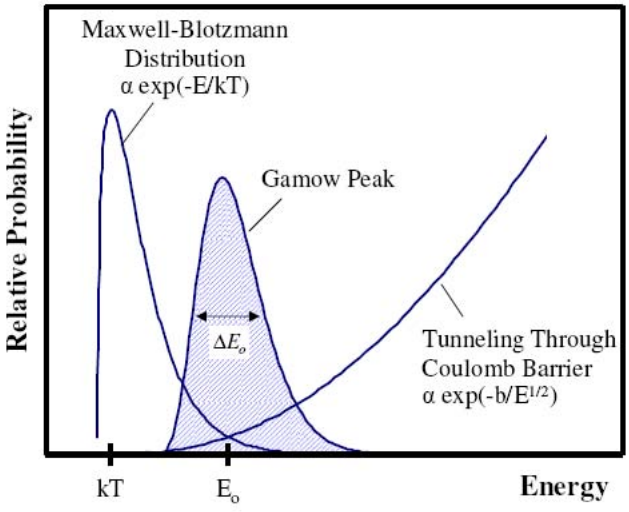

FIG. 7. The energy-dependent functions of the Maxwell-Boltzmann distribution and the tunneling through the Coulomb barrier are peaked at two opposite domains. The overlap between their tails leads to the Gamow peak centered around the stellar energy E_o, which is much larger than kT.

where the effective width of the function is

$$\Delta = \frac{4}{\sqrt{3}} \left(E_o kT\right)^{1/2} = 0.749 \left(Z_a^2 Z_X^2 \mu T_6^5\right)^{1/6} \quad [\text{keV}] \,. \tag{2.19}$$

When the S-factor is a smoothly varying function over stellar energies, its value can be expanded in a Taylor series around the effective burning energies [33]

$$S_{eff}\left(E_o\right) = S\left(0\right) \left[1 + \frac{5}{12\tau} + \frac{\dot{S}\left(0\right)}{S\left(0\right)} \left(E_o + \frac{35E_o}{12\tau}\right) + \frac{\ddot{S}\left(0\right)}{S\left(0\right)} \left(E_o^2 + \frac{89E_o^2}{12\tau}\right) + ...\right], \tag{2.20}$$

where

$$\tau = 42.46 \left(Z_a^2 Z_X^2 \frac{\mu}{T_6}\right)^{1/3} . \tag{2.21}$$

Substituting Eq. (2.18) and Eq. (2.20) in Eq. (2.14), the nonresonant reaction rate is then given by

$$N_A \langle \sigma_v v \rangle = N_A \left(\frac{2}{\mu}\right)^{1/2} \frac{\Delta}{(kT)^{3/2}} S_{eff}(E_o) \exp(-\tau) \quad \left[\frac{\text{cm}^3}{\text{mole s}}\right]. \tag{2.22}$$

2. Reaction Through Narrow Resonances

Unlike nonresonant reactions, reactions through narrow resonance states are two-step processes. The first one gives the probability that the C.M. energy of the entrance channel coincides with the energy E_r of a quasi-stationary quantum state of the compound nucleus, while the other process involves a subsequent γ-decay of E_r to a final state at lower energy as shown in Fig. 8. The nuclear reaction depends on the angular momentum ℓ of the incident particle that can initiate a specific resonance state. From the conservation of angular momentum, the condition $\overrightarrow{J_r} = \overrightarrow{J_a} + \overrightarrow{J_X} + \overrightarrow{\ell}$ should be satisfied, where J_r is the angular momentum of the resonant state. Also the parity should be conserved.

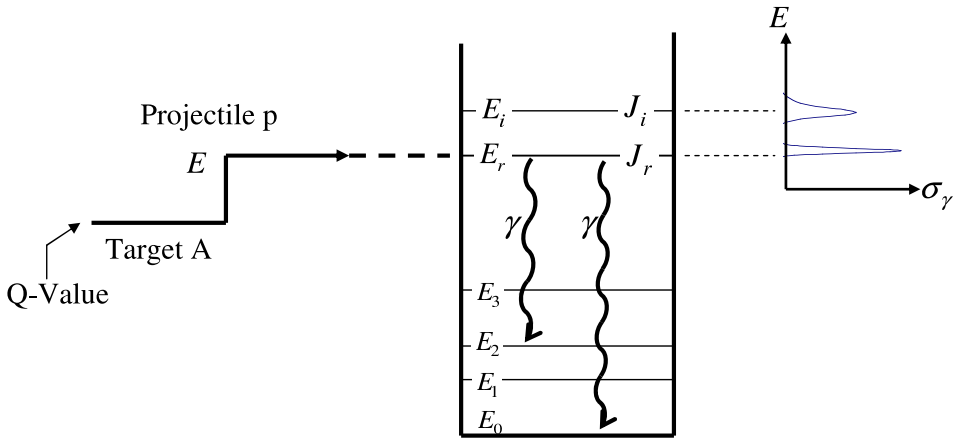

FIG. 8. After the projectile is captured by an excited state E_r, the state then decays to a lower level together with emission of γ-radiation. Resonant capture occurs when the energy $Q + E$ matches E_r.

The cross section is then given by the product of the maximum possible cross section and the transmission coefficient taking into account the resonance phenomena. Hence, its value is obtained by the Breit-Wigner formula [34]

$$\sigma(E) = \frac{\lambda^2}{4\pi} \frac{2J_r + 1}{(2J_a + 1)(2J_X + 1)} \frac{\Gamma_p \Gamma_\gamma}{(E - E_r)^2 + (\Gamma/2)^2}. \tag{2.23}$$

The first part of Eq. (2.23) represents a statistical factor that the combination of $\overrightarrow{J_a}$ and $\overrightarrow{J_X}$ results in $\overrightarrow{J_r}$, where $2J+1$ is the statistical weight of each J. The characteristics of the decay of the compound states are given by the resonant term, where Γ_p and Γ_γ are the partial widths that determine the rate at which the state captures a proton then γ-decays in the entrance and the exit channels, respectively. Γ represents the sum of all the partial widths of all allowed decay channels; $\Gamma = \Gamma_p + \Gamma_\gamma$.

For a (p, γ) reaction, the gamma width is typically no larger than a few electron volts. On the other hand, at stellar energies, the small probability for protons to penetrate the Coulomb barrier reduces Γ_p to a value that is comparable with Γ_γ. Hence the total resonance width is a very narrow spike with width $\Gamma \ll E_r$ in the Maxwell-Boltzmann distribution. Hence the $Ee^{-\frac{E}{kT}}$ term in Eq. (2.11) changes only slightly over the resonance region. Inserting Eq. (2.23) into Eq. (2.11) at $E = E_r$, the reaction rate through a narrow resonance is

$$\langle \sigma_v v \rangle = \left(\frac{2\pi}{\mu kT} \right)^{3/2} \hbar^2 \omega\gamma \exp\left(-\frac{E_r}{kT} \right), \tag{2.24}$$

where $\omega = \frac{2J_r+1}{(2J_a+1)(2J_X+1)}$ and $\gamma = \frac{\Gamma_p \Gamma_\gamma}{\Gamma}$. The product $\omega\gamma$ is called as the resonant strength. The total width Γ depends strongly on the Coulomb potential. If the reaction is near the Coulomb barrier, γ will approximately equal to Γ_γ and hence the strength of the resonance $\omega\gamma \approx \omega\Gamma_\gamma$.

C. Direct Measurements vs Indirect Measurements

Extreme densities and temperatures trigger reactions that may involve nuclei far from β-stability. Several different kinds of laboratory experiments are carried out to explore the nucleosynthesis of chemical elements in evolutionary stellar systems. These experiments are dedicated to measure nuclear reactions, decay mechanisms for β unstable nuclei, and the probability of nuclear reactions to occur (in terms of the cross section σ). A favorable way to determine the cross section is to carry out direct measurements using radioactive beams for short-lived isotopes and radioactive targets for long-lived isotopes. However, the favored energy region where astrophysical reactions take place is between tens and hundreds of keV. Thus, the σ values for these reactions at stellar energies below the Coulomb barrier are extremely small, of the order of nano and picobarns, and they decrease exponentially with decreasing energy. In addition, direct reactions in such an environment may involve contributions from excited states as well as the ground states, which are difficult to measure in the laboratory if the nuclear structure information is missing, or the energy resolution of the beam is too poor to distinguish between well-separated states. Moreover, the short half lives of the radioactive beams and (or) targets complicate the experiments.

Alternatively, indirect experimental methods can provide other approaches to examine the astrophysical reaction rates using stable beams and (or) targets. The main indirect methods are Coulomb dissociation [35] , Trojan Horse [36], and measurement of asymptotic normalization coefficients [37]. These methods give precise information that facilitates accurate predictions of the rates.

D. Nuclear Reactions and DWBA Model

Given the possibilities of studying the astrophysical reaction rates with several indirect techniques, it is crucial to have a reliable method for obtaining useful information from experimental measurements. Direct nuclear reactions are fast interactions with few degrees of freedom involved, which have been described successfully in quantum mechanics by applying the distorted wave Born approximation (DWBA). DWBA gives quantitative as well as qualitative information about the dynamics of the reaction and nuclear structure. The main physics behind this model premises that elastic scattering between two colliding nuclei is the most important event to occur, while other reaction channels can be treated as perturbations. For the reaction $a + X \rightarrow Y + b$, the total wave function Ψ that obeys the Shrödinger equation is

$$H\Psi = E\Psi, \tag{2.25}$$

where Ψ carries information on all open reaction channels, and may be expanded in terms of a complete set of internal states ψ_α

$$\Psi = \sum_\alpha \xi_\alpha(\vec{r})\psi_\alpha\left(\vec{x}_\alpha\right). \tag{2.26}$$

The Hamiltonian H can be written in the form of any partition channel, such as $H = H_\alpha + T_\alpha + V_\alpha = H_\beta + T_\beta + V_\beta = ...$, where the total hamiltonian for the system is then the sum of the internal Hamiltonians for the particles a and X, the kinetic energy of their relative motion, and their mutual interaction. An accurate solution of Ψ is not known yet, so ξ_α, which represents the projection of Ψ onto the partition α, is needed to describe the relative motion of $a + X$ when both nuclei are in their ground states. ψ_α is then the product of their plane waves $\psi_a\psi_X$. The complete set

of the outgoing β channels that result from the initial state α is given by

$$\Psi_{\alpha}^{(+)} = \sum_{\beta} \xi_{\beta}\left(\vec{r}\right)\psi_{\beta}\left(\vec{x}_{\beta}\right). \tag{2.27}$$

Solving the Shrödinger equation for the specific partition β is written as

$$\left(E_{\beta} - T_{\beta}\right)\xi_{\beta}\left(\vec{r}_{\beta}\right) = \left\langle \psi_{\beta}\left|V_{\beta}\right|\Psi_{\alpha}^{(+)}\right\rangle. \tag{2.28}$$

Then substituting Eq.(2.27) into Eq.(2.28) gives

$$\left(E_{\beta} - T_{\beta} - U_{\beta}\right)\xi_{\beta}\left(\vec{r}_{\beta}\right) = \left\langle \psi_{\beta}\left|W_{\beta}\right|\Psi_{\alpha}^{(+)}\right\rangle, \tag{2.29}$$

where $U_{\beta} = \left\langle \psi_{\beta}\left|V_{\beta}\right|\psi_{\beta}\right\rangle$, and W_{β} represents the residual interaction that is treated as a perturbation, $W_{\beta} = V_{\beta} - U_{\beta}$. By assuming that U_{β} is the average interaction potential V_{β} over the nuclei in the exit channel, the inhomogeneous part of Eq.(2.29) can be eliminated because of the small contribution of any excitation or rearrangement after the collision. Hence, only the diagonal matrix elements are involved in the prediction of U_{β}. Because the interaction is strong, when the incident particles enter the domain of the nuclear force, their plane wave function will be distorted by the nuclear potential, and their outgoing wave function will also be distorted by the effective nuclear potential due to the collision. Thus, as a first order approximation, $\xi_{\beta}^{(+)}$ is asymptotically equivalent to the distorted wave $\chi_{\beta}^{(+)}$ due to U_{β}, and Eq.(2.29) becomes

$$\left(E_{\beta} - T_{\beta} - U_{\beta}\right)\chi_{\beta}^{(+)}\left(\vec{k}_{\beta}, \vec{r}_{\beta}\right) = 0, \tag{2.30}$$

and its general solution is

$$\chi_{\beta}^{(+)}\left(\vec{k}_{\beta}, \vec{r}_{\beta}\right) \rightarrow e^{i\vec{k}_{\beta}\cdot\vec{r}_{\beta}} + f_{\beta}\left(\theta\right)\frac{e^{ik_{\beta}r_{\beta}}}{r_{\beta}}, \tag{2.31}$$

where $f_{\beta}\left(\theta\right)$ refers to the scattering amplitude. So $\chi^{(+)}$ in the DWBA consists of

an incident plane wave and outgoing spherical wave. Eq.(2.30) is usually called the optical-model Shrödinger equation [38], and its solution depends on the optical potential U_β, which indeed depends on the energy of the projectile. If this energy is low, only elastic scattering will take place and U_β is real. At higher energies, inelastic scattering and nuclear reactions are possible events, which means that part of the elastic scattering flux is absorbed. Thus, U_β has to be complex and negative to describe all the reaction channels accurately.

Since the incoming wave function is also distorted, $\chi^{(-)}$, with a condition that when $U_\beta \rightarrow 0$, $\chi_\beta^{(\pm)}$ are represented by a plane wave $e^{i\vec{k}\cdot\vec{r}}$. Getting the solution of the distorted waves from Eq.(2.30) and its complex conjugate provides the information needed to evaluate the transition amplitude from $\alpha \rightarrow \beta$

$$I_{\beta\alpha} \simeq \left\langle e^{i\vec{k}_\beta\cdot\vec{r}_\beta} \left|U_\beta\right| \chi_\alpha^{(+)} \right\rangle \delta_{\alpha\beta} + \left\langle \chi_\beta^{(-)}\psi_\beta \left|W_\beta\right| \psi_\alpha\chi_\alpha^{(+)} \right\rangle . \tag{2.32}$$

The first term refers to elastic scattering, and the second term is the DWBA amplitude of the nuclear reaction $I_{\beta\alpha}^{DWBA}$.

E. The Optical Potential and Elastic Scattering

The phenomenological optical model gives a simple method to characterize the interaction of two nuclei through a potential $U(r)$, where r refers to the distance between their CM. As mentioned in the previous section, the success of this model relies on its ability to reproduce the elastic scattering data. Solving the Shrödinger equation, Eq.(2.30) allows the construction of the asymptotic behavior of the wave function at distances larger than the interaction radius. Then the parameters of the potential are adjusted to give the best description of the elastic scattering. The most common

form of the potential is

$$U(r) = V(r) + i[W(r) + U_S(r)] + U_{SO}(r) + U_C(r), \tag{2.33}$$

where V refers to the real part of the potential, which is important for elastic scattering, while the absorptive potentials are represented by the volume W and the surface U_S forms. Including both imaginary forms in $U(r)$ at the same time increases the number of the parameters that need to be adjusted. Moreover, considering that the projectile propagates through uniform nuclear matter means that the volume potential should be involved for all cases, the surface form is often neglected in the analysis of elastic scattering data. Also, the spin-orbit interaction form, U_{SO}, is often not considered since it is only significant on the surface of the nucleus, in which case the effect of the polarization depends on which side of the nucleus the projectile is approaching. The last term of Eq.(2.33) stands for the Coulomb potential and is usually included whenever the interaction involves charged particles. Hence, only the optical model parameters (OMP) of the real and absorptive potential need to be varied systematically to optimize the prediction of the experimental differential cross section.

To obtain the OMP, the form of the chosen potential $U(r)$ must be short range that falls rapidly to zero near the surface of the nucleus, while the weak electromagnetic forces act at very large distances outside the nucleus. The nuclear size, the depth, and the surface thickness are the main characteristics of the potential. Two different shapes are frequently used to fit elastic scattering data: the Woods-Saxon potential and the double folding potential.

F. The Woods-Saxon Potential

The Woods-Saxon form was introduced [39] to overcome the difficulties of applying a square well potential with sharp edges, while the distributions of the nuclear charge and matter fall smoothly to zero beyond the nuclear radius. The Woods-Saxon potential is rather rounded, and represented by

$$U(r) = -\left(V f_V(r) + iW f_W(r)\right), \tag{2.34}$$

where V and W are related to the real and the imaginary well-depth of the potential. The function $f_x(r)$ is the form factor

$$f_x(r) = \frac{1}{1 + e^{\frac{r-R}{a}}}, \tag{2.35}$$

where a determines the surface diffuseness, and R is the nuclear radius.

At high bombarding energies, all the nuclear interior can participate in absorbing part of the incoming wave function, so both parts of Eq. (2.34) have the same shape as shown in Fig. 9. While at low projectile energies, the tightly bound nucleons in the interior are blocked from responding to the interaction by the Pauli exclusion principle an the fact that the neighboring orbitals are already filled. Therefore, the absorbing process will occur through the valence nucleons near the surface. In this case the imaginary potential is described by the surface potential term of Eq. (2.33) instead of the volume one, where $U_S \propto \frac{d}{dr} f_V(r)$.

In order to fit the elastic scattering data, all six parameters that characterize Eq. (2.34) should be varied to optimize the potential. The OMP have individual effects on the calculated differential cross section [40]. Increasing V or R shifts the angular

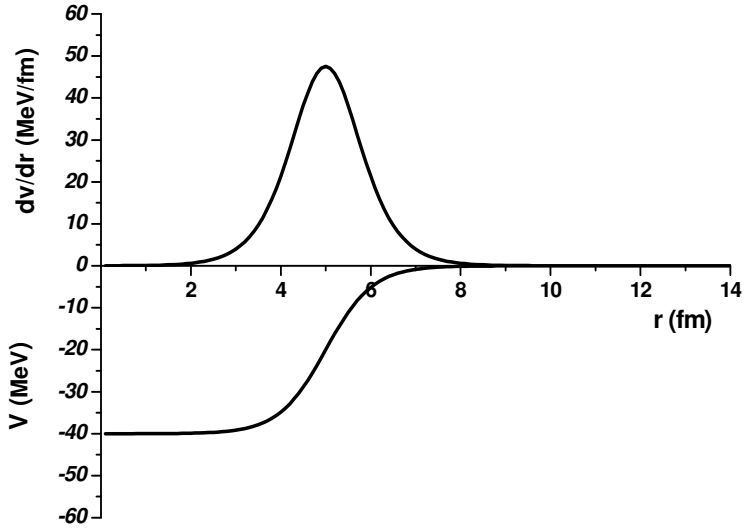

FIG. 9. Volume and surface potential derived from Woods-Saxon forms. The shape of $W(r)$ is similar to $V(r)$ at high energy and peaks near the surface at low energies.

distribution toward smaller angles, while increasing the diffusivity a reduces the cross section, especially at larger scattering angles. Increasing W smooths out the angular distribution by decreasing the height of the maxima and the depths of the minima in its oscillations.

G. The Double Folding Potential

Another method to analyze scattering data is to use double folding potentials for OMP. In this model, the potential is obtained by considering the effective nucleon-nucleon (NN) interaction between the matter distributions of the colliding particles, where the two body operator is

$$V = \sum_{i,j} v_{ij}, \tag{2.36}$$

i and j are related to each nucleon in the projectile and the target, respectively. The potential is then determined by the folding expression

$$U_F(R) = \int d\vec{r}_1 \int d\vec{r}_2 \rho_1(\vec{r}_1)\,\rho_2(\vec{r}_2)\,v_{eff}\left(\vec{s} = \vec{R} + \vec{r}_1 - \vec{r}_2\right). \tag{2.37}$$

$\rho(r)$ is the density distribution of one of the colliding nuclei in the ground state, which may be calculated in a standard Hartree-Fock procedure [41]. The integrations are over the coordinates shown in Fig. 10. In the absence of the spin-orbit interaction, both densities and $U_F(R)$ are considered spherical, and the potential is only a function of the interaction radius R. The double integrations in Eq. (2.37) are over the nucleons in the projectile as well as in the target. The density distributions ρ are normalized to give the number of nucleons in each nucleus. $\vec{s} = \vec{R} + \vec{r}_1 - \vec{r}_2$ is the NN separation distance.

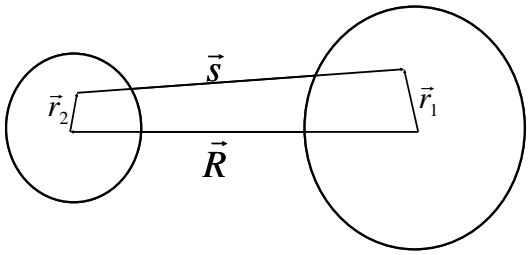

FIG. 10. The coordinates for the double folding integral, Eq. (2.37)

When the collision takes place over composite nuclei, the folding procedure may be simplified by using a local density approximation in folding the interaction [42], which assumes that the interacting nucleons are immersed in uniform nuclear matter with

a density

$$\rho\left(\vec{r}\right)=\left[\rho_1\left(\vec{r}_1+\frac{\vec{s}}{2}\right)\rho_2\left(\vec{r}_2-\frac{\vec{s}}{2}\right)\right]^{1/2}, \tag{2.38}$$

where $\rho\left(\vec{r}\right)$ averages the individual single particle densities that are evaluated at half distance between the two interacting nucleons. It was found that realistic potentials are obtained from the JLM effective interaction [43].

The JLM interaction is intended to produce a complex optical potential from the double folding model. In contrast, with many other effective interactions the double folding procedure is used to describe only the real part of the potential, while the imaginary OMP are treated phenomenologically with a Woods-Saxon form. The effective potential depends on the local densities as well as the energy of the incident particle. The original JLM interaction was extracted for nucleons in infinite nuclear matter of constant density. Then it was transposed by Bauge to nucleon-nucleon collisions [44]. We used their effective interactions

$$v_{eff}\left(\rho,E\right)=\frac{V\left(\rho,E\right)+iW\left(\rho,E\right)}{\rho}, \tag{2.39}$$

where V and W are for the NN interaction. The general form for the complex heavy ion potential in JLM is improved by inserting a smearing function $g\left(s\right)$ in Eq. (2.37) [45], where g has the exponential form

$$g\left(s\right)=\frac{1}{t^3\pi^{3/2}}e^{\left(-\frac{s^2}{t^2}\right)} \tag{2.40}$$

that tends to $\delta\left(s\right)$ as the range parameter $t\rightarrow 0$. The real and imaginary volume integrals are not affected by $g\left(s\right)$ since the finite range form factors are normalized to one. Global analysis of elastic scattering data shows that the imaginary radius is larger than the real radius. The optimum values for the range parameters are $t_V=$

1.2 fm and $t_W = 1.75$ fm [46], but they can be taken as free parameters as well [45].

For a loosely bound p-shell nucleus, elastic scattering is strongly coupled with neutron transfer and break up reactions, so the description of the data requires a significant normalization of the folding potentials

$$U(r) = N_V V_{fold}(r) + iN_W W_{fold}(r). \tag{2.41}$$

The elastic scattering data is then fit by adjusting simultaneously four parameters: the normalization parameters N_V and N_W, and the range parameters t_V and t_W.

H. Asymptotic Normalization Coefficients (ANC)

The nuclear structure of the $a(b+c) + X \rightarrow b + Y(X+c)$ reaction, where c is the transferred nucleon, is contained in the matrix elements of the overlap function $I^{DWBA}_{\beta\alpha}$, Eq. (2.32), i. e. it is contained in the overlap between the bound state wave functions $\langle \psi_a | \psi_b \psi_c \rangle$ and $\langle \psi_Y | \psi_X \psi_c \rangle$ in the transfer reaction, where ψ_Y is the bound state of particles X and c. These overlaps are determined by a factor named the spectroscopic factor S that defines the probability for the nucleus a with ψ_a to be composed of the nucleon c moving with specific quantum numbers ℓ, j relative to the nucleus b with ψ_b. S gives information about the relation between the initial and final states in the transfer reaction.

To extract information about the nuclei involved in the reaction, normalized single-particle wave functions are generated for a nucleon binding potential around the core assuming that they provide a good approximation of the overlap functions. However, the absolute normalization of S is still uncertain due to the lack of spectroscopic factor measurements and because the values derived from many nuclear reactions are

strongly dependent on the geometric parameters of the nucleon binding potentials, mainly the radius r_o and the diffuseness a that are used to determine the single-particle orbital.

Radiative proton capture reactions in astrophysical environment occur at distances much larger than the radius of the capturing nucleus and at low binding energies of the captured particles. For a direct radiative capture, the process takes place through the tail of the nuclear overlap function. The shape of this tail is completely determined by the Coulomb potential between the interacting nuclei, so the reaction is peripheral. Its rate can be estimated with good precision by a single parameter, explicitly, the ANC that gives the amplitude of this tail [47] [48] .

For the decomposition $Y \rightarrow X + c$, the overlap function I of the bound state wave functions for individual particles is given by

$$I^{Y}_{Xc}\left(\vec{r}\right) = \sqrt{Y}\left\langle \psi_X\left(\zeta_X\right)\psi_c\left(\zeta_C\right)\left|\psi_Y\left(\zeta_X,\zeta_C,\vec{r}_{Xc}\right)\right.\right\rangle . \tag{2.42}$$

The wave function of the final nucleus ψ_Y is written as a function of the position of the nucleon c relative to the C.M. of the remaining nucleons in the core X, $\vec{r}_{Xc}$, and ζ that stands for the other intrinsic coordinates including spin and isospin variables. The antisymmetrization factor $\sqrt{Y}$ relates to the Y identical nucleons, where each one of them can be labeled as c. Satisfying the condition of conserving angular momentum, the above equation may be written in terms of Clebsch-Gordan coefficients as

$$\begin{aligned} I^{Y}_{Xc}\left(\vec{r}\right) &= \sum_{l_Y m_{l_Y} j_Y m_{j_Y}} \left\langle J_X M_X j_Y m_{j_Y}\left|J_Y M_Y\right.\right\rangle \\ &\times \left\langle J_c M_c l_Y m_{l_Y} | j_Y m_{j_Y}\right\rangle i^{l_Y} Y_{l_Y,m_{l_Y}}\left(\hat{r}\right) I^{Y}_{Xcl_Y j_Y}\left(r_{Xc}\right), \end{aligned} \tag{2.43}$$

where $j_Y m_{j_Y}$ are the total angular momentum of c and its projection in Y, ℓ_Y and m_{ℓ_Y} are the orbital angular momentum of the relative motion of X and c in the bound state Y and its projection, and the summation is over all the values of these quantum numbers that are allowed by angular momentum and parity conservation in the process $Y \rightarrow X + c$. $Y_{\ell_Y, m_{\ell_Y}}(\hat{r})$ are the spherical harmonic functions. The last component of Eq. (2.43) $I^Y_{Xcl_Y j_Y}(r_{Xc})$ is the radial overlap function, which is significant to describe the one nucleon transfer reaction.

The square of the norm of the overlap function defines of the spectroscopic factor, S

$$S_{Xc} = \int \left| I^Y_{Xc}(r_{Xc}) \right|^2 d\vec{r}. \tag{2.44}$$

The approximation of the overlap function to a single-particle wave function is usually given by

$$I^Y_{Xcl_Y j}(r_{Xc}) = S^{1/2}_{Xcl_Y j_Y} \psi_{n_Y l_Y j_Y}(r_{Xc}), \tag{2.45}$$

where $\psi_{n_Y l_Y j_Y}$ is the normalized bound state wave function of the relative motion of X and c, and $S_{Xcl_Y j_Y}$ is the corresponding spectroscopic factor with the appropriate quantum numbers n_Y, l_Y, and j_Y. To find the overlap function, one has to solve Eq. (2.43) for an infinite number of coupled integro-differential equations. Since the spectroscopic factor is a model-dependent number, its value can differ from unity due to the coupling between any open channel with the two-body channel $(Xc)_{l_Y j_Y}$. A single-particle approach is used such that the radial overlap function, Eq. (2.45), can be approximated by the single-particle overlap function

$$I^Y_{Xcl_Y j} \approx I^{(sp)}_{Xcl_Y j} = \left[S^{(sp)}_{l_Y j_Y} \right]^{1/2} \psi_{n_Y l_Y j_Y}(r), \tag{2.46}$$

where ψ represents the single-particle bound state wave function (Xc) that is used

in DWBA to analyze the experimental data. If Eq. (2.45) and Eq. (2.46) are identical in the nuclear interior and exterior, then $S^{(sp)}_{l_Y j_Y}$ and $S_{Xcl_Y j_Y}$ are identical. However, for $r < R$, where both I and ψ have most of their probability, the overlap function is a many-particle object and its radial dependence may differ from the radial dependence of the single-particle wave function. On the other hand, for $r > R$, their radial dependencies are the same, and they only differ by their overall normalization, which is given by the ANC. The asymptotic behavior of the of radial overlap function is

$$I^Y_{Xcl_Y j_Y}(r_{Xc}) \to C^Y_{Xcl_Y j_Y} \frac{W_{-\eta, l_Y+1/2}(2\kappa_{Xc} r_{Xc})}{r_{Xc}}, \tag{2.47}$$

where $W_{-\eta, l_Y+1/2}(2\kappa_{Xc} r_{Xc})$ is the Whittaker function describing the asymptotic behavior of two charged particles interacting by the Coulomb force. $\kappa_{Xc} = \sqrt{2\mu_{Xc}\varepsilon_{Xc}}$ is the wave number of the bound state, and μ_{Xc} is the reduced mass. $C^Y_{Xcl_Y j}$ is the asymptotic normalization coefficient. The asymptotic behavior of the normalized single-particle bound state wave function is

$$\psi_{Xcl_Y j_Y}(r_{Xc}) \to b_{Xcl_Y j_Y} \frac{W_{-\eta, l_Y+1/2}(2\kappa_{Xc} r_{Xc})}{r_{Xc}}, \tag{2.48}$$

where b is the single-particle ANC. By the proper choice of $S^{(sp)}_{l_Y j_Y}$, one can make Eq. (2.46) exact for $r > R$. Using Eq. (2.45), the comparison between the last two equations gives the relation that connects the single-particle spectroscopic factor to the ANC

$$S^{(sp)}_{l_Y j_Y} = \frac{\left(C^Y_{Xcl_Y j_Y}\right)^2}{\left(b_{l_Y j_Y}\right)^2}. \tag{2.49}$$

The experimental cross section in conventional DWBA is parameterized by the prod-

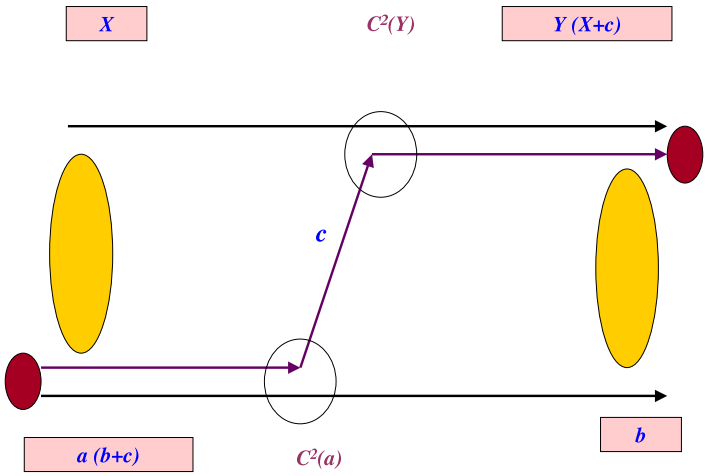

FIG. 11. The pole diagram describing the transfer reaction of the nucleon c and the importance of the ANCs for both vertices of the reaction.

uct of the spectroscopic factors of the initial and final channels in the form [49]

$$\frac{d\sigma}{d\Omega} = \sum_{j_Y j_a} S_{bcl_a j_a} S_{Xcl_Y j_Y} \sigma^{DW}_{l_a j_a l_Y j_Y}, \tag{2.50}$$

which can be written in terms of the ANCs by using Eq. (2.49)

$$\frac{d\sigma}{d\Omega} = \sum_{j_Y j_a} \left(C^a_{bcl_a j_a}\right)^2 \left(C^Y_{Xcl_Y j_Y}\right)^2 \frac{\sigma^{DW}_{l_a j_a l_Y j_Y}}{b^2_{bcl_a j_a} b^2_{Xcl_Y j_Y}}. \tag{2.51}$$

The ANC is a property of the transfer reaction and its value can be extracted experimentally, while b is calculated theoretically. The strong dependence of the DWBA cross section and b on the geometric parameters of the Woods-Saxon potential, mainly r_o and a, cancel each other, so that the ANC is nearly a model-independent characteristic of the nuclear states. Eq. (2.51) implies that the value of $C^Y_{Xcl_Y j_Y}$ can be extracted if the ANC $C^a_{bcl_a j_a}$ of the complementary vertex is known, as shown in Fig. 11.

The main purpose is to find a relation between the ANC and the peripheral radiative capture reaction at low energy that leads to a loosely bound final nucleus: $A + p \rightarrow B + \gamma$. The amplitude of the matrix element of the radiative capture reaction is given by

$$M^{DC} \propto \left\langle \psi_B \left(\zeta_A, \zeta_p; \vec{r}\right) \left| \hat{O} \right| \psi_A \left(\zeta_A\right) \psi_p \left(\zeta_p\right) \psi_i^+ \left(\vec{r}\right) \right\rangle . \tag{2.52}$$

$\hat{O}$ is the electromagnetic transition operator, and $\psi_i^+ \left(\vec{r}\right)$ is the scattering wave function in the initial state. The greatest interest in nuclear astrophysics is when the scattering energy goes to zero. The initial scattering wave function is a Coulomb wave. So any ambiguities associated with the proton-nucleus interaction are eliminated. After integration and summation over the internal degrees of freedom, the formula for the direct capture cross section is [48]

$$\sigma^{DC} = \sum_{j_B} \left(C^B_{Apl_Bj_B}\right)^2 \frac{\tilde{\sigma}^B_{l_Bj_B}}{b^2_{Apl_Bj_B}}. \tag{2.53}$$

Thus, the only unknown quantities in the last relation are the ANCs. Once they are obtained in a peripheral nuclear reaction, they can be used to calculate the direct capture amplitude and the astrophysical S-factor. The good agreement between the directly measured astrophysical S-factors compared to those determined using the ANCs in ^{16}O(^{3}He, d)^{17}F points out that the method is applicable to determine direct capture reactions to better than 9% [50].

I. The ANCs for ^{22}Mg$(p,\gamma)^{23}$Al from ^{13}C(^{22}Ne,^{23}Ne)^{13}C

^{22}Mg plays an important role in the production of ^{22}Na in the hot NeNa cycle. Its destruction by the radiative proton capture reaction ^{22}Mg$(p,\gamma)^{23}$Al must be investigated. The Gamow windows of the reaction for several temperatures in ONe novae are shown in Fig. 12. Wiescher *et al.* [51] calculated the reaction rate due to the

contribution of the direct capture from ^{22}Mg to the ground state of ^{23}Al. Later, the excitation energy of the first excited state in ^{23}Al was measured [52] and its strength was estimated from a shell model calculation and the nuclear structure of the mirror nucleus ^{23}Ne. The ground state in ^{23}Al is $5/2^+$ and the orbital angular momentum for a proton to occupy this state is $\ell = 2$. The first excited state in ^{23}Ne has $J^\pi = 1/2^+$. Its analog state in ^{23}Al is predicted as the only resonance important in ^{22}Mg$(p,\gamma)^{23}$Al [51]. Its excitation energy is $E_x = 0.528\,(20)$ MeV [53].

Recently, an experimental study of the β decay of a pure sample of ^{23}Al to determine the absolute branching ratios and *ft* values to states in ^{23}Mg confirms unambiguously that the ground state in ^{23}Al is $5/2^+$ [55]. This result coincides with the measurement of the magnetic moment of ^{23}Al, which agrees with shell model calculations for $J^\pi = 5/2^+$ [56]. Hence, the ground state spin and parity of ^{23}Al are settled. For the resonant state in ^{23}Al, the γ-ray width, $\Gamma_\gamma = 7.2 \pm 1.4 \times 10^{-7}$ eV [57], was obtained experimentally using Coulomb dissociation of ^{23}Al. This value is compatible with $\Gamma_\gamma = 5.49 \times 10^{-7}$ eV predicted in Ref. [53] and $\Gamma_\gamma = 6 \times 10^{-7}$ eV estimated in Ref. [58].

Direct measurements of the ^{22}Mg$(p,\gamma)^{23}$Al reaction at stellar energies have not been reported yet due to several difficulties. It is impossible to make ^{22}Mg $\left(t_{1/2} = 3.86\text{s}\right)$ as a target and difficult to obtain an intense ^{22}Mg beam for direct measurements in inverse kinematics. In order to avoid these difficulties, the ANC method is proposed to determine ^{22}Mg$(p,\gamma)^{23}$Al reaction rate.

^{23}Al is a weakly-bound proton-rich nucleus close to the drip line. Since the spin and parity of its ground state and resonance are equivalent with its mirror ^{23}Ne,

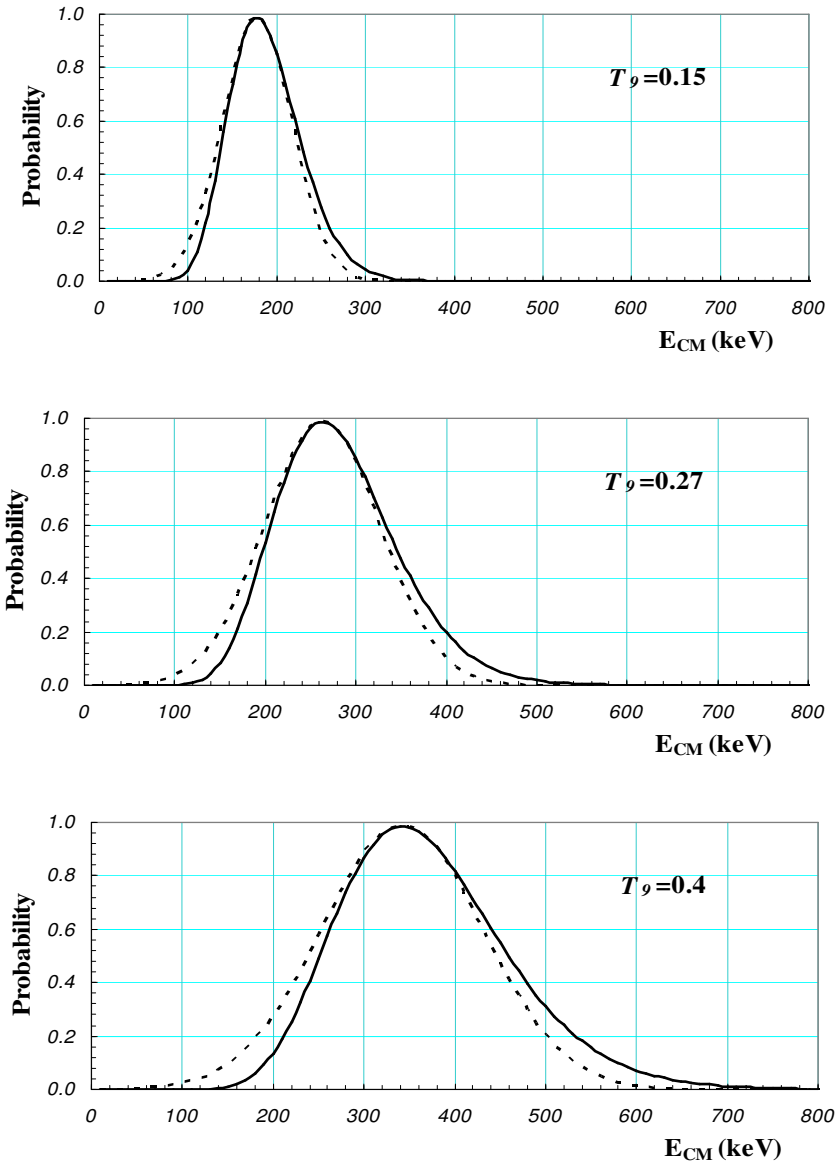

FIG. 12. The Gamow peak for the ^{22}Mg + p reaction at typical ONe temperatures. Solid lines represent the integrand of Eq. (2.14), while the dashed lines are the Gaussian approximation used in Eq. (2.18).

and the wave functions for mirror nuclei are similar, the ANCs can be extracted in ^{23}Ne which is easier to study. Charge symmetry of the nuclear force implies that the spectroscopic factors for mirror nuclei are the same, and the ratio between their ANCs is independent of the NN force. The difference in the values of the ANCs is due to the presence or absence of the Coulomb potential. By studying the relation between the mirror nuclei within a microscopic cluster model that considers the many body nature of atomic nuclei and involves the variation in nuclear structure because of the charge symmetry, Timofeyuk [59] indicates that the spectroscopic factors for $\langle ^{23}\mathrm{Ne}\,(5/2^+) \mid ^{22}\mathrm{Ne}\,(0^+)\rangle$ and $\langle ^{23}\mathrm{Al}\,(5/2^+) \mid ^{22}\mathrm{Mg}\,(0^+)\rangle$ differ by only 2%. Hence, the proton-capture reaction $^{22}\mathrm{Mg} + p \rightarrow {}^{23}\mathrm{Al}$ can be studied with the neutron transfer reaction $^{22}\mathrm{Ne} + n \rightarrow {}^{23}\mathrm{Ne}$ using stable beam and target. The ANCs of the ground state and the first excited state in ^{23}Ne will be extracted, and then transposed to the corresponding values for states of ^{23}Al.

The basic relations of this indirect technique, ANCs, can be explained in terms of the peripheral transfer reaction $^{13}\mathrm{C}(^{22}\mathrm{Ne},^{23}\mathrm{Ne})^{12}\mathrm{C}$, where the ^{22}Ne beam picks up a loosely bound neutron from the ^{13}C target. The differential cross section for the ^{23}Ne ejectile will be measured to obtain the ANCs. For this reaction, the differential cross section values can be related to the DWBA calculations by the product of the square of the ANCs

$$\frac{d\sigma}{d\Omega} = C^2_{p_{1/2}}\left(^{13}\mathrm{C}\right) C^2_{d_{5/2}}\left(^{23}\mathrm{Ne}\right) \frac{\sigma^{DWBA}_{\frac{1}{2},\frac{5}{2}}}{b^2_{p_{1/2}}\left(^{13}\mathrm{C}\right) b^2_{d_{5/2}}\left(^{23}\mathrm{Ne}\right)}. \tag{2.54}$$

To extract the value of $C^2_{d_{5/2}}(^{23}\mathrm{Ne})$, the ANC for the complementary vertex that comes from $^{13}\mathrm{C} \rightarrow {}^{12}\mathrm{C} + n$ is explicitly required. Its ANC value or the equivalent nuclear vertex constant were widely studied [60] and are knowm with uncertainties less than 6%. Also, the deduced spectroscopic factors from (d,p) and (p,d) reactions

are mutually consistent to within 15% for incident deuteron energies from 12 to 60 MeV [61].

The nuclear structure of ^{23}Ne is located in the middle of the mass region that has received significant attention for the aim of giving a microscopic description of several nuclear phenomena near the beginning of the *sd*-shell. Several studies were dedicated to measure the spectroscopic factor for the states in ^{23}Ne, mainly the bound d-wave and s-wave states. Both pick-up and knock out reactions have been performed in the form of (p,d) and (d,p) reactions, respectively, then compared with theoretical expectations. For $J^\pi = 5/2^+$, the average value for S extracted experimentally is 0.24 ± 0.03 [62], which is slightly less than 0.34 from an Oxbash calculation [63]. For $J^\pi = 1/2^+$, the value from different transfer experiments for C^2S is 0.37-0.7 in [64], and the expected value is 0.70 ± 0.03.

However, the ANCs for the same states in ^{23}Ne had not been measured experimentally prior to this work. Calculations for one-nucleon ANCs in a microscopic cluster model using two effective NN interactions in the form of Volkov (V2) and Minnesota potentials (MN) predicts that the ANC for $J^\pi = 5/2^+$ is 0.71 fm^{-1} or 0.81 fm^{-1}, respectively [59], and their average spectroscopic factor is 0.28. The ANC for $J^\pi = 1/2^+$ has the value of 16.3 fm^{-1} or 18.5 fm^{-1} from V2 or MN, respectively, with a spectroscopic factor of 1.08 [65]. This research presents the first experimental measurements of the ANCs for the ground state and first excited state in ^{23}Ne. Another self-consistent experiment reported in this dissertation is the study of the exchange reaction ^{13}C(^{12}C,^{13}C)^{12}C in order to measure $C^2_{p_{1/2}}$ (^{13}C), which is needed to complete the above experiment.

J. Extracting the ANC of ^{18}Ne from Its Mirror ^{18}O

Studying the reaction rate for $^{17}\mathrm{F}(p,\gamma)^{18}\mathrm{Ne}$ in ONe novae is important to understand the production of the elements in the HCNO cycle, and investigate the missing γ-ray from the decay of ^{18}F. The Gamow windows of the reaction for several temperatures in ONe novae are shown in Fig. 13. The rate of this reaction has been determined by applying several theoretical methods and experimental measurements. Wiescher, Görres, and Thielmann noticed that the $J^\pi = 3^+$ level in ^{18}Ne greatly influences the thermonuclear reaction rate [66]. Based on a shell model description, the s-wave proton couples with the $5/2^+$ ground state of ^{17}F to populate the 3^+ level that is located above the proton threshold, $Q = 3.922$ MeV. The predicted properties of the 3^+ state from Thomas-Ehrman shift and shell model calculations, applied to experimentally known 3^+ states of the isospin triplet T = 1 analog levels in ^{18}O and ^{18}F nuclei, estimate that the excitation energy of the level in ^{18}Ne has an average value $E_x = 4.51$ MeV [66, 67, 68]. Recent experiments have obtained precise information about the energy of the 3^+ level and its total width [69, 70]. The values of the excitation energy and the Γ_p are summarized in Table I.

Estimates of the reaction rate show that the resonant capture to the 3^+ state dominates the rate only at $T_9 > 0.5$ [71], which is an appropriate temperature for explosive events such as X-rays bursts and supernovae, while at typical nova temperatures, $T_9 \leq 0.4$, the direct capture reaction to the bound states in ^{18}Ne dominates the rate. However no direct measurements have been reported or performed yet.

The nuclear structure of ^{18}Ne depends on the configurations and the binding energy of the levels in the mirror nucleus ^{18}O taking into account the Coulomb energies.

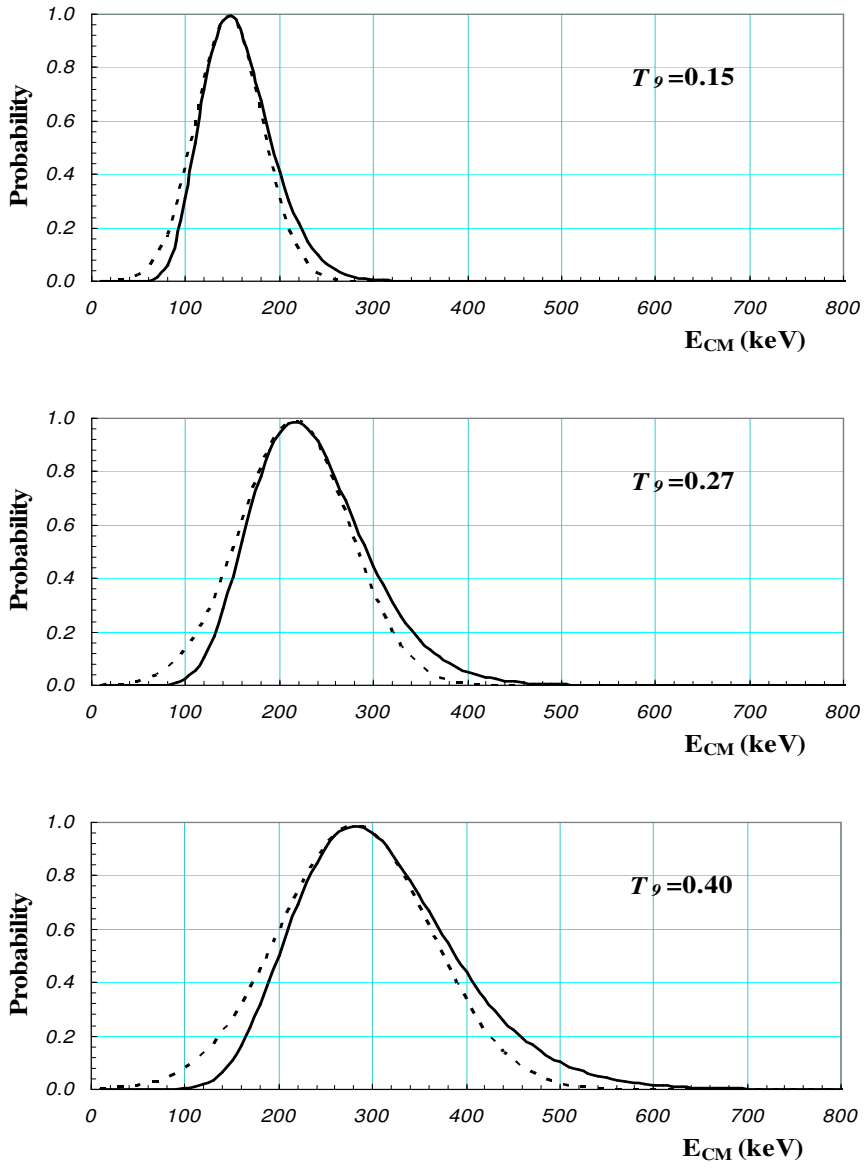

FIG. 13. The Gamow peak for the ^{17}F + p reaction at typical ONe temperatures. Solid lines represent the integrand of Eq. (2.14), while the dashed lines are the Gaussian approximation used in Eq. (2.18).

TABLE I. The Γ_p width for the resonance 3^+ state in ^{18}Ne from several experimental studies.

Reference	E_x [MeV]	Γ_p [keV]
[66]	4.328	5
[67]	4.561	22
[68]	4.642	42
[69]	4.523	18
[70]	4.527	17

Shell model calculations assume a $2s$ or $1d$ nucleon coupled to the single particle $5/2^+$, $1/2^+$, and $3/2^+$ levels of ^{17}O and ^{17}F. Comparison of the nuclear structure of the mirror nuclei for the low-lying states is listed in Table II [68]. Estimating the nuclear cross section based on the configuration of the state, and using the selection rules for one nucleon transitions within the shell model calculation, predicts that the $^{17}\mathrm{F}(p,\gamma)^{18}\mathrm{Ne}$ reaction will be dominated by direct capture to the lowest energy $J^\pi = 2^+$ states, mainly $E_x\left(2_1^+\right) = 1.887$ MeV and $E_x\left(2_2^+\right) = 3.616$ MeV [67].

Using the same arguments as in the previous sections, the ANC technique is considered as an alternative method to determine the $^{17}\mathrm{F}(p,\gamma)^{18}\mathrm{Ne}$ direct capture rate. However, analyzing the capture to these levels may be strongly affected by the non-negligible contribution of resonances, where γ-ray transitions from higher energy levels may occur. A study of the $E1$ and $M1$ contributions to the direct and resonant reaction rate and their consequences on the astrophysical S-factor is reported in Ref. [72]. More experimental inspections of resonant components are needed to disentangle their effects from the direct capture reactions.

TABLE II. Mirror states in ^{18}Ne and ^{18}O, where all the energies are in keV.

J^π	$E_x(^{18}\mathrm{O})$	E_x (^{18}Ne)	
	Expt.	Expt.	Calc.
0_1^+	0	0	-44
2_1^+	1982	1887	1877
4_1^+	3555	3376	3419
0_2^+	3634	3576	3553
2_2^+	3920	3616	3574
2_3^+	5255	5090	5022
3_1^+	5378	4525	4642

Since the spectroscopic factor for mirror nuclei are the same, the ANC method can be applied to the mirror nucleus ^{18}O to extract the ANCs for the $E_x\left(2_1^+\right) = 1.982$ MeV and $E_x\left(2_2^+\right) = 3.920$ MeV states. The suggested experiment is the peripheral neutron transfer reaction ^{13}C(^{17}O,^{18}O)^{12}C. Using a stable beam will improve the accuracy of the nuclear cross section, and increases the ability to separate the interesting levels in ^{18}O.

The nuclear structure of ^{18}O has a great theoretical interest in studying shell-model effective interactions derived from the NN force. In viewing the ^{18}O nucleus as an ^{17}O core surrounded by one neutron in the *sd*-shell, the energy levels of ^{18}O depend on the coupling of an s or d neutron to the ground state $J^\pi = 5/2^+$ of ^{17}O. $\left(d_{5/2}\right)^2$, $\left(d_{5/2}s_{1/2}\right)$, and $\left(d_{5/2}d_{3/2}\right)$ configurations lead to the population of $(J = 0^+, 2^+, 4^+)$, $(J = 2^+, 3^+)$, and $(J = 1^+, 2^+, 3^+, 4^+)$ levels in ^{18}O, respectively.

The energy gap between the $d_{5/2}$ and $d_{3/2}$ levels is of the order of 5 MeV. The pairing energy of two neutrons in the $\left(d_{5/2}d_{3/2}\right)$ configuration is 1.5 MeV, only excited states at energies higher than 7 MeV will occur [73]. Thus, the low-lying 2^+ levels will have contributions from both $\left(d_{5/2}\right)^2$ and $\left(d_{5/2}s_{1/2}\right)$, while 0^+ and 4^+ levels result from a pure $\left(d_{5/2}\right)^2$ configuration. Measurements of ^{17}O(p,d)^{18}O [74] found that the spectroscopic factor for the $E_x\left(2_1^+\right)$ is an admixture of $\left(d_{5/2}\right)^2$ and $\left(d_{5/2}s_{1/2}\right)$ configurations with the values 0.83 and 0.21, respectively. Similarly, the spectroscopic factors for $E_x\left(2_2^+\right)$ are 0.66 and 0.35 for $\left(d_{5/2}\right)^2$ and $\left(d_{5/2}s_{1/2}\right)$ arrangements, respectively. The results were obtained by fixing the geometric parameters of the Woods-Saxon potential for the radius, $r_o = 1.25$ fm, and diffuseness, $a = 0.65$ fm. Varying these geometries, (r_o, a), will change the relative magnitude of the spectroscopic factors for $s_{1/2} : d_{5/2}$ by almost 15%.

The ANCs for peripheral transfer reactions are more useful characteristics of nuclear states for calculating astrophysical reaction rates than the spectroscopic factors. Their values for lowest 2^+ states in ^{18}O have not been determined. Thus, this research reports the first measurement of the ANCs of the 1.982 MeV and 3.920 MeV levels and their relations to the determination of the $^{17}\mathrm{F}(p,\gamma)\,^{18}\mathrm{Ne}$ reaction rate. A parallel measurement was carried out to obtain the ANCs for the low-lying states in ^{18}Ne by measuring the peripheral proton transfer reaction ^{14}N(^{17}F,^{18}Ne)^{13}C with aim of populating the first 2^+ states [20]. However, no results have been published yet.

CHAPTER III

EXPERIMENTAL SETUP AND PROCEDURES

A. The Experiments

Three experiments were carried out at the Texas A&M University K500 Superconducting Cyclotron facility to measure the following neutron transfer reactions:

1. $^{13}\mathrm{C}(^{12}\mathrm{C}, ^{13}\mathrm{C})^{12}\mathrm{C}$
2. $^{13}\mathrm{C}(^{22}\mathrm{Ne}, ^{23}\mathrm{Ne})^{12}\mathrm{C}$
3. $^{13}\mathrm{C}(^{17}\mathrm{O}, ^{18}\mathrm{O})^{12}\mathrm{C}$

In addition to measurements of neutron pick-up from the loosely bound nucleus ^{13}C, measurements of the elastic scattering cross sections for the incoming and outgoing channels of each reaction were also performed. In each case, the beam was aligned to bombard perpendicular to the self-supporting 100 μg/cm^3 ^{13}C target. The energy of the beams was carefully selected to ensure that the above reactions are peripheral.

Predicting the cross section of a heavy-ion nuclear reaction can be done with the help of the T-matrix, which represents the right hand side of Eq. (2.28). It describes the probability amplitude for the transition from the incident momentum p_i to the final momentum p_f, through the action of the potential V_β. Figure 14 shows the variation of the T-matrix as a function of the orbital angular momentum ℓ for a specific example, $^{17}\mathrm{O}$ + $^{13}\mathrm{C}$ transfer reaction. The maximum value of the matrix at ℓ_o depends on the size of the system and the energy under consideration. The relation between the beam energy and the impact parameter is given by

$$b = \lambda\!\!\!^{-}(\ell_o + 1/2), \tag{3.1}$$

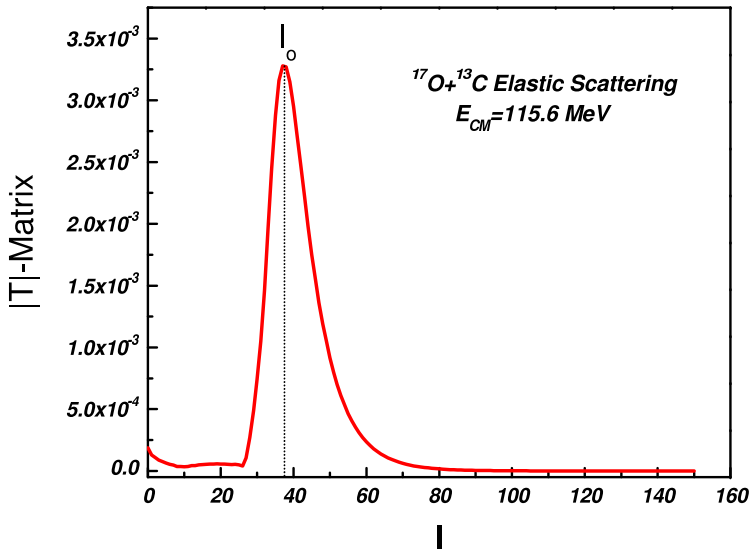

FIG. 14. The dependence of the absolute value of the T-matrix on the orbital angular momentum ℓ, where the maximum point gives information about the nuclear radius of the interaction.

where λ relates to the incident wavelength. For ^{17}O + ^{13}C at E_{lab} = 12 MeV/A, the value of ℓ_o is 37, which implies b equals 6.68 fm. The sum of the radii of the colliding particles $R = r_o(A_1^{1/3} + A_2^{1/3})$ is 5.95 fm. Since $b > R$, this implies that the interaction between the nuclei will be peripheral. An alternative way to check for the peripherality is by using the relation between the predicted DWBA calculation and the single-particle ANCs as in Eq. (2.51). When the reaction is peripheral, the ratio between them should be independent of the geometries of the Woods-Saxon potential. For example, plotting the DWBA cross section for ^{13}C(^{17}O, ^{18}O)^{12}C as a function of the single-particle ANC $b(^{18}\mathrm{O})$, as shown in Fig. 15, shows that their ratio varies by less than 3% which gives an indication that the reaction is peripheral at this energy. In addition to these considerations, the energy was also chosen to be above the Coulomb barrier to avoid the overlap between the amplitudes of the elastic scattering and the direct exchange reaction, mainly for the case of the ^{13}C(^{12}C, ^{13}C)^{12}C reaction.

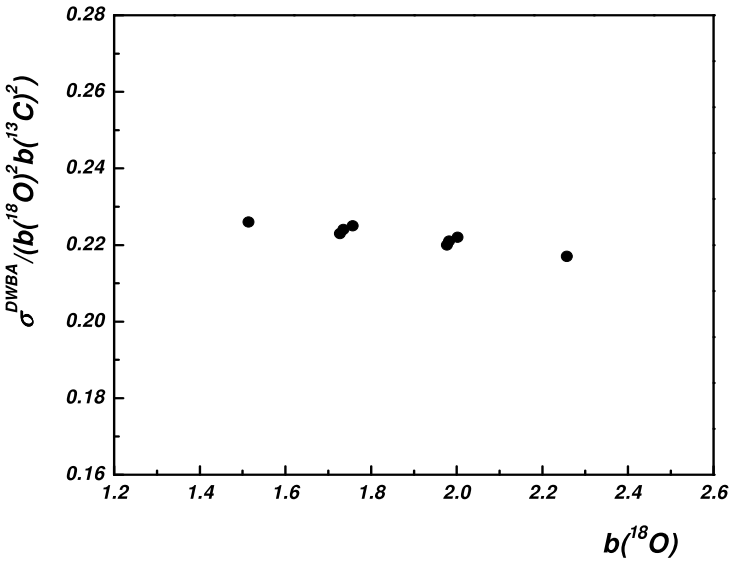

FIG. 15. The reaction ^{13}C(^{17}O, ^{18}O)^{12}C is expected to be peripheral at E_{Lab} = 12 MeV/A. The ratio between the maximum value in the DWBA calculations and the single-particle ANCs for both vertices of the reaction is independent of the choice of ^{18}O single-particle wave function when r_o = 1.1-1.3 fm and a = 0.5-0.65 fm, while the b value for ^{13}C is fixed.

B. The MDM Spectrometer and the Oxford Detector

After accelerating the ionized beam in the cyclotron, it was transported through the beam analysis system (BAS) as shown in Fig. 16. The BAS is composed of magnetic dipoles that bend the beam 175 degrees in two opposite direction 87^o and 88^o segments with intermediate horizontal and vertical focusing quadrupoles between the segments. The BAS is used to clean the beam from the slit scattered particles, to improve and control the energy and angular resolution of the beam, and to match the dispersion of the beam from the cyclotron to that of the spectrometer [75].

The ^{13}C target was located at the center of the sliding-seal target chamber of the multipole-dipole-multipole (MDM) spectrometer [76]. The MDM magnetic spectrometer, which is sitting on a moving table, was used to analyze the reaction products.

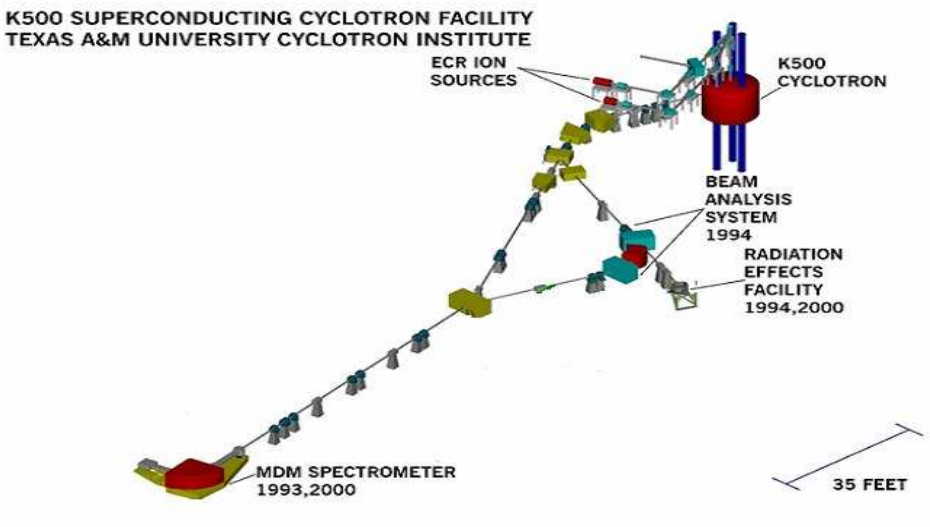

FIG. 16. The K500 Superconducting Cyclotron facility.

The operation of one main dipole magnet provides simplicity and reliability under experimental conditions. It has a maximum field strength of more than 1 T with an overall 100^o bend and 1.6 m central radius, as shown in Fig. 17. The convex curvature of the entrance opening of the big magnet body minimizes the image aberrations [76]. On the other hand, the concave boundary at the exit opening allows the incident particles to be normal to the focal plane angle, which is assumed to be in the xy-plane and particles propagate in z-direction. The median plane that lies in zx-plane is parallel to the plane of magnetic analysis with a deviation angle θ, while ϕ denotes angles in the yz-plane. These two curvatures serve as extra sextupole field components.

The spectrometer configurations are adjusted by the magnetic fields of the single dipole and the multipole in front of it for the aim of achieving larger dispersion, low magnification, and higher mass-energy products. For the measurements reported here, they are usually set to transport either the elastically scattered beam or the

nuclei that picked up a neutron from the target. The values of the magnetic elements were determined by using the RAYTRACE computer code [77]. RAYTRACE tracks the path of the particles beginning from the output of the target chamber, then through the MDM magnet to the end of the detection area, taking into account the geometries of the MDM spectrometer and the magnetic multipole components.

The modified Oxford detector [78] was used to observe the reaction products. The detector has multi-functional capabilities. It has been used to identify the particles and measure their positions along the dispersive x-direction. By measuring the direction of the particles in the xz-plane, we can reconstruct the scattering angle at the target as a function of the beam deviation in the detector.

The Oxford detector is an ionization chamber [79] with entrance and exit windows in the external box of the chamber. These windows were made of 25 and 50 μm thick polyethyelene (Mylar) foil, respectively. Their dimensions are large enough for the utilization of the full efficiency of the detector. The chamber was filled with pure isobutane gas at low pressure 30-50 Torr. Isobutane has been chosen due to its great stopping power and minimal multiple scattering of the ions for a specific energy loss. Important precautions were considered to reduce the contamination of the gas. The detector volume was connected to the spectrometer high vacuum system. Once the pressure went almost to zero, the isobutane was pumped into the chamber. In order to minimize any further impurities of the gas during the experiment, a low-cost flow-regulation system was installed to slowly refresh the isobutane in the chamber without affecting its required pressure value. The energy of the beams was selected to be sufficient so that the reaction products would lose part of their energy in the ionizing the gas and the Mylar windows, and stop completely in a NE102A scintillator

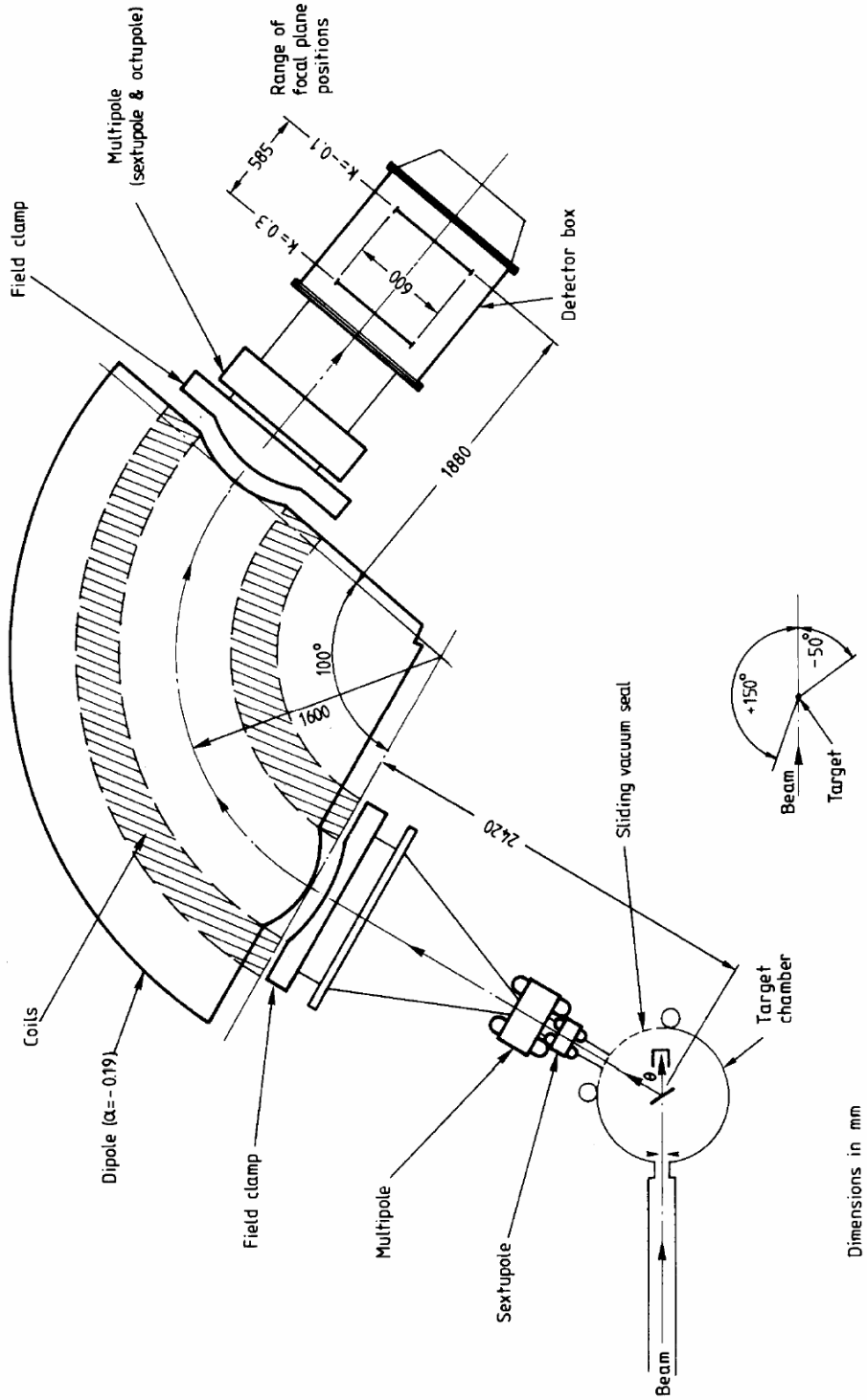

FIG. 17. A layout of the MDM spectrometer, extracted from Ref. [76], shows all of the magnetic components and their locations relative to the target chamber and the detector box.

located in the air, about 42 mm behind the exit window.

The inside structure of the detector, as shown in Fig. 18 and Fig. 19, consists of two electrodes to measure the ion energy loss and four resistive avalanche counters (ACs) to determine the position of the particles in the focal plane and their deviation angles. The detector has a multi-wire Frisch grid that is designed to be 10.5 cm above the cathode to minimize the possibility of multiple scattering positive ions that may pass through the grid or hit the cathode. Another four small (screening) grids beneath the ACs were added to shield the lower Frisch grid from escaping positive ions produced in the ACs' shells. The voltages are chosen so these grids are transparent to electrons drifting upward.

A rectangular frame of G10 glass fiber was designed to support the wires of the grids. Grooves were added to the frame to space the wires uniformly. Each 80 μm Be-Cu wire was straightened and tensioned by hanging weights on both ends, then epoxy glue was applied to keep it taut and place it dominantly in the groove. Finally, it was soldered to the attached circuit boards along the edges of the internal body of the detector for electrical contact. To correct the electric field between the electrodes, fourteen 80 μm Be-Cu field shaping wires with double banks, 7 mm separation between each two banks and 7 mm vertical spacing, were added around all the four sides of the detector. The particles are then identified by measuring the energy loss in the ionization chamber and measuring the residual energy in the scintillator.

To measure the position of the particles in the focal plane, four resistive wires (ACs) were used. The ACs are located at four different depths within the detector, parallel

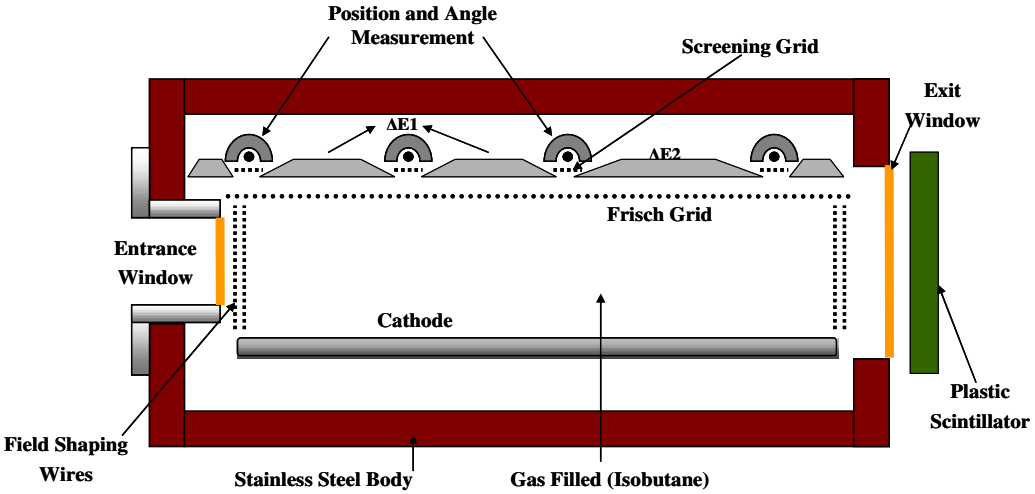

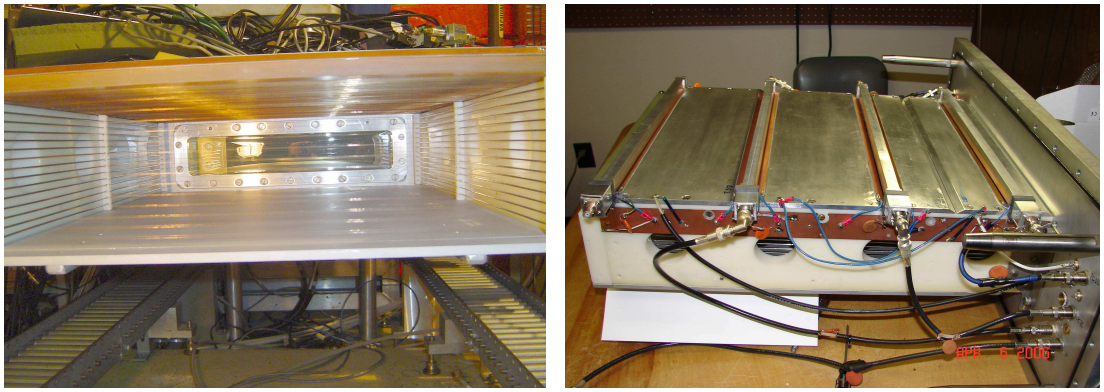

FIG. 18. The upper drawing represents a cross section view of the Oxford detector with its main internal parts. The field shaping wires along the sides of the detector, the Frisch grid, and the front window covered with Mylar foil are shown in the bottom left picture. The position of the four ACs, the anode plates, the connection cables, and the attached circuit boards along the edges of the detector are shown in the right picture.

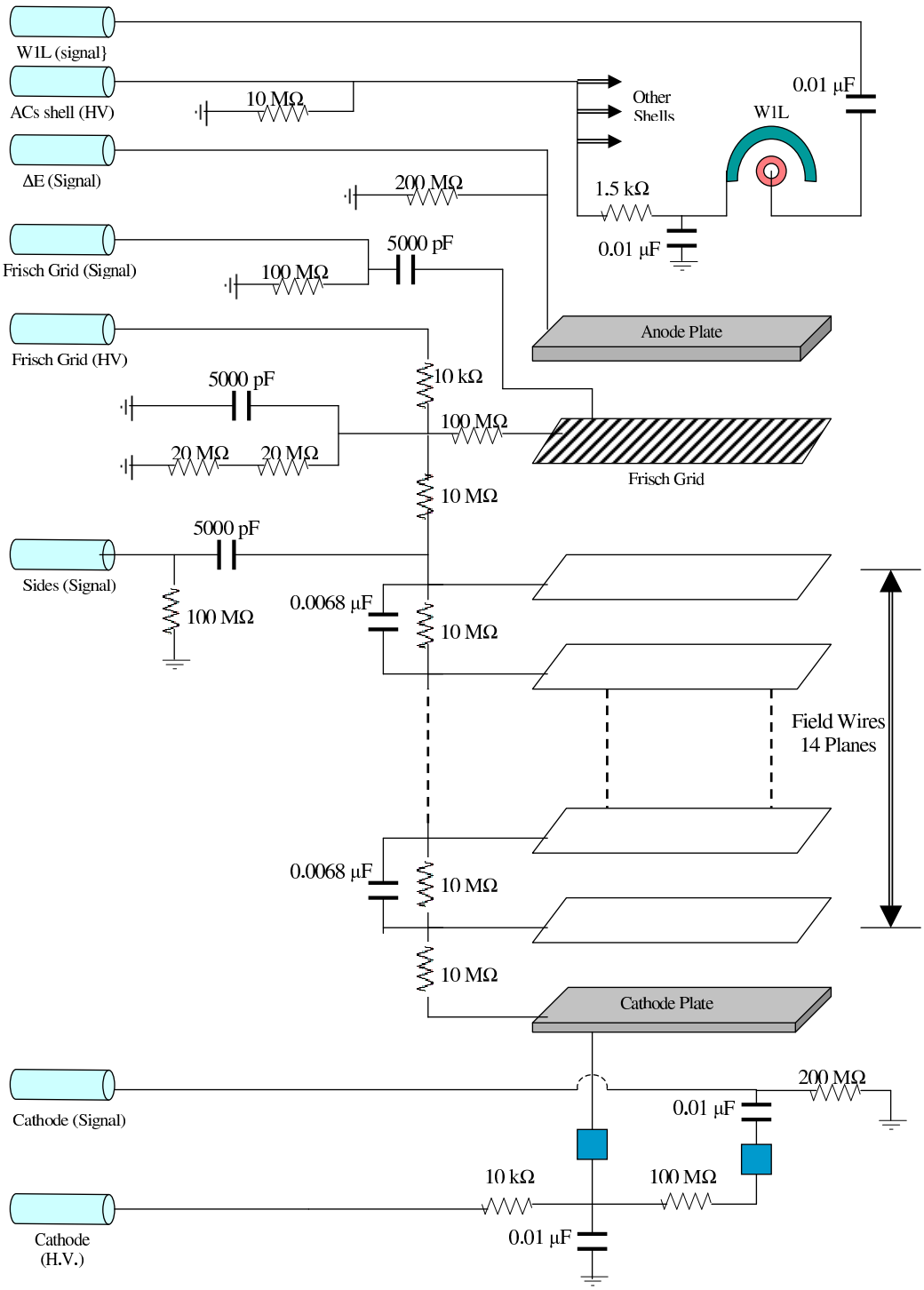

FIG. 19. The electrical circuits that connect the internal parts of the Oxford detector in order to apply HV and get the signals that will be sent outside the detector to the amplification system.

to the focal plane and separated by 16 cm each. The first wire is 2 cm behind the entrance window. The body (shell) of each AC is 40 cm length and is made of a rectangular aluminum bar with a U-shaped groove. A 10 μm Ni-Cr wire (anode) was tensioned and soldered to coaxial connectors at each side of the counter. A power supply with smoothly increasing voltage was used to avoid the breakage of wires when high voltages were applied. When a few electrons drifting up penetrate through the grid into the AC, the applied fields accelerate them toward the center of the wire. An avalanche is generated in a tiny distance along the wire comparable to its diameter. The position of the incident electrons along the wire is determined through charge division. The charge drifts to both ends of the wire, then is collected by two amplifiers. Since the anode wire has a significant resistance per unit length, the position of the interaction is determined by dividing the output signal of either amplifier by the sum of the two. The confinement of the avalanche to a small area allows good position resolution along the wire. The detector angle is then determined by tracking the path of the ions using the position signals in two of the four ACs.

C. The Data Acquisition System and Electronics

Collecting the data required monitoring and saving 8 signals from the ends of the four resistive wires, 2 energy loss (ΔE) signals, 2 residual energy (E_r) signals from the scintillator, and 2 signals from the cathode and field shaping wires (sides). All these signals were processed by preamplifiers and amplifiers, then digitized and sent to CAMAC ADCs as shown in Fig. 20. The high voltages (HV) applied in the detectors were optimized empirically depending on the particles and their energies, and the gas pressure. The applied HV on the wires were around 1 kV.

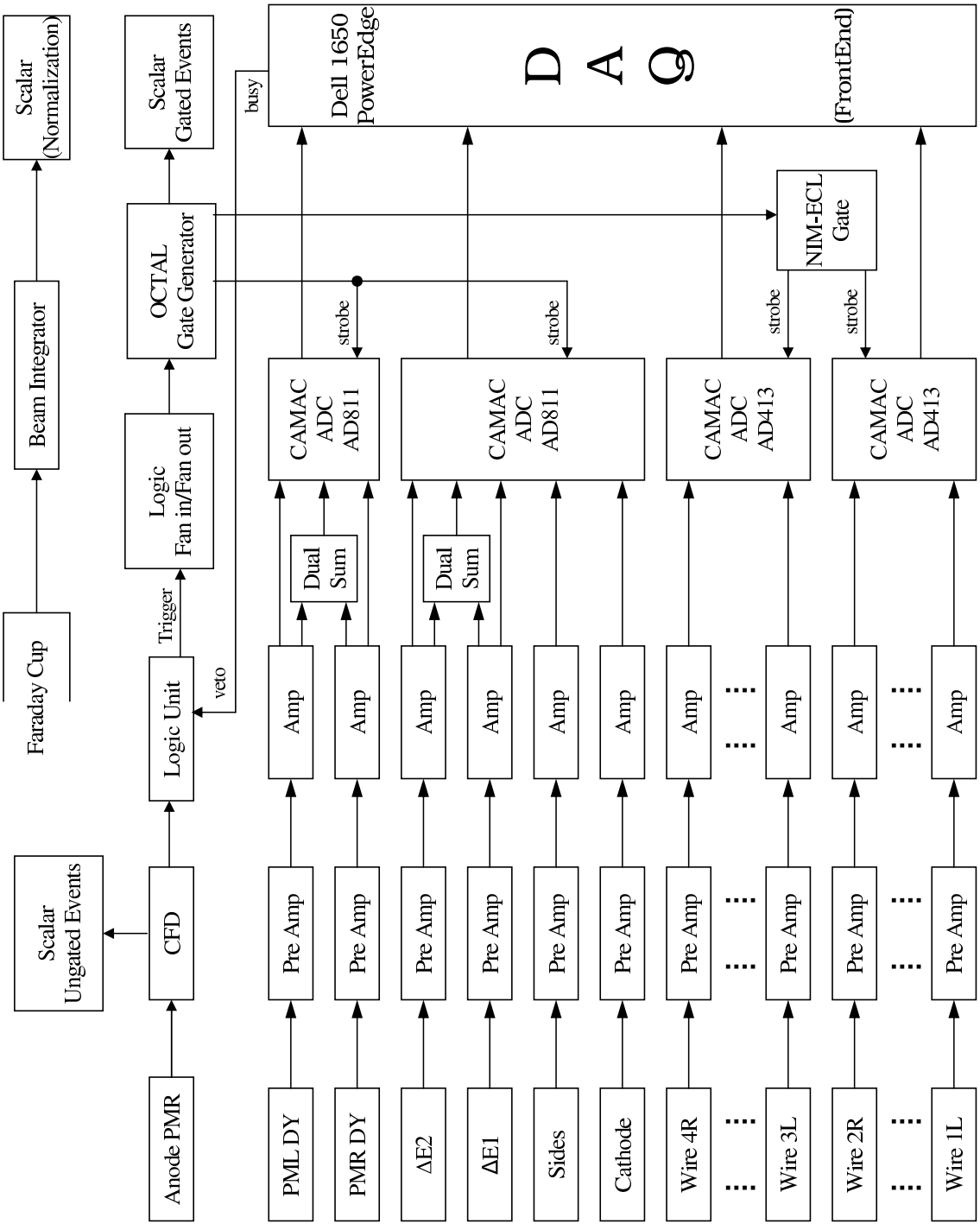

FIG. 20. The sketch shows the signal processing and data acquisition electronics for the MDM spectrometer.

A pulser signal was sent to the left and right ends of each wire to match the amplification gain in the electronics. Then the position signal was determined in the data analysis software using

$$P = A\frac{L}{L+R}, \tag{3.2}$$

where L and R are integer numbers resulting from the digital conversion of the analog signals, and A is the number of the channels in the AD413 ADC. The resolution of the wires using the pulser peak was 0.4 mm FWHM. The angle deviation of the beam was measured depending on the information of their position signals and the distance between them.

The anode plane is made of four adjacent plates. The first three plates were connected by conductive wires as shown in Fig. 18 to give a ΔE1 signal that covered almost 70% of the detection area, while the last plate near the exit window gave the ΔE2 signal. The two signals were added using a Dual Sum and Invert module. Their resolutions depended significantly on the energy of the beam and the gas pressure in the ionization chamber. The HV between the electrode plates was of the order of 700 V. Since the AC bodies are close to the anode plates, any crosstalk problem due to increasing the HV of the resistive wires was eliminated by inserting 10 nF capacitors between the ACs and ground. The sides signal was taken to account for the energy loss of the beam in the region away from the center of the detector and near the field shaping wires since the cathode and the Frisch grid do not form a complete Faraday cage [79]. Also the cathode signal was included in the acquisition system to be coupled with the ΔE signals to get a better resolution. However, we faced noise problems with these two signals that reduced their benefits, and therefore they were neglected.

The particles were stopped by depositing all their residual energies in a 1.3 cm thick NE102A plastic scintillator. The E_r signals were taken from two photomultipliers (PM). Their circular photocathodes are connected to the left and right sides of the flat sheet of the scintillator via plexiglass light guides. Negative 1600 V was applied on each PM as recommended by the manufacturer. The PMs were tested with a strong radioactive source before being attached to the MDM to check for sources of noise or any external light leak. Both the left and right dynode signals, which represent the overall gain of the PM, were sent through the amplification process to an AD811 ADC. The signals were also summed in the hardware system to get a general picture of the energy deposited in the scintillator. They were used with the ΔE signals for particle identification.

Because the time response of the scintillation detector is short relative to the ACs, the anode output pulse of the right PM was used as the electronic logic signal to activate several operations such as the recording instrument. A constant-fraction discriminator (CFD) was used to accept all the incoming signals with pulse heights greater than its threshold, then convert them to logic signals. The threshold was set above the noise level. The logic signal was then passed on to a coincidence logic unit, which has another input signal from a CBD 8210 module that was used to veto events when the data acquisition system was busy. This system, as shown in Fig. 20, included a VME frontend and a backend host computer. The VME frontend consisted of a VME crate with a Motorola MVME 712/M Ethernet interface module and the CBD 8210 module. The backend host computer was a Dell 1650 PowerEdge server that connected with the frontend by an Ethernet cable. When the computer was not busy processing the events, a trigger pulse from the logic unit was fed to a fan in/fan out unit to divide the logic signal into several identical signals, then send

them to a gate generator. The gate generator produced adjustable width gate pulses to activate the ADCs to read out the signals from the amplifiers. The dead time of the acquisition system was determined from the ratio between two scalars. The first one counted the total number of anode pulses by reading directly the output of the CFD (ungated events), while the other scalar counted the events after being gated.

D. The Preliminary Analysis of the Raw Data

An interactive data analysis manager was developed under Linux using ROOT frameworks with C++ language. This ROOT macro was the premier platform for the data analysis, where raw data were monitored and saved simultaneously during the experiment.

Directly after the target chamber, a slit-box was added to the beam line to contain three different masks. A single-slit mask with one 0.1^o opening was used to examine the energy of the incident beam. This was done by investigating the magnetic rigidity ($B\rho$) of the MDM and the acceptance limit of the Oxford detector. The dipole magnetic field was increased and decreased to points where the PMR signal rate dropped almost to zero, which indicated that the elastically scattered beam hit the sides of the front window of the detector. The median value of $B\rho$ between these limits was then used to determine the beam energy. The second mask has five openings (5-finger) of $\delta\theta = 0.1^o$, located at -1.54^o, -0.77^o, 0^o, 0.77^o, and 1.54^o relative to the central angle of the spectrometer. This mask was used for detector calibration as will be discussed in the next section. The last mask has a wide opening that restricted the acceptance of the detector, but increased its efficiency, horizontally to $\Delta\theta = \pm 2^o$ and vertically to $\Delta\phi = \pm 0.5^o$. Measuring the whole range of the angular distribution

for the elastic scattering and the transfer reaction required moving the spectrometer by 2^o or 3^o at a time to allow for an angle overlap that provided a self-consistency check of the data at all angles.

An example of the wire signals can be seen in Fig. 21, taken with a ^{22}Ne beam incident on a gold target, ^{197}Au, when the spectrometer angle was 5^0. The Rutherford scattered beam passed through the 5-finger mask and followed five trajectories at different angles. The left and right pulse heights were inserted in Eq. (3.2) to determine the location of each trajectory in the wire, then combined with the position information from the other wires to specify the path of the beam in the detector. The amplitudes of the pulses were also examined to adjust the applied HV on the wires to avoid loosing signals on the their edges.

Typical examples of the E_r and ΔE pulses are shown in Fig. 22, where the ^{13}C target was bombarded by the ^{22}Ne beam. The results of the reaction passed through the $4^o \times 1^o$ mask and the MDM was set at 5^o, which allowed measuring the angular distribution in the range of 3^o-7^o at once. Filling the histogram of ΔE versus E_r in the ROOT macro identified all the particles that were observed by the detection system. Running a Monte Carlo simulation assisted in defining the particles that needed to be studied. The analytical details will be discussed later in Chapter IV.

E. Oxford Detector Calibrations

1. Position Calibration

The position calibration was performed to determine the trajectory of the scattered or produced particles along the dispersive x-axis and in the focal plane. The main

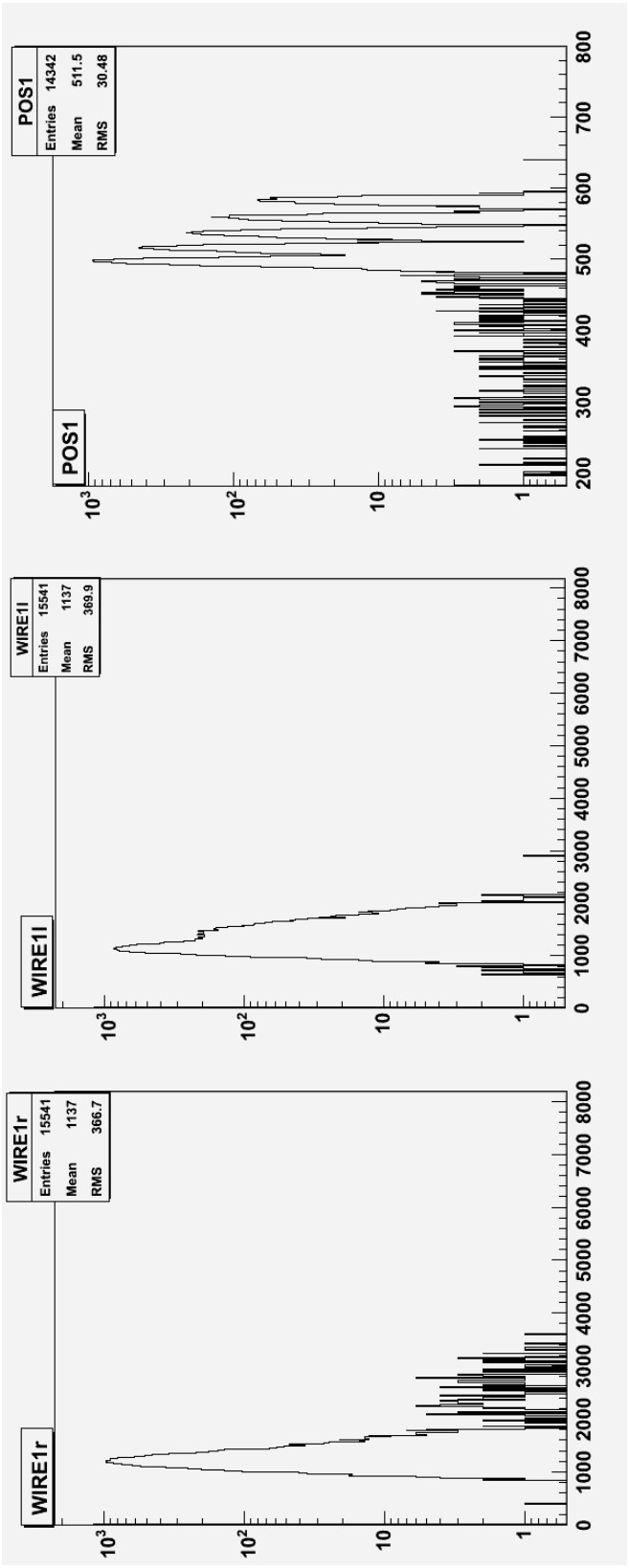

FIG. 21. The left and middle pictures show the hardware logic signals from the left and right ends of the first wire in Oxford detector after the beam passed through the 5-finger mask. The right picture illustrates the online determination of the position signal, where the five trajectories are clearly separated.

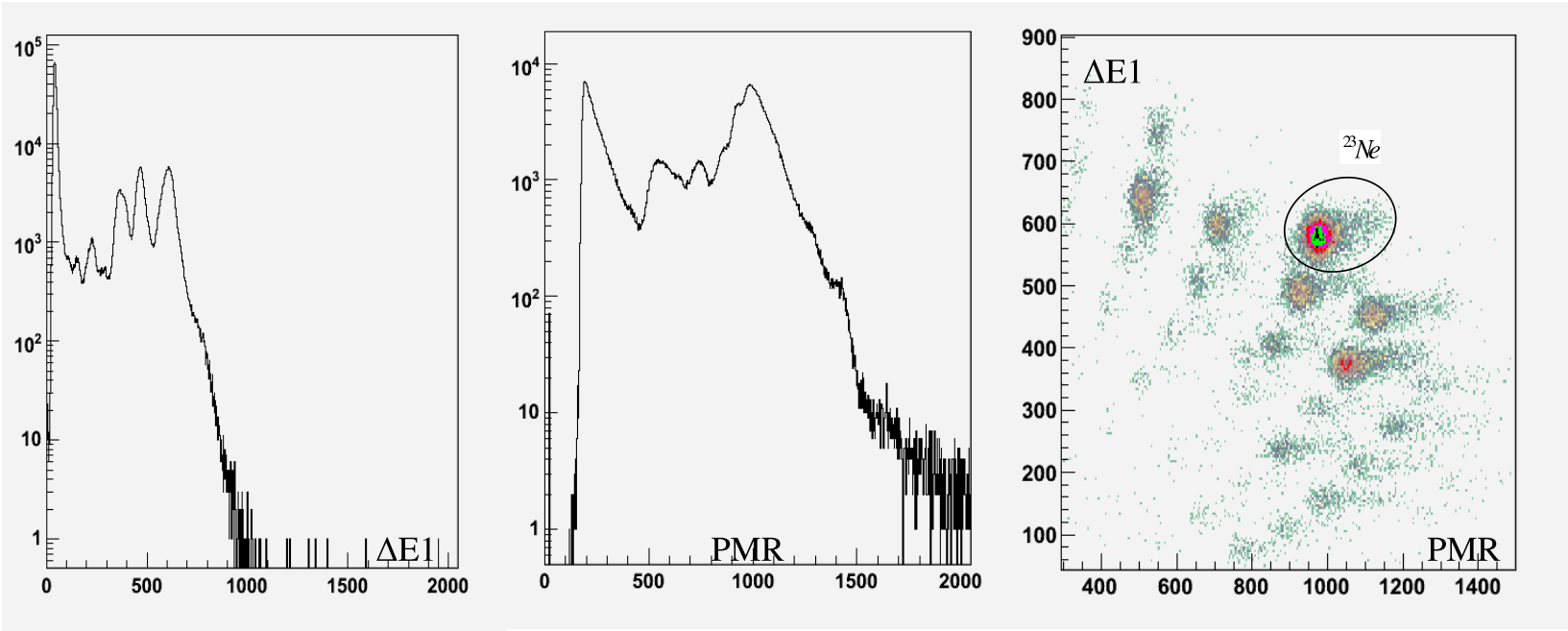

FIG. 22. The gated pulse from the ΔE1 and right side of the scintillator (PMR) signal are shown in the left and middle pictures, respectively. At right, the two dimensional ΔE-E_r spectrum shows the quality of the particle identification obtained. The position of ^{23}Ne is identified by the circle.

objective was to calibrate the position spectrum in Fig. 21 for each of the four wires. To do that, the beam bombarded a ^{197}Au target with MDM at 5^o. The kinematics of the reaction were determined to obtain the $B\rho$ in the middle region of the detector. Since the range of $B\rho$ values for the scattered particles to pass through the detector were specified with the single-slit mask, the 5-finger mask was used to measure the trajectories of the particles for four different $B\rho$s covering the full length of the resistive wires. RAYTRACE was used to calculate the corresponding positions on each of the four resistive wires (in centimeters). Then, the calibration was made by matching the positions calculated (POSC) by RAYTRACE with the measured positions (POS) given by Eq. (3.2) as shown in Fig. 23. The positions and angles of the particles on the first wire were easily separated. Depending on their measured angles when they crossed the first wire and the separations between the four wires, their positions on the other wires are determined by

$$x_{ij} = x_{1j} + D_i tan(\theta_{1j}), \tag{3.3}$$

where i refers to the second, third, and fourth wires, while 1 is for the first wire. Each trajectory is represented by j. Before the beginning of each experiment, RAYTRACE was also used to identify the position of the focal plane, which was used to fix the optimal distance between the Oxford detector and the MDM in order to keep the focal plane in the detector, while changing the spectrometer angle.

2. Angle Calibration

The deviation angle of the particles in the detector θ_d was measured from their position in any two of the four wires. To get the angle of the reaction at the target θ_t in the analysis of the data, RAYTRACE was used to obtain θ_t as a function of θ_d. Unlike the position calibration, the angle calibration was done using only RAYTRACE.

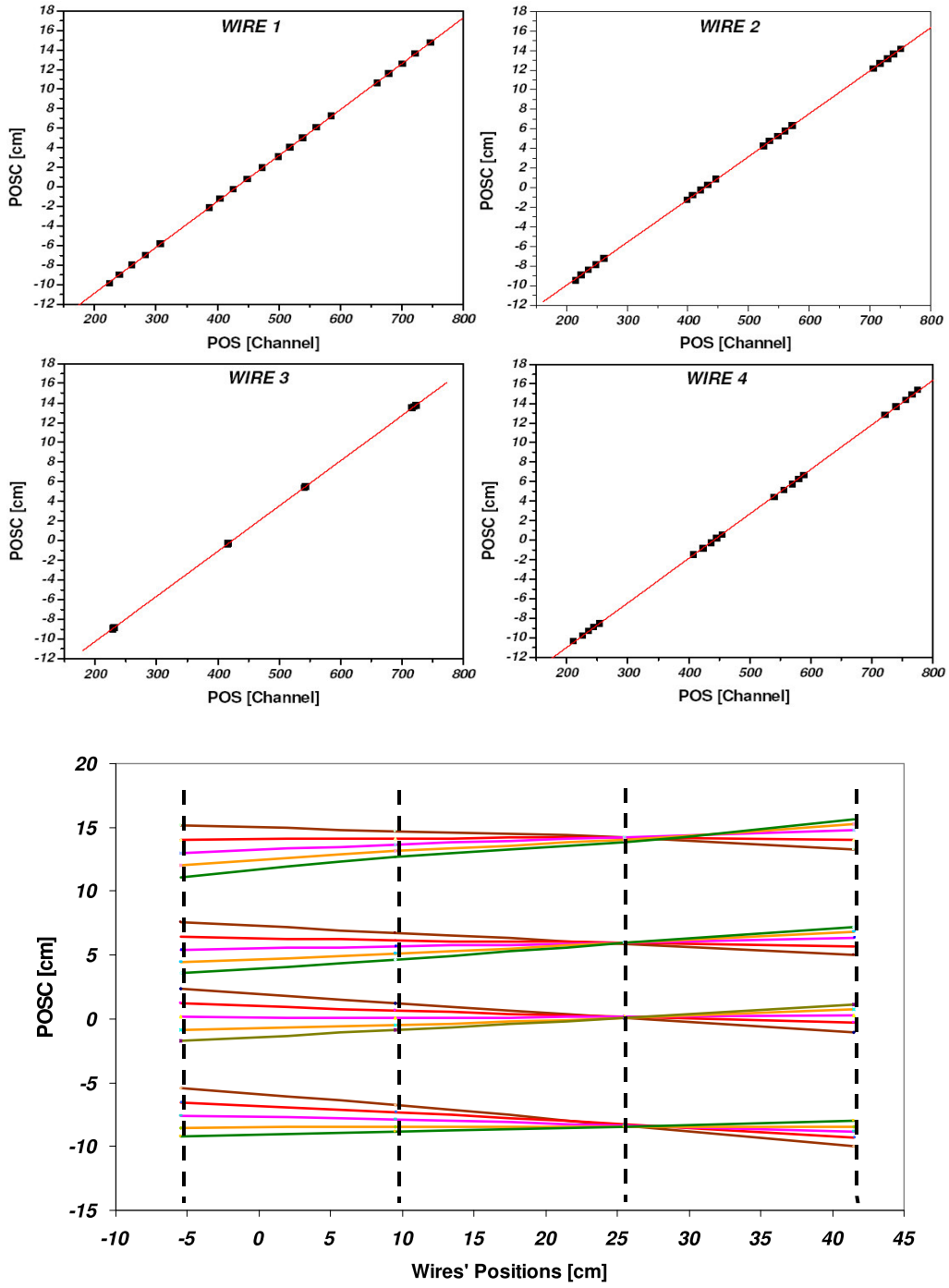

FIG. 23. The ^{22}Ne beam scattered on the ^{197}Au target at 5^o spectrometer angle and the 5-finger mask was used. The wires' figures show the linear correlations between the POS and POSC to get the position calibration. The bottom figure shows the trajectories of the scattered particles on each wire for four $B\rho$ values. The position of the focal plane is clearly on the third wire.

The calculation of θ_d was performed at seven θ_t angles for several beam energies at the same $B\rho$ in the MDM. A second degree polynomial relation was found between θ_d and θ_t angles for each incident energy as in the following relation:

$$\theta_t = A + B\theta_d + C\theta_d^2 \tag{3.4}$$

Changing the beam energy in RAYTRACE will change the position x of the particles in the focal plane, and the parameters A, B, and C are functions of the beam energy, or simply they are functions of the focal position x. In another words, x depends on the momentum and deviation angle of the particles after colliding with the target, so $x \equiv f(p, \theta)$. This dependence can be approximated to the first order by a Taylor series:

$$x = x_o\,(p_o, \theta_0) + (\theta - \theta_o)\,\frac{\partial x}{\partial \theta} + (p - p_o)\,\frac{\partial x}{\partial p} \tag{3.5}$$

The first term is related to p_o and θ_o, the values of the momentum and angle directly after the particles interact with target. The second term gives the magnification of the outgoing beam in the spectrometer, and it depends on the settings of the MDM and the z-location of the focal plane. The last term depends on the kinematics of the reaction. The momentum p of the particles in the detector can be written as $p = p_o(1+ k(\theta)\delta\theta)$. This can be rearranged to use the kinematics factor $k\,(\theta) \equiv (1/p_o)\,dp/d\theta$, which is defined as the fractional variation of momentum with the scattering angle. The dispersion of the beam in the focal plane (in units of cm/%) is $D_x = \frac{\partial x}{\partial p/p_o}$. At the focal plane, the effects of the magnification and kinematics terms cancel each other. Therefore, the position x depends only on p_o and θ_o, and the constant parameters A,

B, and C are related to x using:

$$\begin{aligned} A &= A_1 + A_2 x + A_3 x^2 \\ B &= B_1 + B_2 x + B_3 x^2 \\ C &= C_1 + C_2 x + C_3 x^2 \end{aligned} \tag{3.6}$$

where A_i, B_i, and C_i are the final calibration parameters. An illustration of the calibration is shown in Fig. 24. The angle calibration was calcualted for each spectrometer angle and each outgoing particle that was intended to be studied. Then it was checked online with the 5-finger mask at several locations of the MDM for any further adjustments.

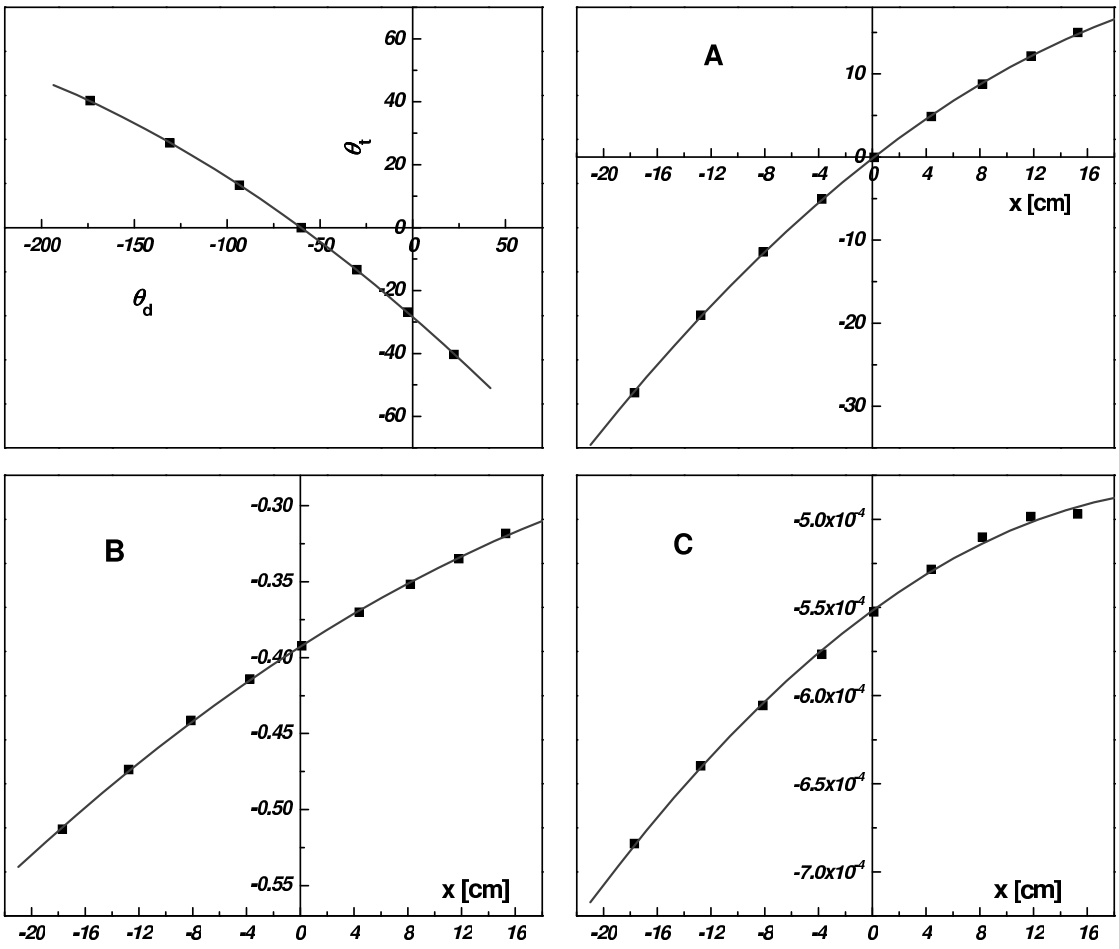

FIG. 24. The figures show a specific case, which represents bombarding the ^{13}C target with ^{22}Ne beam, where the spectrometer angle was at 5^o. The relation between the angles at the target (θ_t) and the detected angles at the detector(θ_d) was calculated at seven θ_t angles: 0^o, $\pm 0.77^o$, $\pm 1.54^o$, and $\pm 2.31^o$. Then, it was fit by a polynomial function to obtain the values of A, B, and C. Those parameters were drawn as functions of the dispersive x-axis in the detector for several incident energies of the beam to get the final parameters, which were used for the angle calibration.

CHAPTER IV

DATA ANALYSIS AND EXTRACTING THE ANCS

A. The Differential Cross Sections

When the flux of incident beam irradiates the surface area of the target, the probability to observe scattered particles per solid angle unit is proportional with the differential cross section defined as

$$\frac{d\sigma}{d\Omega} = \frac{\text{Scattered flux/Unit of solid angle}}{\text{Incident flux/Unit of surface}}. \tag{4.1}$$

In order to determine the differential cross sections [in units of b/sr] the definition from Eq. (4.1) becomes

$$\frac{d\sigma}{d\Omega}(\theta) = \frac{Y(\theta)}{N_t N_{FC} \Delta\Omega(\theta)}, \tag{4.2}$$

where the yield $Y(\theta)$ represents the the number of events of a given type that were measured in the Oxford detector at a specific scattered angle $\theta \pm 1/2\Delta\theta$. $\Delta\Omega(\theta)$ is the solid angle under which the collected scattered flux was allowed to enter the MDM and travel to the detection box, and its value depends on the mask that had been selected in the slits-box. The last components in the dominator of Eq. (4.2) are the number of target centers N_t (the thickness of the target in atoms/cm^2) and N_{FC} the total number of the incident particles on the target. The beam was stopped in a Faraday cup, where its collected charge was converted in the beam integrator into total charge Q and was measured by a scaler, as shown in Fig. 20. N_{FC} was then determined by dividing this integrated charge Q by the charge of the beam q_i ($+Ze$ in our case as at our energies the beam is fully stripped after passing through the target).

Measurements of the thickness of the Au, ^{12}C, and ^{13}C targets were performed online with two different beams using a double-target method. First, the ^{22}Ne beam at 12 MeV/A bombarded a thin gold target, and the elastic scattering (pure Rutherford) was measured with the MDM at 5^o. The position of the elastic peak along the dispersive x-axis in the focal plane of the detector was determined. Then the ^{13}C target was added in front of the Au target while keeping the spectrometer unchanged and the new position of the elastic scattering along the x-axis was measured. The measured difference in positions due to the supplementary energy loss of the ^{22}Ne beam in the ^{13}C target was transformed into energy loss using RAYTRACE. The ^{13}C thickness was determined from this energy loss using the TRIM code [80].

A similar procedure was followed to determine the thickness of the Au and ^{12}C targets. The thicknesses were remeasured again online with the ^{17}O beam, then rechecked offline with a radioactive ^{228}Th α-source. The average thickness of the ^{13}C target is 104 ± 8 μg/cm^2, ^{12}C is 109 ± 9 μg/cm^2, and one of ^{197}Au targets is 219 ± 17 μg/cm^2. A 7.5% accuracy was assigned to the absolute values of the differential cross sections due to the precision in determining the thickness of the targets.

Since for high Z targets at our beam energy and small angles the reaction will be pure Coulomb scattering, the Au target was also used in the experiments to test the efficiency of the Faraday cup in order to get the correct normalization of the cross section values. For a specific case, the scattered ^{17}O particles were measured at spectrometer angles of 4-8 degrees. The yield was then compared with the calculated Rutherford scattering as shown in Fig. 25 to give a normalization factor of 1.02. This process was neglected for the experiment that included the ^{12}C beam because the N_{FC} number was not recorded correctly. On the other hand, the ^{22}Ne beam experiment

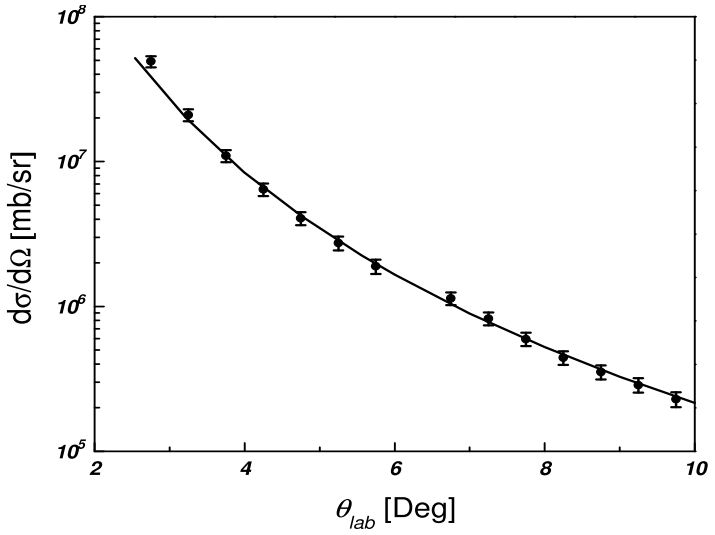

FIG. 25. The elastic scattering of ^{17}O on Au at 204 MeV is compared to the Rutherford scattering at small laboratory angles. The 1.02 factor between measurements and calculations indicates that normalizing the data with Faraday cup is good.

required a Faraday cup normalization factor of 30%.

B. The ^{13}C(^{12}C,^{13}C)^{12}C Experiment

Interactions between the ^{12}C and ^{13}C nuclei with well-established shell structures have been widely studied. They provide precise and consistent methods to study single-nucleon transfer reactions, where spectroscopic factors and vertex constants, or ANCs, are wanted. The ^{13}C(^{12}C,^{13}C)^{12}C reaction has identical entrance and exit channels, which may lead to an overlap between the elastic scattering and elastic transfer reactions. The current part of the research investigates the effect of the overlap when the energy of the incident ^{12}C particles is above the Coulomb barrier. On the other hand, choosing a transfer reaction with the same initial and final states reduces the dependence on different spectroscopic factors to the square of one. From

these transfer data, the ANC of the ground state in ^{13}C can be obtained, then used in other neutron transfer reactions that involve a ^{13}C target and are performed for the purpose of ANC measurements.

1. Elastic Scattering Data

The ^{12}C beam at 10.6 MeV/A impinged on the ^{13}C target. The elastic scattering angular distribution was measured at several spectrometer angles. Overlapping measurements were performed for consistency checks of the data at all angles, as shown in Fig. 26. Selecting the scattered ^{12}C particles in the ground state from (ΔE,E) and (TargetAngle,position) histograms from the raw data was clear since the contributions from excited states either of the incident or the target nuclei came at lower energies. However, an additional constraint was added on the data to avoid any back or side scattering of the particles in the MDM walls or in the ionization chamber. Therefore, a gate was set on the difference between the detector angle found from the position in the first and fourth wire and that found using data from the first and third wire.

The raw data show that the elastic scattering band in the (TargetAngle,position) histogram, Fig. 27, partly overlaps with other bands of different slopes at very small angles (below $\theta_{lab} = 5^o$). Analysis found those bands to be related to very small amounts of heavy impurities in the ^{13}C target, most likely Ta and Si, along with O. Since interactions with Ta and Si are pure Rutherford scatterings at very forward angles, their expected contributions are subtracted from the data to obtain absolute values of the cross section. The ^{16}O contamination in the target was treated differently. Figure 27 shows that the elastic scattering of the $^{12}\mathrm{C} + ^{13}\mathrm{C}$ band is completely separated from the $^{12}\mathrm{C} + ^{16}\mathrm{O}$ band for laboratory angles larger than 8^o. The ratio

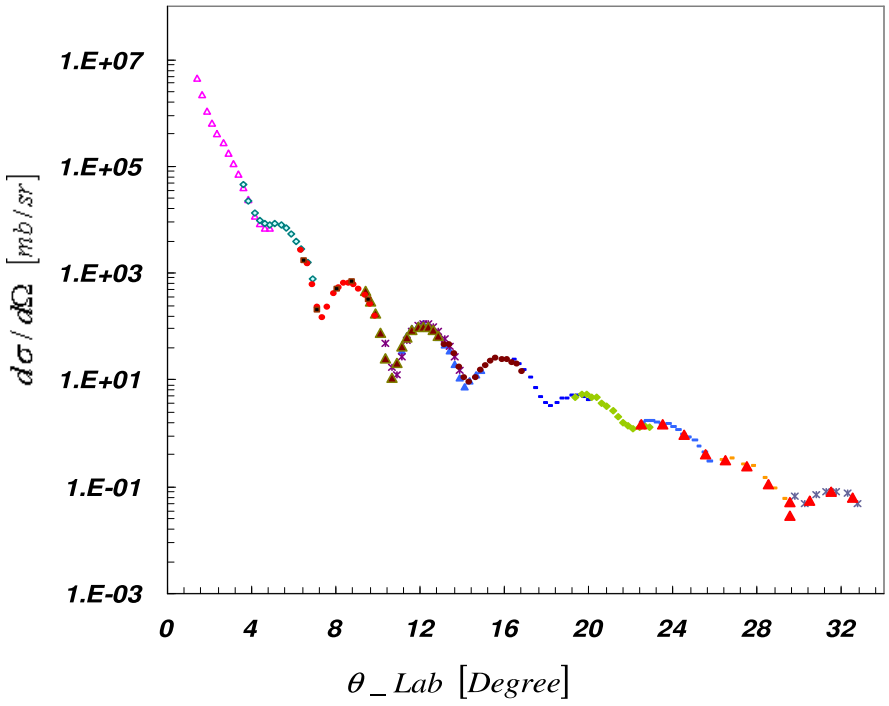

FIG. 26. The elastic scattering angular distribution measurements of ^{12}C+^{13}C at several spectrometer angles. The well-overlapped data points show the reproducibility of the cross section data when the MDM rotated to large angles.

between their bands for the angular range 8^o-10^o shows that the ^{12}C+^{16}O yield is only 5% of the ^{12}C + ^{13}C scattering. Taking this factor into consideration, the predicted elastic scattering angular distribution for O is on average 8% of the corresponding distribution for C, therefore its contribution is neglected. Consequently, the elastic measurements in the laboratory frame are good from 2^o-33^o, which is 4^o-63^o in the center of mass frame.

The measured elastic scattering cross section is shown in Fig. 28 as the ratio to the Rutherford cross section. The measurements with the 5-finger mask showed that the overall resolution in the laboratory scattering angle was $\Delta\theta_{res} = 0.23^o$ full width at half maximum (FWHM) at small angles, and it increased to $\Delta\theta_{res} = 0.4^o$ at

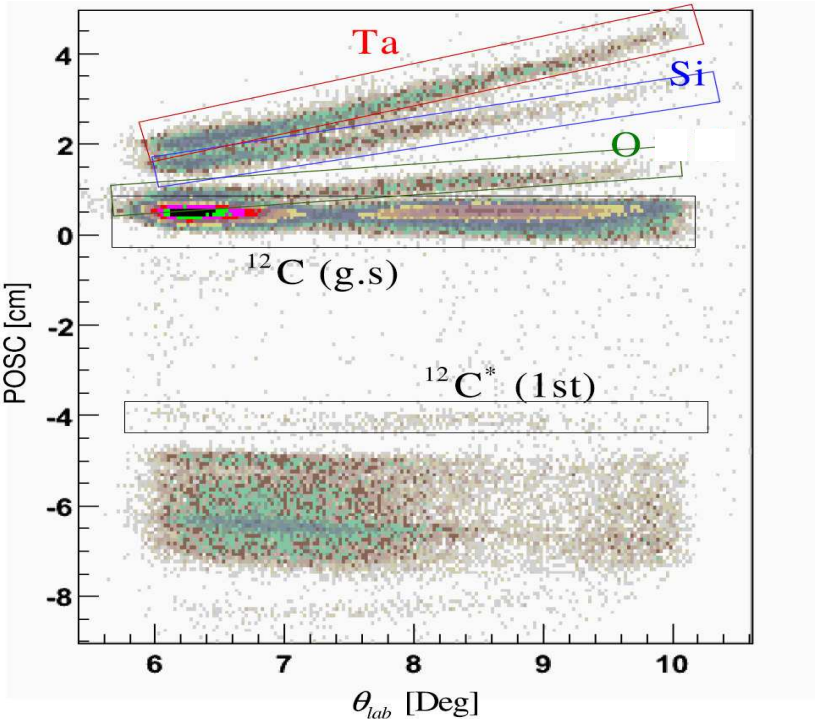

FIG. 27. The impurities in the target are shown in the (θ_{lab},POSC) histogram, which were identified using RAYTRACE and the kinematics of the reaction. The analysis found that Ta and Si have almost 1% concentrations in the ^{13}C target, and they affect extracting the data at laboratory angles less than 4^o. The wide band below -4.3 cm in the POSC-axis may consist of several excited states in ^{13}C above 5 MeV, but the limited energy resolution increases the difficulties of identifying the J^π of those states.

larger angles. This includes a contribution from the angular spread of the beam of about 0.1^o. Therefore, for the analysis, the 4^o angular range acceptance of the Oxford detector due to using the $4^o \times 1^o$ mask was divided into 16 and 8 bins at small and large angles, respectively. This provided a 1^o-2^o self-consistent overlap by 4-8 matching bins as illustrated in Fig. 26. Hence in the final results, many data points represent the average of several measurements.

2. The Woods-Saxon OMPs

The data are characterized by rapid oscillation in the angular distribution measurements up to $\theta = 63^o$. These data have been fitted using the code OPTIMINIX [81] in a standard optical model analysis with conventional Woods-Saxon volume form factors as introduced in Eq. (2.33). The number of the data points involved in this procedure is around $N = 110$, so the quality of the fit is judged with the reduced χ^2 criterion (normalized to $N - f$, where f is the number of free parameters)

$$\chi^2 = \frac{1}{N-f} \sum_i \frac{\left(\sigma_{\exp}\left(\theta_i\right) - \sigma_{th}\left(\theta_i\right)\right)^2}{\left(\Delta\sigma_{\exp}\left(\theta_i\right)\right)^2}. \tag{4.3}$$

The contribution of the Coulomb potential generated by a uniform charge distribution is fixed with a reduced radius $r_c = 1$ fm. The absence of any spin-dependent observables led us to ignore a spin-orbit term in the potential. The calculations showed that comparable results came from fitting the data with the volume or surface-localized terms has no preference, while including both of them complicated the fitting process with too many parameters. Therefore, only the volume absorption is considered. In addition, coupling of the ground state to excited states in either one of the colliding nuclei for the entrance channel ^{12}C+^{13}C was not observed in the data, so it has been neglected.

Due to the finite angular resolution and binning used in the analysis (0.25^o and 0.5^o bins), the calculations show sharper minima with large depths in the angular distribution than the data. A correction for the predicted cross section values was considered to smear the calculations and make them comparable with the experimental results. A ROOT macro code was run to convolute the calculated cross section curves with the

TABLE III. The best fit parameters of the Woods-Saxon optical model potential obtained from the analysis of the elastic scattering data for ^{12}C+^{13}C. The Coulomb-reduced radius is fixed to $r_c = 1$ fm. R_V and R_W are the rms radii of the real and imaginary potentials, respectively.

Pot	V [MeV]	W [MeV]	r_V [fm]	r_W [fm]	a_V [fm]	a_W [fm]	χ^2	σ_R [mb]	J_V [MeV fm^3]	R_V [fm]	J_W [MeV fm^3]	R_W [fm]
1	88.5	37.5	0.88	1.12	0.85	0.56	6.2	1445	229	4.47	157	4.53
2	146.5	18.3	0.74	1.21	0.89	0.57	2.5	1449	269	4.26	94	4.83
3	230.7	18.9	0.65	1.19	0.89	0.60	7.8	1464	318	4.05	95	4.82

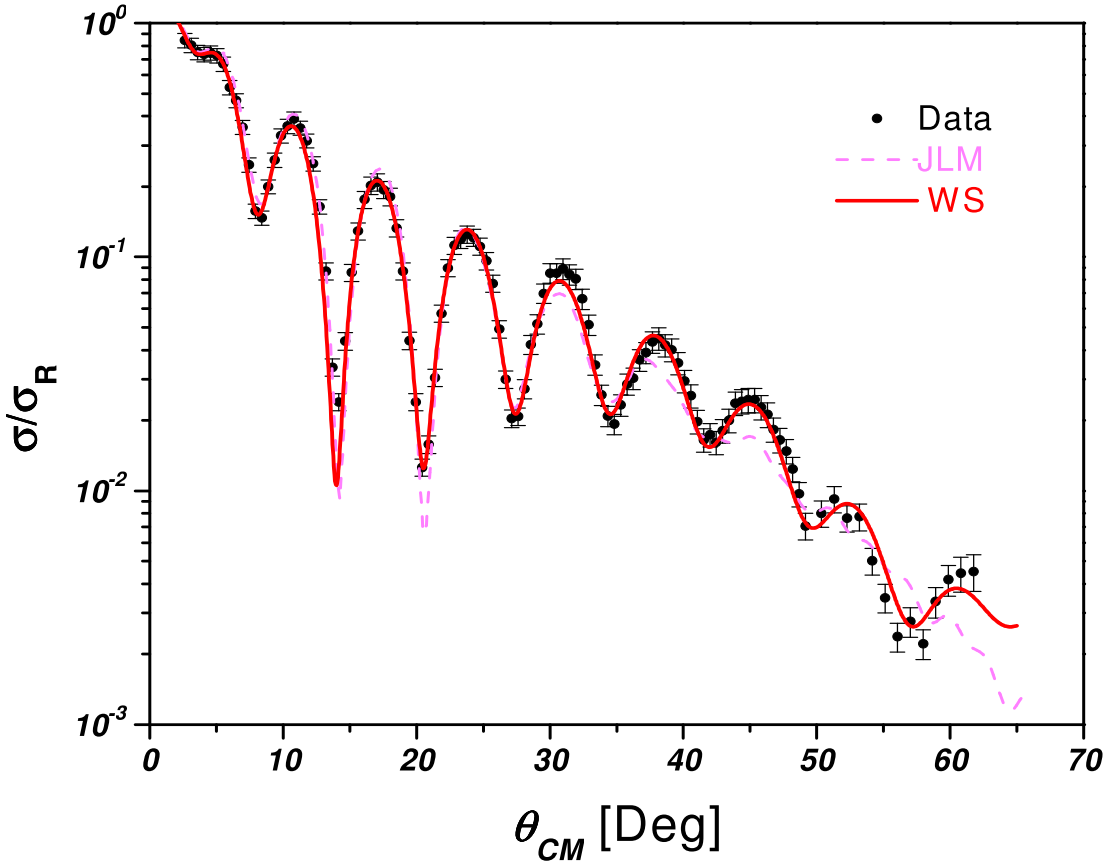

FIG. 28. The fits of the elastic scattering cross section of 127.2 MeV ^{12}C on ^{13}C in the forward hemisphere. The solid and dashed curves are the calculations for the optical potentials that have the smallest χ^2 presented in Table III and Table IV for Woods-Saxon and double folding forms, respectively.

experimental angular resolutions and binnings relative to each spectrometer angle.

The extracted OMPs from the fits are presented in Table III, where the six adjustable parameters of the nuclear real and imaginary volume parts of the optical potential were sufficient to reproduce the elastic scattering in the whole angular range. In this process, the local minima in the reduced χ^2 obtained by varying V in steps were first identified, then a complete search on all six parameters was run to determine the best fit. All the sets of parameters shown in Table III give an excellent description of the data. This reflects the well known ambiguities in the determination of OMP parameters. The cross section described by the second parameter set in Table III, which has the smallest χ^2, is plotted in Fig. 28. The elastic scattering cross section was re-calculated using the PTOLEMY [82] to check for consistency between different codes.

In comparison with the nuclear real parts, the optical potentials in Table III have a consistent preference of weak imaginary volume parts with the same values of W for the second and third potentials, while the first potential is almost a factor of two larger. The other parameters are slightly changed with systematic ratios, where $r_V < r_W$ and the diffuseness parameters $a_V > a_W$. The root mean square radius of the real and imaginary potentials are respectively given by

$$\left\langle R_V^2 \right\rangle = \int_0^\infty V(r) r^4 dr \Big/ \int_0^\infty V(r) r^2 dr \tag{4.4}$$

$$\left\langle R_W^2 \right\rangle = \int_0^\infty W(r) r^4 dr \Big/ \int_0^\infty W(r) r^2 dr. \tag{4.5}$$

The volume integral per interacting nucleon pair of the real and imaginary part is

$$J = J_V + iJ_W = -\left(1/A_P A_T\right) 4\pi \int_0^\infty \left(V\left(r\right) + iW\left(r\right)\right) r^2 dr, \tag{4.6}$$

where the $V(r)$ and $W(r)$ formulas are given in Eq. (2.35), and $A_{P(T)}$ is the mass number of the projectile (target) nucleus. The values J_V are used to check the ambiguity of the OMPs. A grid search procedure of the real depth of the potential for V = 50-270 MeV found discrete minima of χ^2, as shown in Fig. 29, which are associated with jumps of $\Delta J_V \simeq$ 50-70 MeV fm^3 from one family to the next with almost constant imaginary volume integrals. These OMP families identify the discrete ambiguities. The root mean square (rms) radii for each family were required to fit both forward- and intermediate-angle cross sections. Applying the same grid search on the other Woods-Saxon parameters led to a continuous ambiguity, where $J_V R_V \approx$ constant. The absorption seems to be independent of the strength and shape of the real part of the potential, resulting in a constant total reaction cross section with an average value of 1453 mb.

Inelastic scattering of the ^{12}C beam to the first excited state of the ^{13}C target, J$^\pi = \frac{1}{2}^+$ with an excitation energy 3.09 MeV, was also observed in the raw data. The same Woods-Saxon potential was used to calculate the inelastic angular distribution and is shown in Fig. 30 to reproduce the data. The fit was made using the the same reference potential as in the elastic scattering cross section figure, convoluted with the experimental angular resolution, and normalized to account for the deformation of the target nucleus. The poor match for the minima of the data in comparison with the fit is due to low statistics and background in the Oxford detector that may prevent producing a better angular distribution.

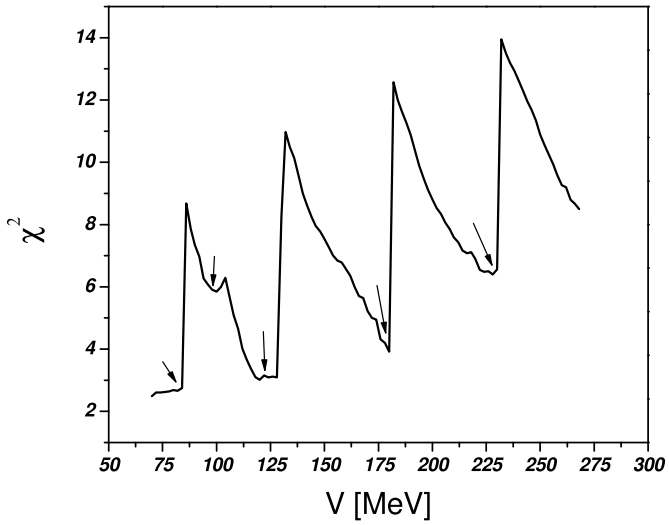

FIG. 29. A grid search was performed to obtain preliminary OMPs by varying the real depth of the optical potential and adjusting the other optical parameters. The minima with small χ^2 show the discrete ambiguities of the potential. The arrows indicate the potentials that were used as initial conditions for further fitting process to find the best description of the elastic scattering data.

3. The Double Folding Potential OMPs

The elastic scattering data have been also analyzed using double folding potentials. The wave functions and the densities for ^{12}C and ^{13}C nuclei were obtained in a standard spherical Hartree-Fock procedure as discussed in Chapter II and Ref [46]. The main constraint for the calculation was to slightly adjust the parameters of the surface term in order to reproduce the experimental total binding energy. Then, the optical potentials were obtained from the calculated nuclear mass densities folded with the effective JLM(1) interaction to provide simultaneously both the real and imaginary parts. The fitting procedure started with the standard range parameters $t_V = 1.2$ fm and $t_W = 1.75$ fm, and the average renormalization parameters $N_V = 0.37$ and $N_W = 1.0$ of Ref [46]. Then those parameters were adjusted using Eq. (2.41) until

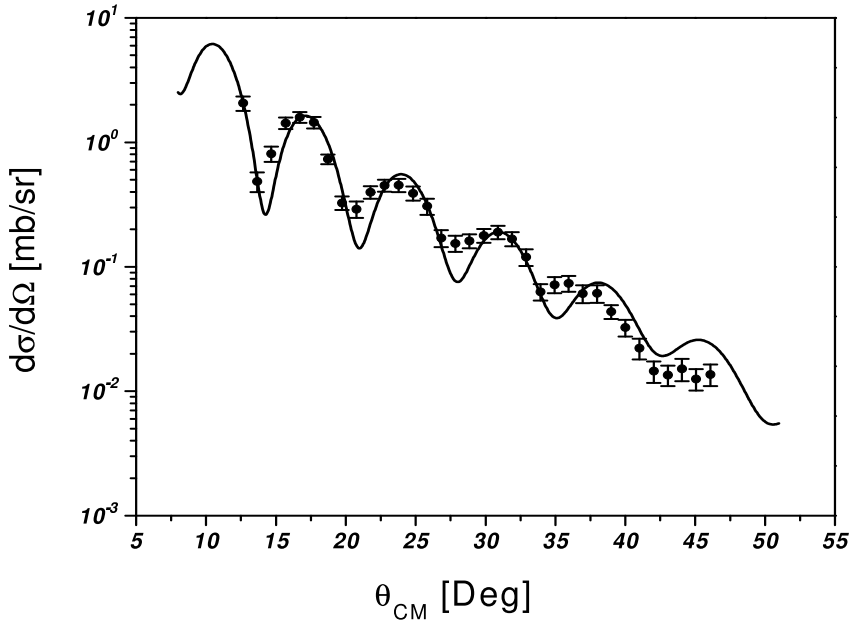

FIG. 30. The Woods-Saxon fit of the inelastic scattering of ^{12}C particles from the first $\frac{1}{2}^+$ excited state in the ^{13}C target.

the best description of the elastic scattering data was reached. The OMP families with the smeared range parameters t_V and t_W and renormalized strength parameters N_V and N_W, which have the smallest χ^2, are presented in Table IV, and the fit of the data with the second parameter set is shown in Fig. 28.

From the study of many elastic scattering reactions that involve break-up in loosely bound nuclei at energies around 10 MeV/A, Ref. [46] found the average and standard deviation for N_V is 0.37 ± 0.03. This renormalization is due to the dynamic polarization contribution to the optical potential, which arises from the effects of coupling to nonelastic channels [83]. This polarization correction is not included in the folding-model potential. In contrast, the imaginary part of the optical potential does not need any renormalization, $N_W = 0.99 \pm 0.06$. This indicates that the imaginary part

TABLE IV. The best fit optical model parameters for the folding potential with various effective interactions, χ^2, the total nuclear cross section reaction, and the rms radii of the real and imaginary parts and their corresponding volume integrals per pair of interacting nucleons.

Pot	N_V	N_W	t_V [fm]	t_W [fm]	χ^2	σ_R [mb]	J_V [MeV fm^3]	R_V [fm]	J_W [MeV fm^3]	R_W [fm]
1	0.35	0.93	1.64	1.44	4.8	1458	200	4.31	115	4.40
2	0.37	1.08	1.61	1.21	4.5	1442	208	4.29	134	4.29
3	0.42	0.97	1.20	1.75	13.3	1520	236	4.08	119	4.56

of the effective interaction and its density dependence are well calculated in the double folding potential. It is clear from Table IV that all the potentials, which give the most realistic description of the scattering data, have similar volume integrals for the real part $J_V \approx 215$ MeV fm^3, which are equivalent to the phenomenological potentials that have small real well depths with an average value around $V \approx 115$ MeV. Similar to the Woods-Saxon ones, the imaginary potentials are independent of the real parts, predicting a total nuclear reaction cross section 1473 mb, which is very comparable with the average WS value. Because the calculations were carried out with the use of spherical Hartree-Fock density distributions, no deformation in the ^{13}C nucleus is included.

4. The Strong Absorptive Optical Potential

To understand the behavior of the elastic scattering angular distribution in Fig. 28, the nuclear part of the scattering amplitude can be decomposed into

$$f(\theta) = f^{+}(\theta) + f^{-}(\theta), \tag{4.7}$$

where $f^{-}(\theta)$ refers to the near-side amplitude, while $f^{+}(\theta)$ is called the far-side amplitude. They are related to each other by

$$f^{-}(\theta) = f^{+}(-\theta). \tag{4.8}$$

The plus (or minus) sign represents the contribution of the subamplitude at θ from positive (or negative) angles relative to θ. These far/near trajectories are complex. The dominating imaginary part in ^{12}C+^{13}C collision characterizes the reaction by the presence of strong absorption, which develops rapidly at the surface of the two nuclei. This is usually manifested by a decomposition between the far/near-side trajectories, as shown in Fig. 31. Since they diffract from opposite sides of the target nucleus, their interference gives rise to a Fraunhofer diffraction that explains the strong oscillations in the elastic scattering cross section at small- and intermediate-angles. At very forward angles, the near-side and the Coulomb amplitudes rule the scattering, and can be described by Fresnel diffraction. In the region where the f^{+}/f^{-} amplitudes are comparable, the Fraunhofer diffraction type begins to develop, which gives evidence of the strong absorption. Both amplitudes are equal at $\theta = 16^{o}$. Beyond this angle, the angular distribution is completely damped by the strong absorption.

However, the features of the nuclear potential can not be easily investigated with the elastic scattering in the presence of strong absorption, which hides most of the particles that enter its domain, while the strong repulsive Coulomb potential will affect the particles further outside. Hence, only a small fraction of the scattered particle flux provides some details about the nuclear potential. One valuable peace of information is the radial sensitivity of the selected optical potential, which maps the effective region of the elastic scattering. Studying this property in ^{12}C+^{13}C elastic scattering is shown in Fig. 32. The real OMP obtained by the Woods-Saxon form,

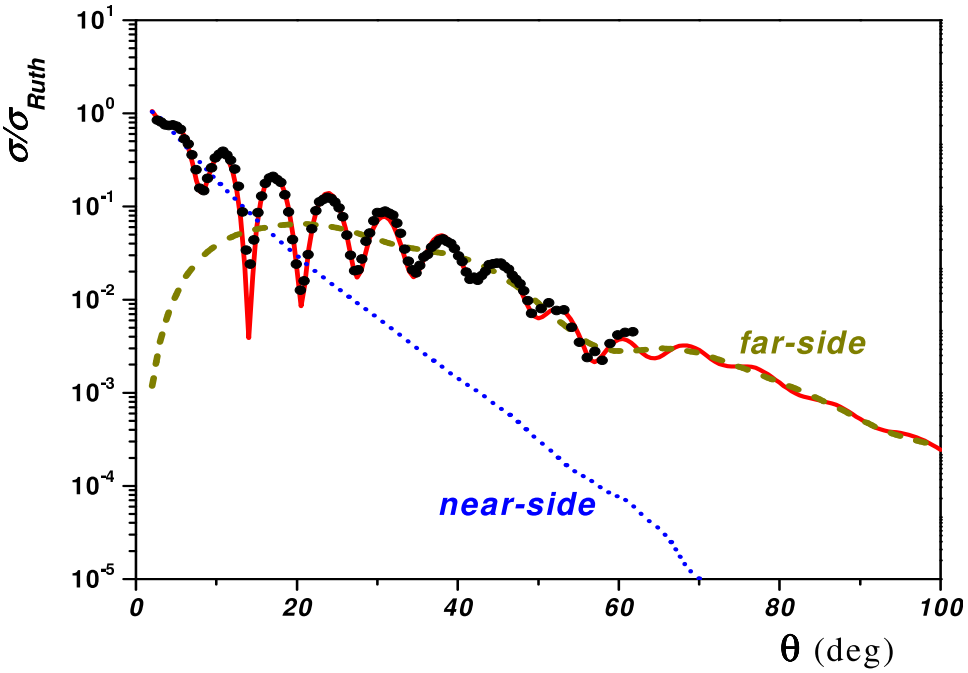

FIG. 31. Woods-Saxon optical model analysis of the elastic scattering for ^{12}C+^{13}C at 127.2 MeV. The far-side, near-side, and their coherent sum cross sections are shown by dashed, dotted, and solid lines, respectively. The curves are fits with the second potential presented in Table III.

the parameters of the second potential in Table III, were perturbed systematically through the potential by the factor [84]

$$g\left(R,a,d,r\right)=\left\{1-4df\left(R,a,r\right)\left[1-f\left(R,a,r\right)\right]\right\}. \tag{4.9}$$

Thus the Woods-Saxon form becomes

$$V\left(r\right)=Vf\left(R,a,r\right)g\left(R',a',d,r\right). \tag{4.10}$$

The employed perturbation cut out a notch in the potential at position r' with a width a' centered at R', reduced it by a factor d in some localized region, and then returned it to its original value. Using χ^2 to determine the effect of varying the potential, the

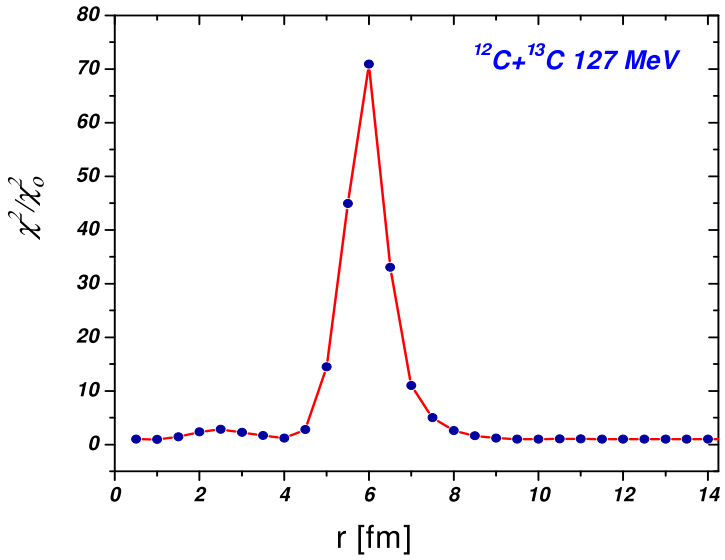

FIG. 32. A Gaussian perturbation on the real potential at a given radius. It shows that there is a relatively high sensitivity for radial distances at 5-7 fm, inside the strong absorption radius. χ^2_o was determined with the real OMP of the second potential in Table III, while χ^2 was calculated after the perturbation of the potential.

calculations in Fig. 32 show that sensitivity to the perturbation is peaked at radii 5-7 fm, which is inside the strong absorption radius. This means that the scattering is highly sensitive to the surface region and the radius of the interaction can be well determined.

An alternative way to test the radial sensitivity of the optical potential is described in Fig. 33. Plotting the real part of the Woods-Saxon forms that fit the data we observe that the potentials are practically identical at radii beyond 5 fm, because the colliding nuclei experience strong nuclear absorption at a grazing radius larger than the radius of the real potential, R_V. A similar comparison shows that the imaginary parts of the optical potentials in Table III match beyond 6 fm.

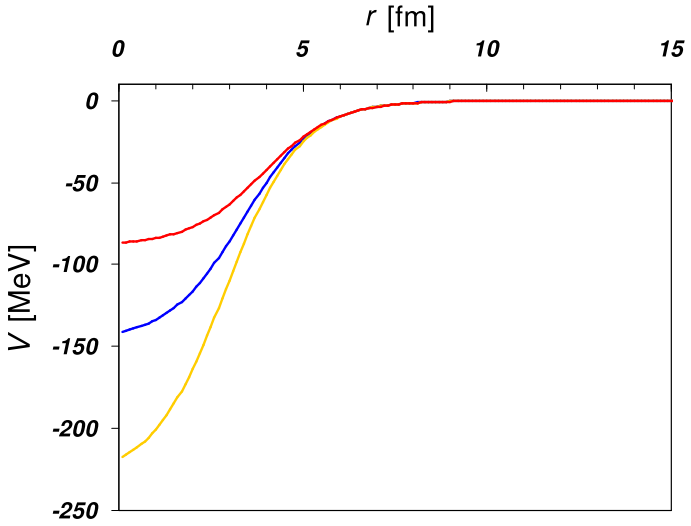

FIG. 33. The real potentials of Table III overlap at $r > 5$ fm.

5. The Semiclassical WKB Approximation

The far/near-side interference method does not give any information about the response of the nuclear interior, but it decomposes the scattering amplitude into traveling waves. To understand the reaction mechanism of ^{12}C+^{13}C elastic scattering and the dynamical contribution of the nuclear interior when the incident flux penetrates the Coulomb barrier, the semiclassical uniform approximation for the scattering amplitude of Brink and Takigawa [85] is well adapted. It illustrates the situation when the incident energy is sufficiently above, as in our case study, or below the Coulomb barrier, so the WKB approximation can be used. Following the analysis as in Ref. [45], discarding the absorption term, the effective real potential in the WKB approximation, which is defined by nuclear and centrifugal potentials as

$$V_{eff} = V(r) + \frac{\hbar^2 \lambda^2}{2\mu r^2}, \quad \lambda = \ell + \frac{1}{2} \tag{4.11}$$

has three classical turning points: r_1, r_2, and r_3, which are the roots of $E_{C.M.} - V_{eff} = 0$. Those points separate the external region from the internal region where

the attractive nuclear potential dominates. When the imaginary potential, $W(r)$, is included, the WKB approximation is continued into the complex plane [86], where r_1, r_2, and r_3 become isolated and complex, the roots of $E_{C.M.} - V_{eff} - iW = 0$. In this case r_2 moves into the upper half of the complex $\Im r$-plane, while r_1 and r_3 are in the lower half of the complex plane [85].

In this technique, the S-matrix of the semiclassical scattering is written as

$$\mathrm{S_{WKB}}(\ell) = \mathrm{S_B}(\ell) + \mathrm{S_I}(\ell), \tag{4.12}$$

where $\mathrm{S_B}(\ell)$ is the barrier term which identifies the flux reflected from the outermost point($r = r_1$), and $\mathrm{S_I}(\ell)$ is the internal barrier component that describes the flux reflected at the innermost turning point ($r = r_3$) and refracted several times between r_2 and r_3. The trajectories of the turning points are clarified in Fig. 34 for the ^{12}C+^{13}C reaction at $E_{C.M.} = 66$ MeV using potential 2 in Table III. For integer angular momenta, only turning points close to the real axis, $\Re r$, are retained and a typical case with three well isolated turning points is observed for each partial wave, as the effective potential is sufficiently high to sustain the potential barrier up to a grazing angular momentum, ℓ_g. Removing the imaginary part of the potential, the points $r_{1,2}$ become complex conjugates, while r_3 is purely real.

The accuracy of the WKB approximation was checked by comparing the barrier and internal barrier absorption profiles with the exact quantum-mechanical result, as shown in Fig. 35. Both the barrier/internal-barrier decomposition and quantum solution have the same results. The internal barrier profile has significant values up to $\ell_g = 25$ and is negligible beyond this value. The barrier component resembles a strong absorption profile and this confirms that part of the incident flux did not penetrate

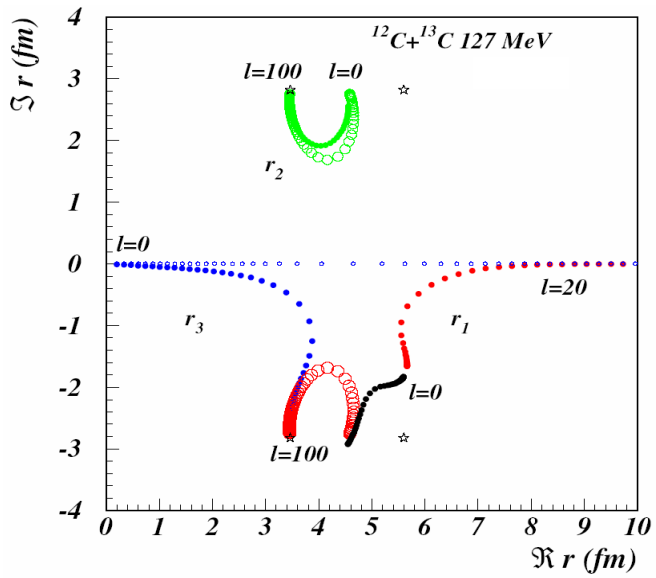

FIG. 34. Trajectories of the complex turning points (solid symbols) r_1, r_2, and r_3 for the potential 2 shown in Table III at integer angular momenta. Open symbols denote turning points for the real potential and stars indicate complex poles of the potential.

into the nuclear interior. The average value for $\ell \leq \ell_g$ is $|\mathrm{S}(\ell)| \approx 10^{-2}$. It is clear from the figure that the barrier and internal barrier components are almost decoupled in the angular momentum space and therefore they will contribute in different angular ranges.

Corresponding to the semiclassical scattering function of Eq. (4.12), the scattering amplitude is decomposed as $f_{WKB} = f_B + f_I$. then the barrier and internal barrier angular distributions are calculated as $\sigma_{B,I} = |f_{B,I}|^2$. The semiclassical cross sections are compared with the data in Fig. 36. Both the f_B and f_I are decomposed in their corresponding F/N side subamplitudes. Clearly, the forward angles are dominated by the barrier component, and the Fraunhofer diffraction occurs due to the interference of its F/N sides. The internal barrier component starts to dominate the angular

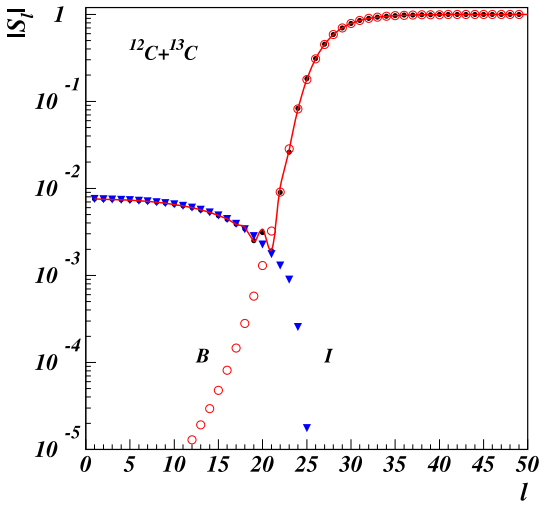

FIG. 35. Semiclassical decomposition of the scattering function for the Woods-Saxon potential of Fig. 34. Barrier (open circles) and internal barrier (triangles) are shown. The exact S matrix is indicated by small dots. The line is a cubic spline interpolation of the total semiclassical scattering function for the same potential.

distribution at angles greater than 80^o, but it is negligible before that. Therefore almost no trace of the refractive effects survive in the measured cross section, and the scattering is completely absorptive.

6. The ^{13}C(^{12}C,^{13}C)^{12}C Exchange Reaction

The experiment used to extract the angular distribution for the neutron transfer in the ^{13}C(^{12}C,^{13}C)^{12}C reaction in Fig. 37 is similar to the elastic scattering procedure described above. The measurements were carried out for spectrometer angles 3^o-18^o, which covers 3^o-37^o of the angular distribution in the C.M. frame. The fields in the spectrometer were set at each angle to measure ^{13}C. In Fig. 37, the elastic transition of a neutron from the ground state of the target, $J^\pi = \frac{1}{2}^-$, to the ground state of the ejectile, $J^\pi = \frac{1}{2}^-$, was observed and gated for further analysis. The

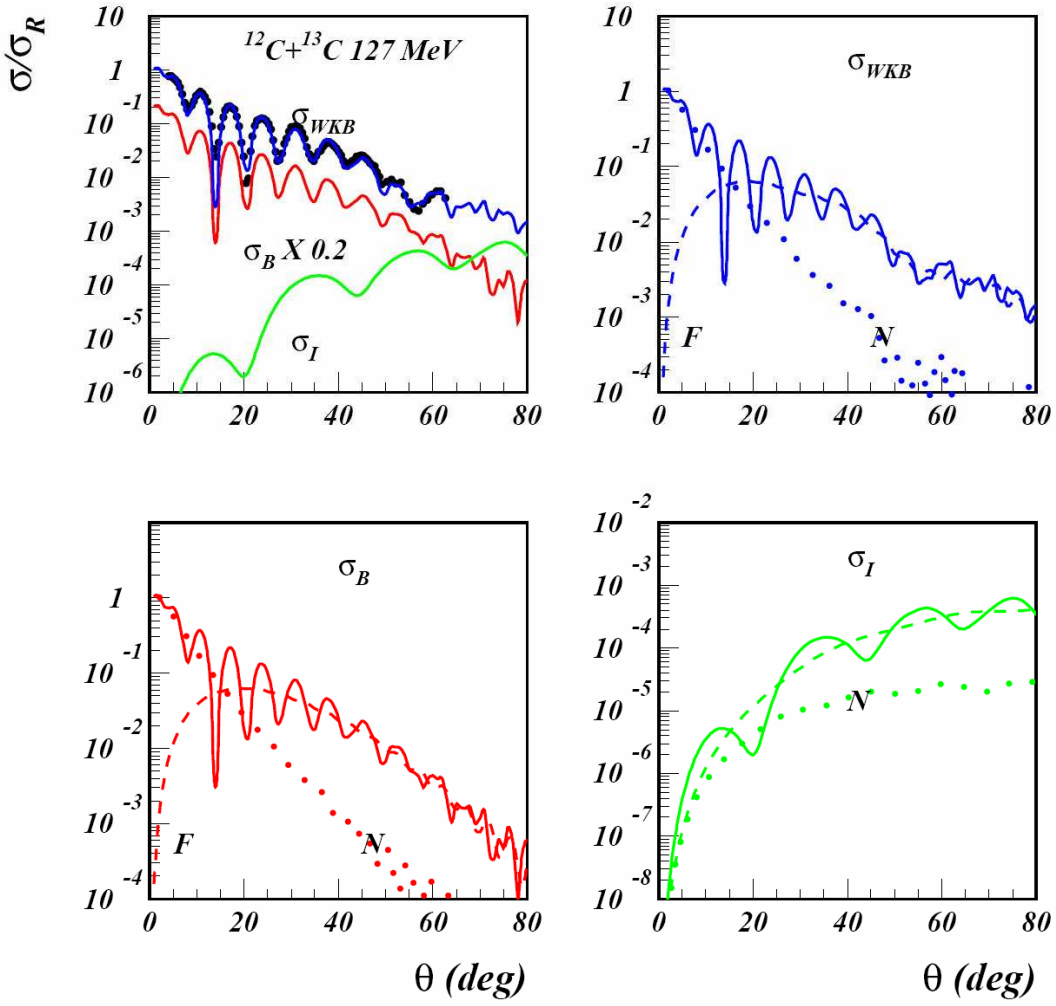

FIG. 36. Semiclassical barrier and internal barrier decomposition of the cross section. Each component is decomposed into far-side (dashed), near-side (dotted) components, and their coherent sum (solid).

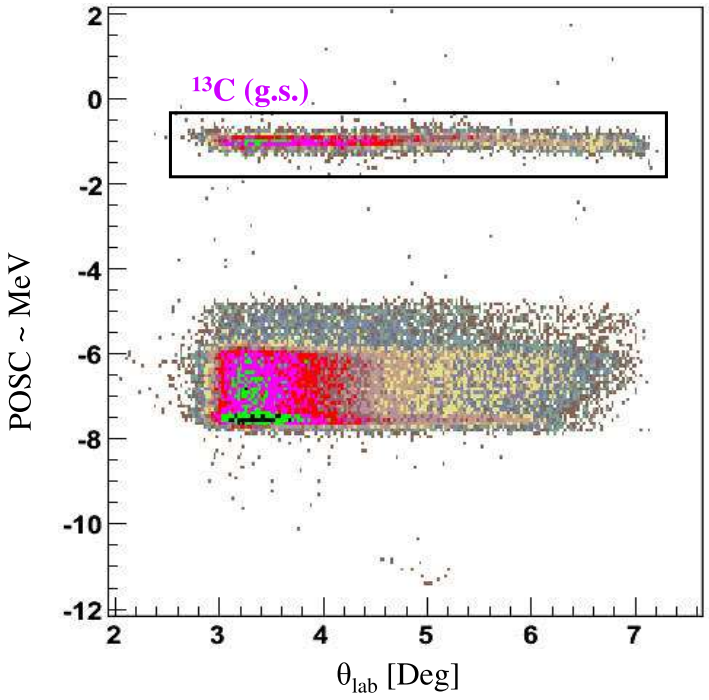

FIG. 37. The (Angle,POSC) histogram shows the raw data of the ^{13}C(^{12}C,^{13}C)^{12}C reaction. The gated band selects the elastic transfer reaction to the $J^{\pi} = \frac{1}{2}^{-}$ in ^{13}C. Other inelastic transfer reactions are difficult to extract because of their low statistics and the limited energy resolution at higher excitation energies.

expected angular distribution was calculated with the PTOLEMY and FRESCO [87] DWBA codes. These calculations have been done using the same optical potential that describes the elastic scattering in the entrance and exit channels, because the initial and final nuclei are identical. Both DWBA codes give the same expected elastic transfer angular distribution. The comparison between the data and the calculation is plotted in Fig. 38 for a specific geometry of the Woods-Saxon neutron-binding potential, $r = 1.25$ fm and $a = 0.65$ fm. The DWBA calculation was normalized to the data by a spectroscopic factor $S = 0.65$. The agreement is excellent at forward angles.

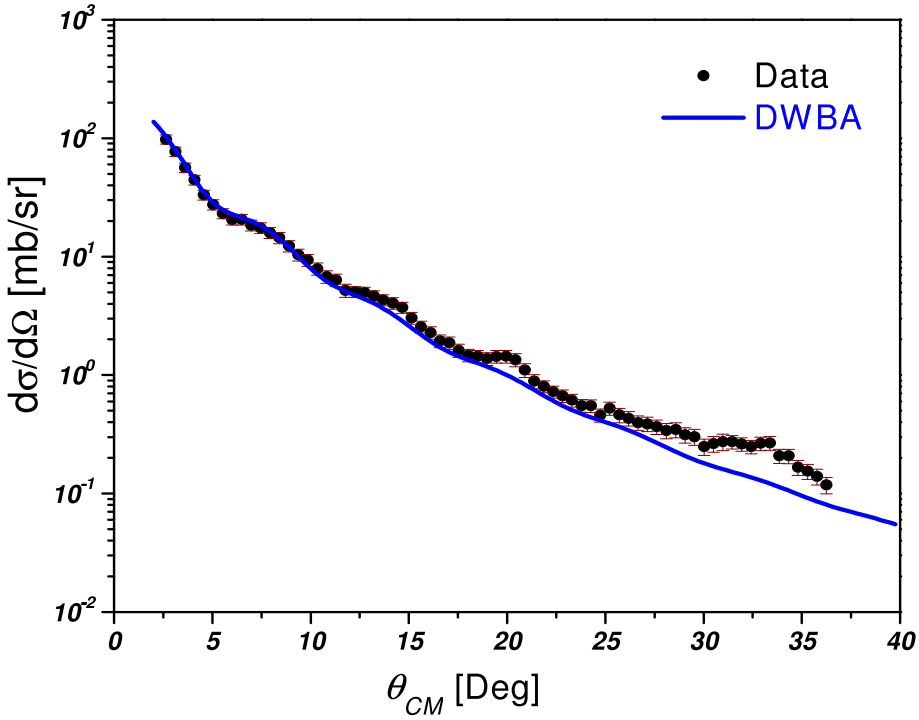

FIG. 38. The experimental and the calculated angular distribution of the ^{13}C(^{12}C,^{13}C)^{12}C transfer reaction. The points are the experimental data, while the solid line is the DWBA cross section obtained from PTOLEMY. The calculation has been done with the second optical potential in Table III.

Even though the spectroscopic factor is strongly dependent on the choice of the optical model parameters, existing measurements of the angular distribution of $p_{1/2}$ to $p_{1/2}$ transitions of ^{12}C$(d,p)^{13}$C and ^{13}C$(p,d)^{12}$C neutron-transfer reactions have been performed at several incident energies. Most recent experiments gave an average value, S is 0.61 ± 0.09 [61], for incident deuteron energies from 12 to 60 MeV. This agrees with the measured value above, but only for the same DWBA input parameters. Therefore it gives a good indication about the reliability of the DWBA calculations.

Excitation of the 4.44 MeV 2^+ state in ^{12}C or of the 3.09 MeV $\frac{1}{2}^+$ state in ^{13}C may contribute to the population of the ground state of ^{13}C in the neutron transfer reaction.

Coupled-channel calculations are needed to detect the consequences of the inelastic couplings on the elastic transfer reaction. A study of ^{12}C$(d,p)^{13}$C and ^{13}C$(p,d)^{12}$C reactions beyond the Born approximation for energies between 7 and 60 MeV was reported in Ref. [88]. It was found that the coupling to the 2^+ state changes the amplitude of the cross section up to 15%, but its effect at higher deuteron energies, more than 30 MeV, is almost negligible. The coupling to the $\frac{1}{2}^+$ state in ^{13}C has a almost 5% effect on the transfer cross sections at relatively small deuteron energies, $E_d \leq 30$ MeV, and is also negligible at higher energies. Hence, the coupled reaction channel effects have been neglected in the present calculations of the ^{13}C(^{12}C,^{13}C)^{12}C exchange reaction.

Measuring the elastic neutron exchange reaction of ^{13}C nuclei at forward angles is kinematically equivalent to measuring elastically scattered ^{12}C particles at backward angles in the C.M. frame. The C.M. energy is conserved and the final states of these two processes are indistinguishable. Therefore their amplitudes may interfere. The angular distribution for the elastic scattering of ^{12}C on ^{13}C using the data from the detection of ^{12}C in the forward hemisphere and the data from the detection of ^{13}C at complementary forward angles in the backward hemisphere are plotted in Fig. 39. The rise in the cross section at backward angles proves a contributing mechanism that is different from the potential elastic scattering, so it can be explained solely by the transfer of a neutron from the target to the projectile. Hence, the two mechanisms dominate in completely different angular regions with negligible interference within the measured regions, and we can treat them separately and neglect any interference between the elastic and exchange amplitudes.

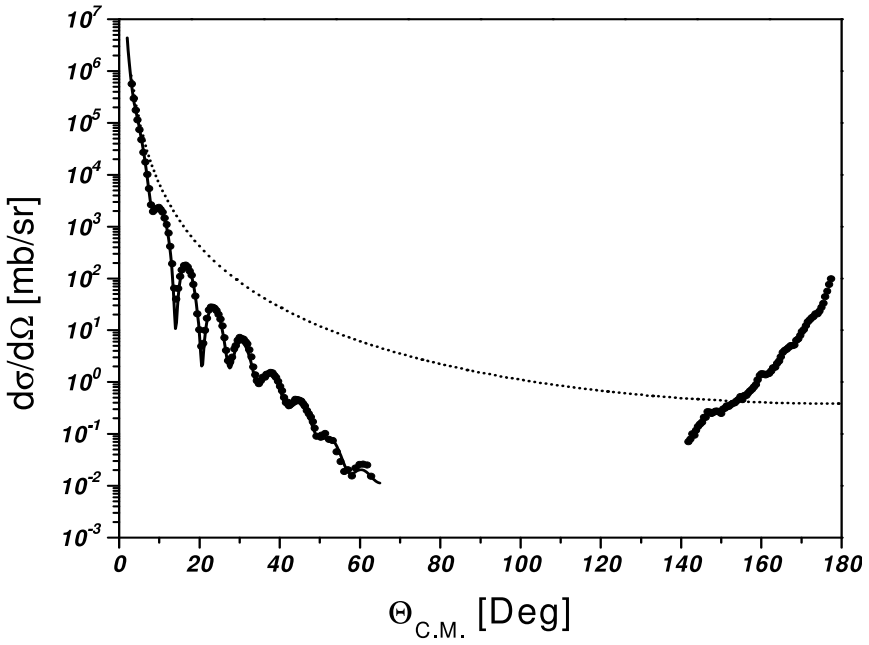

FIG. 39. The whole angular range $\theta_{C.M.} = 0^o$-180^o of the elastic scattering cross section. The data at forward angles indicate the elastically scattered ^{12}C particles. Those at backward angles were obtained by measuring the recoiling ^{13}C nuclei at complementary forward angles. The dotted line is the Rutherford scattering cross section.

7. Extracting the ANC in ^{13}C

Since the entrance and exit channels of the reaction are identical, the same spectroscopic factors and ANCs occur at both vertices of Eq. (2.51), which then becomes

$$\frac{d\sigma}{d\Omega} = C^4_{p_{1/2}} \left(^{13}C\right) \frac{\sigma^{DWBA}}{b^4_{p_{1/2}}}, \tag{4.13}$$

where the neutron is transferred from the $p_{1/2}$ state in the ^{13}C target to the $p_{1/2}$ state in the ^{13}C ejectile. The value of the single particle ANC $b_{p_{1/2}}$ is defined as in Eq. (2.48). Since the Sommerfeld parameter is zero for a neutron, the Whittaker function is replaced by the corresponding Hankel function. The radial behavior of the single particle bound state neutron wave function $r\phi(r)$ in ^{13}C(g.s.) $\rightarrow$ ^{12}C + n

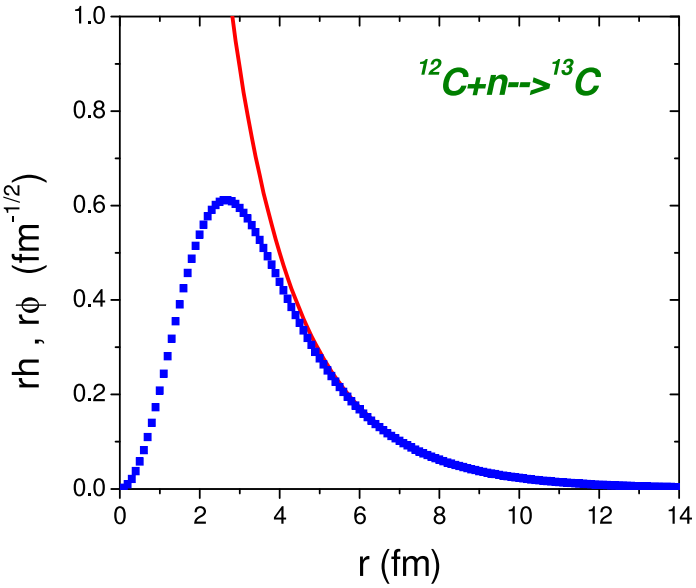

FIG. 40. The radial behavior of the single particle radial bound state wave function $r\phi(r)$ in ^{13}C, blue squares, calculated in the Woods-Saxon potential with $a = 0.6$ fm and $r_o = 1.2$ fm. The solid line is the tail of $rh^{(1)}_{\ell=1}(i\kappa r)$ normalized to the bound state wave function. The ratio between the two functions for $r \gg R$ gives the single particle ANC $b = 1.72$ fm.

is illustrated in Fig. 40. In comparison with the Hankel function, the radial wave function reaches it asymptotic shape for $r > 4.5$ fm. Therefore in calculating the DWBA matrix element, the bound state can be replaced by its asymptotic term.

If the reaction is peripheral, then the value of the ANC extracted from experiment will be constant over a broad range of single particle well parameters, while the spectroscopic factor S is strongly dependent on these parameters. The comparison between $S_{p_{1/2}}$ and $C^2_{p_{1/2}}$ extracted for single particle potentials with parameters ranging from $r_o = 1.1$-1.3 fm and $a = 0.5$-0.65 fm, as a function of the value of the corresponding single particle ANC $b^2_{p_{1/2}}$ is shown in Fig. 41. For each new geometry the depth of the single particle potential was adjusted to fit the experimental neutron binding energy.

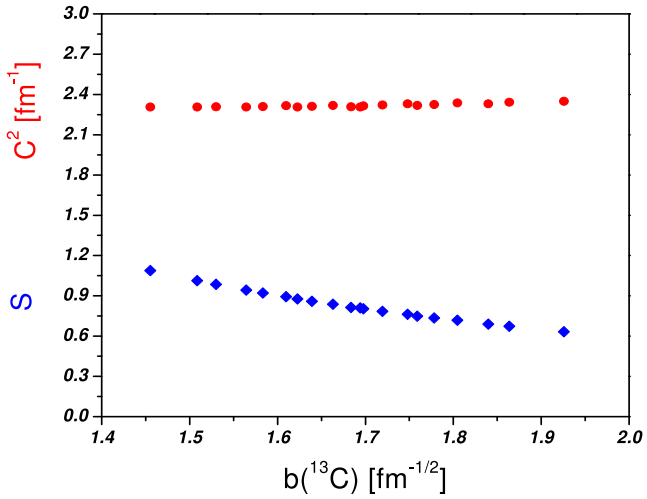

FIG. 41. Comparison of the spectroscopic factors (blue diamonds) and of the ANC C^2 (red dots) extracted from the exchange reaction for different geometries of the Woods-Saxon well.

It is obvious from the figure that the spectroscopic factor changes by almost $\pm 30\%$ about the mean value, while the ANC varies by less than $\pm 2\%$ over the full range. This is completely understood if the transfer is peripheral and therefore the calculated cross section σ^{DWBA} is to good approximation proportional to $(b^2)^2$, leading to a ratio of σ^{DWBA}/b^4 which is nearly independent of the individual values of r_o and a. Reversing the reasoning, if this constancy of C^2 is observed, it means that only the asymptotic part of the wave function contributes in the DWBA calculation and the transfer reaction is peripheral. Moreover, the elastic scattering analyses indicate the nuclear trajectories are restricted to r greater than ~ 5 fm. Figure 40 shows that $r\phi$ matches its Hankel function asymptotic form in this region. Another way to check for the peripherality of the reaction is to localize the transfer strength with partial waves. The DWBA transition matrix is peaked around $\ell = 29$, which corresponds to $r = 6.64$ fm using Eq. (3.1), and has a FWHM of about 10, making this reaction strongly focused on the surface.

By normalizing the calculated DWBA cross section to the measured one, the value of the ANC for the virtual decay ^{13}C(g.s.) $\rightarrow$ ^{12}C + n is extracted using Eq. (4.13). The most important angular region to obtain the ANC is at $\theta_{C.M.} < 18^o$, where no contributions from multi step processes are involved, or $cos\theta \sim 1$, and the pole mechanism, Fig. 11, is dominating. The uncertainties in the value of C^2 include the contribution of the average statistical errors (3%), the normalization of cross section with the Faraday cup (3%), the measurements of the target thickness (7.5%), the geometry of the neutron binding potential used in the DWBA calculations (1.5%), the fit between the measured and the calculated cross sections for several angular ranges (1.0%), and the normalization of the cross section with different optical potentials in Table III (1.5%). All these uncertainties are summed to give an overall 9% accuracy of C^4, so the uncertainty in determining C^2 is (4.5%) .

As a result from the present experiment the extracted ANC is $C^2_{p_{1/2}} = 2.24 \pm 0.11$ fm^{-1}. In Ref. [89] for the same exchange reaction, but at $E = 12$ MeV, it was reported that $C^2 = 2.39 \pm 0.09$ fm^{-1}. On the other hand, a value for the nuclear vertex constant $|G|^2$ from the analysis of the elastic scattering ^{12}C+^{13}C, ^{13}C$(p,d)^{12}$C(g.s.), ^{12}C$(d,p)^{13}$C(g.s), ^{13}C$(d,t)^{12}$C, ^{13}C(^{12}C, ^{13}C)^{12}C, and ^{12}C(^{13}C,^{12}C)^{13}C reactions has an average value of 0.39 ± 0.02 fm [90]. The vertex constant is related to the ANC by

$$G_{l,j} = -\pi \left(\frac{\hbar}{\mu c}\right) \exp\left[i\frac{1}{2}\pi\left(l+\eta\right)\right] C_{l,j}. \tag{4.14}$$

Using this equation, the calculated ANC in ^{13}C is taken to be $C^2_{p_{1/2}} = 2.40 \pm 0.12$ fm^{-1}. Since this value is in good agreement with the value obtained in this experiment within the uncertainties, a more precise value for the ANC is obtained by calculating the weighted average of all the measurements. Therefore, the new adopted value is $C^2_{p_{1/2}} = 2.31 \pm 0.08$ fm^{-1}.

C. The ^{13}C(^{22}Ne,^{23}Ne)^{12}C Experiment

The nuclear reaction ^{13}C(^{22}Ne,^{23}Ne)^{12}C was measured to determine the ANCs for the ground state and the first excited state in ^{23}Ne, then we transpose them to the ANCs of the corresponding states in its mirror nucleus ^{23}Al to determine the reaction rate of ^{22}Mg(p,γ)^{23}Al. This section will follow exactly the same procedure that was described for the ^{13}C(^{12}C,^{13}C)^{12}C experiment to extract the ANCs. The estimation of the astrophysical reaction rate will be presented in Chapter V.

1. Elastic Scattering of ^{22}Ne+^{13}C and ^{22}Ne+^{12}C

The elastic scattering was measured by bombarding separately ^{12}C and ^{13}C targets with a well collimated ^{22}Ne^{+4} beam at 12 MeV/A. The position calibration of the Oxford detector was performed online with a Au target, while the angle calibration was calculated offline with the RAYTRACE code and checked online with the 5-finger mask for any further adjustments. The elastic scattering of ^{22}Ne+^{13}C was measured to obtain the OMP for the entrance channel of the nuclear reaction. ^{22}Ne only differs from ^{23}Ne by one nucleon, so the scattering of ^{22}Ne+^{12}C was studied to get the optical potential for the exit channel.

The differential cross sections were measured for the angular range 3^o-55^o in the C.M. frame. The angular resolution of the detector in the laboratory frame was $\Delta\theta_{res} = 0.22^o$-$0.46^o$ at small to large angles, respectively. However, due to the almost 1% contaminations in the target, angles less than 5^o degrees were dropped from the angular distributions. Similar amounts of Ta and Si traces were found in both targets. The raw data and the online analysis of the elastic scattering of ^{22}Ne+^{13}C when the spectrometer was at 5^o are shown in Fig. 42. Three well separated states for

the scattered ^{22}Ne particles were identified in the (Angle,POSC) histogram with an energy resolution less than 300 keV. RAYTRACE was run to determine the position of the 0^+ (0 MeV), 2^+ (1.275 MeV), and 4^+ (3.358 MeV) states in ^{22}Ne along the dispersive x-axis in the focal plane of the Oxford detector. The calculations were compared with the measured positions. The energy calibration of E_{exc} in MeV versus the POSC in cm confirms the detection of the elastic and inelastic scatterings in these states of the ^{22}Ne particles. Gating and projecting the ground state band on the angle-axis gives the angular distribution of the elastic scattering within the $\pm 2^o$ range around the central MDM angle. The procedure illustrated in Fig. 42 was also applied for the ^{22}Ne+^{12}C measurement.

2. Optical Model Potentials

Optical potentials have been determined by a fit with phenomenological Woods-Saxon shapes. Only the central components have been included in the optical potential, since spin-orbit couplings and absorptive surface terms have little or no influence on the cross section. As noted above, the OPTIMINIX fitting code did not produce a good description of the elastic scattering for ^{22}Ne+^{13}C and ^{22}Ne+^{12}C at forward angles, where Rutherford scattering dominates, without reducing N_{FC} by almost 30%. Fits using PTOLEMY, FRESCO, and ECIS [91] gave the same results. The folding-model potentials using the JLM(1) effective interaction have been also calculated.

Several solutions were found from the analysis. The extracted optical potentials are listed in Table V. The first family of parameters, Pot. 1, listed in the table for the ^{22}Ne+^{13}C case was obtained by fitting the output results of the JLM with Woods-Saxon shapes. The JLM parameters were converted to their equivalent Woods-Saxon parameters and included in the table. The convoluted cross section using the po-

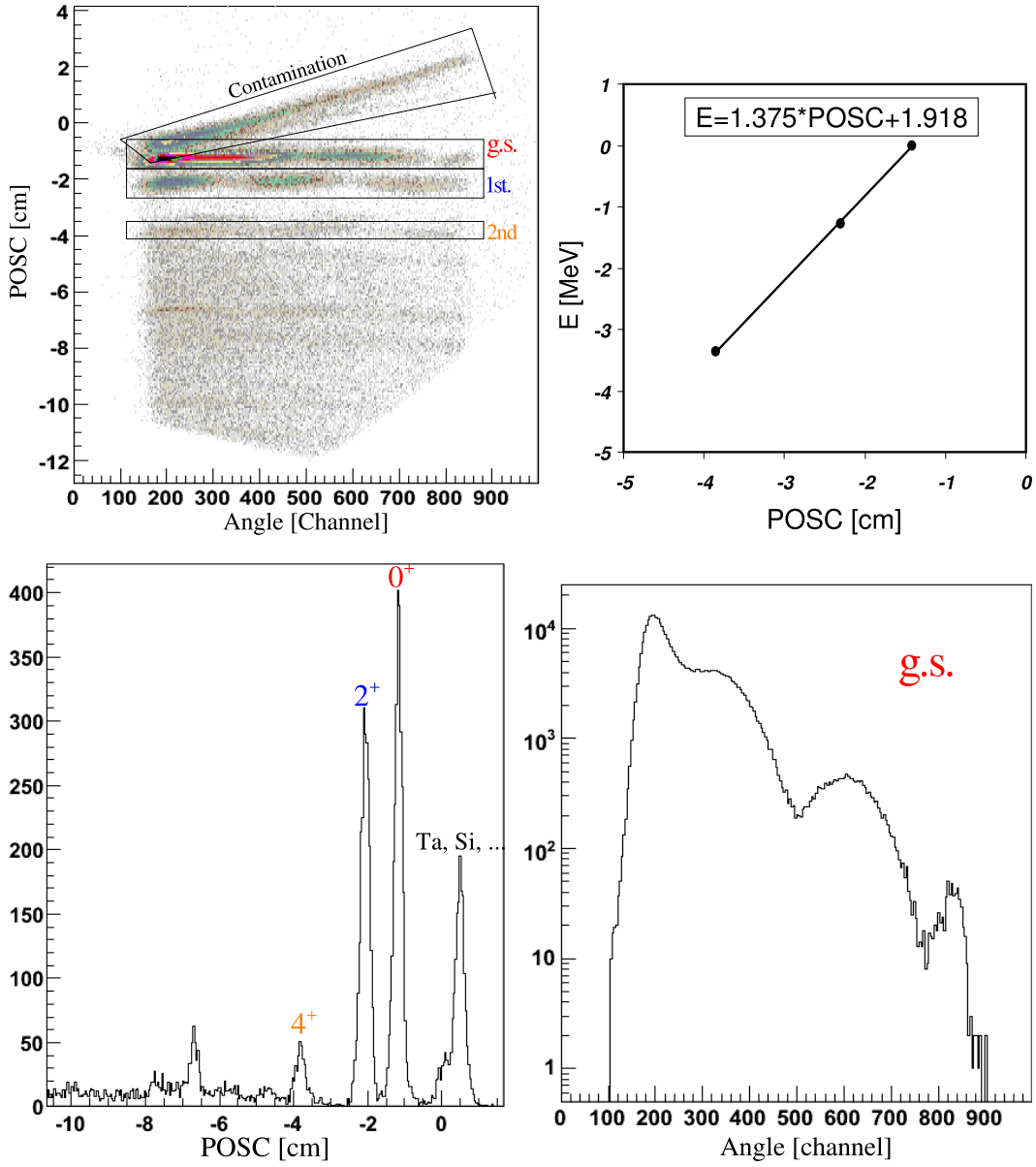

FIG. 42. The upper left figure shows the (Angle,POSC) histogram for the ^{22}Ne+^{13}C elastic scattering when the MDM was at 5^o. Three separated states were observed in the histogram in addition to the contaminations in the target. To identify the states, a calibration using RAYTRACE to obtain the excitation energy as a function of POSC [cm], left bottom figure, was determined as shown in the upper right figure. The ground and first excited states in ^{22}Ne were well populated and their cross section values were analyzed, as in bottom right figure.

tentials that have the best fit, or the smallest χ^2, for each of the entrance and exit channels are compared with the data in Fig. 43. The optical parameters obtained for the two reactions are very comparable and have similar values.

In addition to the measurements of the elastic scattering, inelastic scattering with the excitation of ^{22}Ne particles to the lowest 2^+ (1.275 MeV) and 4^+ (3.385 MeV) states were observed as shown in Fig. 42. The optical potential parameters from Table V were used to describe the outgoing ^{22}Ne$^*(2^+)+^{13}$C and ^{22}Ne$^*(2^+)+^{12}$C channels. It was found that the inelastic cross sections were proportional to the square of the Coulomb deformation parameter β, which is related to the reduced electric transition probability $B\left(E2\right)\uparrow$ by the formula

$$\beta = \frac{4\pi}{3ZR_o^2}\sqrt{\frac{B\left(E2\right)\uparrow}{e^2}}, \tag{4.15}$$

where $R_o^2 = R\left(A_p^{1/3} + A_t^{1/3}\right)$ and $B\left(E2\right)\uparrow$ is the reduced transition probability in units of $\mathrm{e^2b^2}$.

Comparison between the experimental and calculated cross sections estimated that $\beta = 0.560$. This value was obtained by adjusting the calculations to give the best fit of the data in Fig. 44. The PTOLEMY and ECIS codes gave similar results, where β was either inserted explicitly in the input file, or the central real/imaginary volumes and Coulomb potential were deformed in the outgoing channel by multiplying their values with β. It was shown that the experimentally adopted value for β is 0.562 ± 0.012 [92]. The inelastic cross section is at least one order of magnitude smaller than the elastic scattering cross section. Therefore the deformation of the ^{22}Ne nucleus only contributes weakly through coupled channels and the calculated elastic scattering cross section is unchanged.

TABLE V. The parameters of the Woods-Saxon optical model potential obtained from the analysis of the elastic scattering data for ^{22}Ne+^{13}C and ^{22}Ne+^{12}C, where $r_c = 1$ fm for all potentials. The Pot. 1 and 3 for ^{22}Ne+^{13}C and Pot. 1 and 4 for ^{22}Ne+^{12}C were obtained from JLM fits, then converted to their corresponding Woods-Saxon parameters.

Channel	Pot	V [MeV]	W [MeV]	r_V [fm]	r_W [fm]	a_V [fm]	a_W [fm]	χ^2	σ_R [mb]	J_V [MeV fm^3]	R_V [fm]	J_W [MeV fm^3]	R_W [fm]
^{22}Ne+^{13}C	1	81.01	14.14	0.88	1.33	0.85	0.66	5.7	1979	155	4.74	72	5.84
	2	93.06	14.32	0.84	1.32	0.90	0.67	8.7	1997	155	4.74	73	5.84
	3	167.13	15.37	0.74	1.31	0.88	0.64	6.3	1937	208	4.41	74	5.73
	4	245.05	15.30	0.66	1.31	0.90	0.63	6.8	1921	234	4.26	75	5.73
^{22}Ne+^{12}C	1	68.41	13.97	0.94	1.34	0.79	0.70	8.4	2018	152	4.73	78	5.90
	2	77.35	14.58	0.89	1.32	0.84	0.65	6.5	1914	154	4.70	77	5.75
	3	126.00	15.81	0.89	1.31	0.69	0.78	9.7	2095	230	4.35	83	5.92
	4	155.14	16.30	0.79	1.29	0.82	0.67	7.9	1907	223	4.34	81	5.67
	5	236.96	16.11	0.68	1.29	0.86	0.65	8.5	1874	252	4.18	80	5.64

3. Strong Absorption Profiles

Typical Fraunhofer oscillations are observed in the elastic scattering, which arise from strong absorption, as explained in the case before. Decomposition into the far-side and near-side cross sections is shown in Fig. 45 for ^{22}Ne+^{13}C, where the F/N amplitudes are equal at $\theta = 33.5^o$, and for ^{22}Ne+^{12}C, where the F/N amplitudes are equal at $\theta = 37^o$. Beyond these angles, the far-side components are relatively stronger and dominate the cross sections. The radial sensitivity of the potential was determined by a Gaussian spike superimposed on the real potential at a given radius using Eq. (4.10). Figure 45 shows that the radial sensitivity of the potential is maximized near 6.5 fm, well inside the strong absorption radius of 7.9 fm.

4. WKB Approximation

The semiclassical WKB approximation is applied to study the effects of the nuclear interior on the reaction mechanism and to distinguish between the refractive and absorptive processes. Figure 46 shows the power of applying the Brink and Takigawa theory to the elastic scattering of ^{22}Ne+^{12}C. It reproduces almost exactly the quantum S-matrix using the simple classical concepts of the complex turning points. For particles such as ^{22}Ne, where many non-elastic channels are available, absorption is expected to dominate the mechanism and the reaction is favorable for ANC purposes. However, in this specific reaction, the refractive effects are not completely hidden. The internal barrier component is small but still significant to produce a rainbow effect at large angles. The interference between the barrier and internal barrier components is near the grazing angular momentum $\ell_g = 31$. The barrier component resembles a strong absorption profile beyond ℓ_g. The average value for $|S(\ell)|$ in the region where $\ell \leq \ell_g$ is approximately 3×10^{-3}. The decomposition of the scattering

amplitudes using Eq. 4.12 in Fig. 47 shows the dominance of the barrier component at forward angles, while the internal barrier starts to be effective at angles larger than 60^o. On the other hand, the optical potentials for ^{22}Ne+^{13}C scattering do not have well separated complex turning points. Therefore the WKB theory was not applied.

5. The Neutron Transfer Reaction

The neutron transfer reaction ^{13}C(^{22}Ne,^{23}Ne)^{12}C has been measured for spectrometer angles 3^o, 5^o, 7^o, and 10^o in the laboratory system, which covers the angular range 3^o-32^o in the C.M. The neutron transitions from the $1p_{1/2}$ orbital in ^{13}C to the $1d_{5/2}$ and $2s_{1/2}$ orbitals in ^{23}Ne were detected with a good separation between their positions along the x-axis of the focal plane inside the ionization chamber. The DWBA descriptions of the transfer reaction cross sections were calculated using PTOLEMY and FRESCO. The states were considered $d_{5/2}$ and $s_{1/2}$, respectively, a neutron single particle coupled to the g.s. of ^{22}Ne. The calculations were done using the OMP obtained from ^{22}Ne+^{13}C scattering for the entrance channel of the reaction, while the OMP extracted from the scattering of ^{22}Ne+^{12}C were used as inputs for the outgoing channel. The comparisons between the data and the calculations are plotted in Figs. 48 and 49.

Fits of the DWBA calculations to the data are shown in Fig. 48 when the ground state of ^{23}Ne is populated and Fig. 49 when the $J^\pi = 1/2^+$ first excited state is populated. A systematic angular phase shift of about 0.2^o in the laboratory system was observed between the data and the DWBA cross sections. Measurements for the transfer reaction were taken concurrently with ^{22}Ne+^{13}C elastic scattering. Therefore, any error in the incident beam energy would need to be common. Decreasing the angular distribution of the elastic scattering data by 0.2^o, then attempting to find new optical

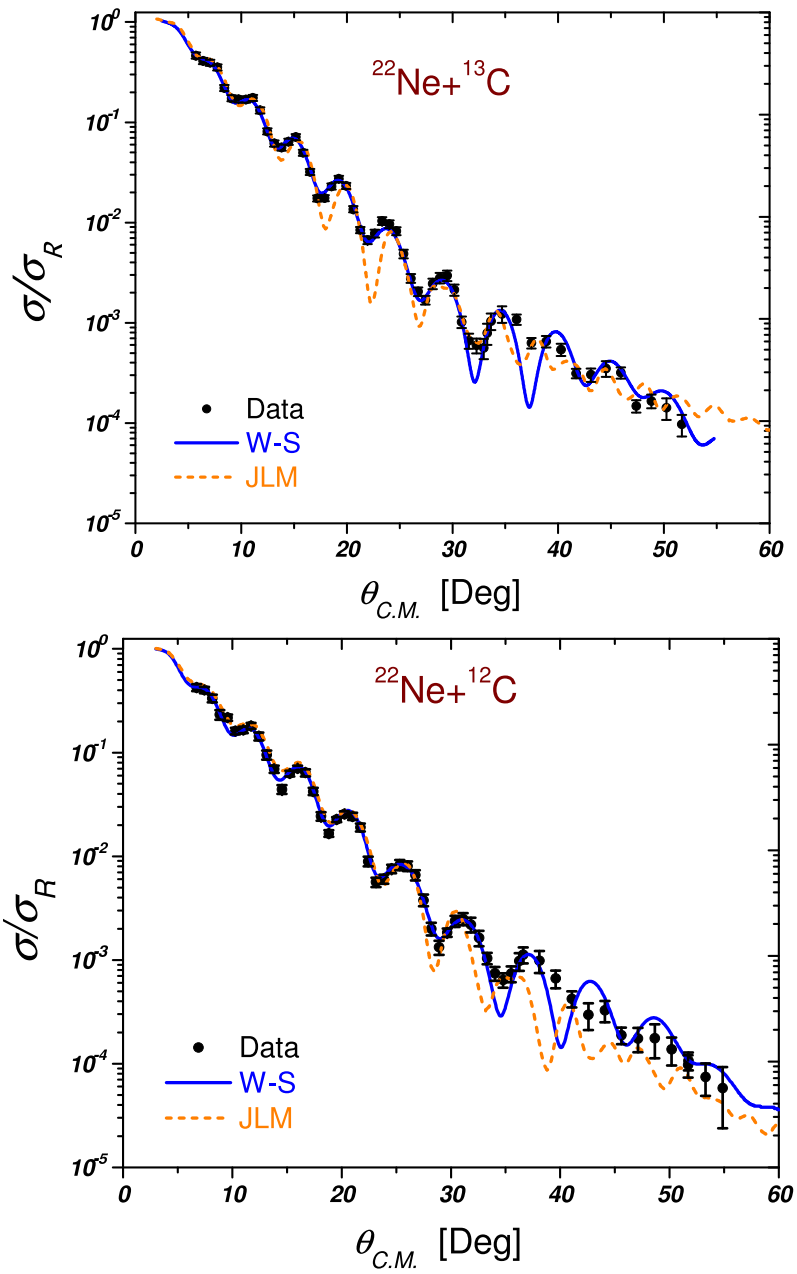

FIG. 43. The angular distributions for the elastic scattering of ^{22}Ne+^{13}C, the top figure, and ^{22}Ne+^{12}C, the bottom figure. The data were fit with Woods-Saxon and double folded potentials. The Woods-Saxon fit was calculated using the optical potential $V = 81$ MeV of Table V for ^{22}Ne+^{13}C and the optical potential $V = 77$ MeV for ^{22}Ne+^{12}C.

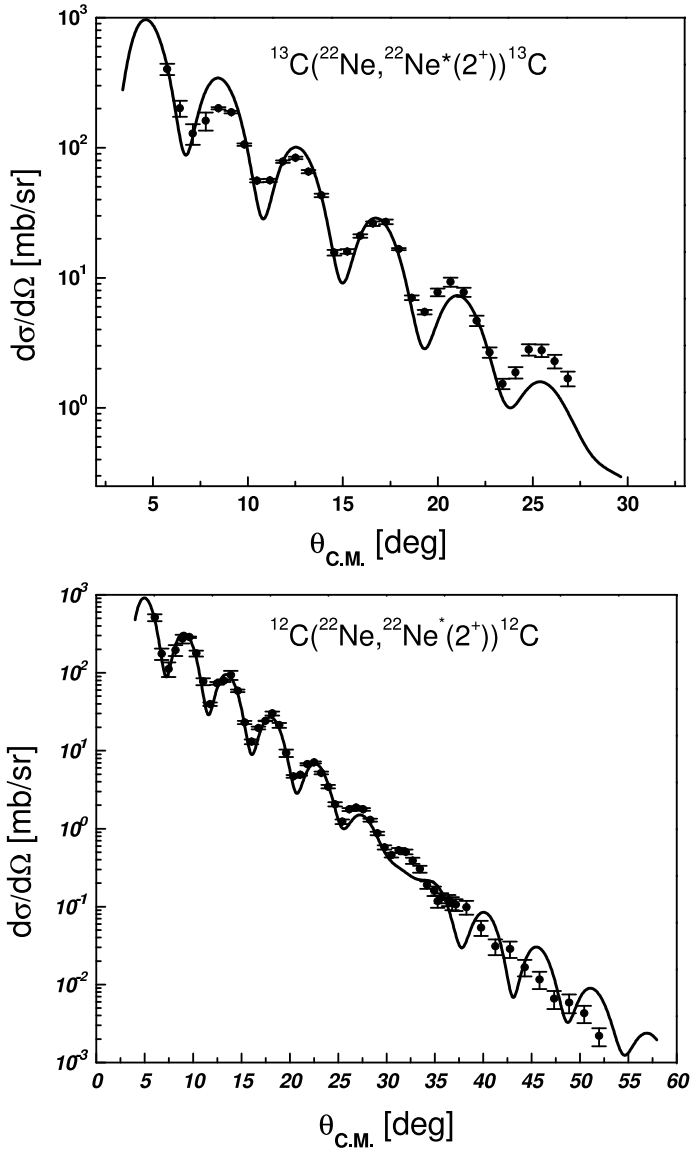

FIG. 44. The top figure shows the inelastic scattering angular distribution of ^{13}C(^{22}Ne,^{22}Ne* $[J^\pi = 2^+, E = 1.275$ MeV$]$)^{13}C. The solid line curve was calculated using the optical potential $V = 81$ MeV of Table V with a deformation $\beta = 0.560$. The inelastic scattering for ^{12}C(^{22}Ne,^{22}Ne$^*[J^\pi = 2^+, E = 1.275$ MeV$]$)^{12}C is shown in the bottom figure. The solid line curve was calculated using the optical potential $V = 77$ MeV after being deformed with β.

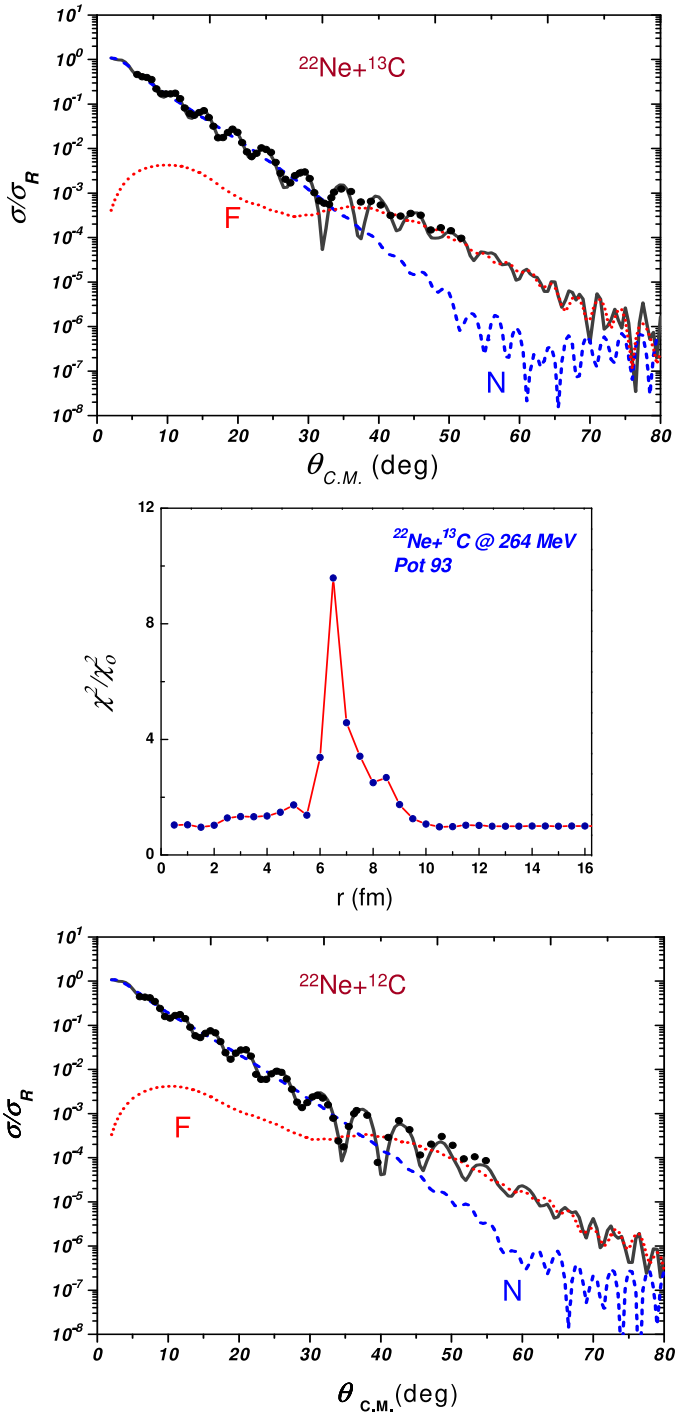

FIG. 45. The upper figure shows the Woods-Saxon far-side (dots) and near-side (dashes) decomposition for ^{22}Ne+^{13}C elastic scattering using the optical potential $V = 81$ MeV of Table V. The radial sensitivity test on the real potential as a function of r is shown in the middle figure. The F/N decomposition for ^{22}Ne+^{12}C scattering using the potential $V = 77$ MeV is illustrated in the lower figure.

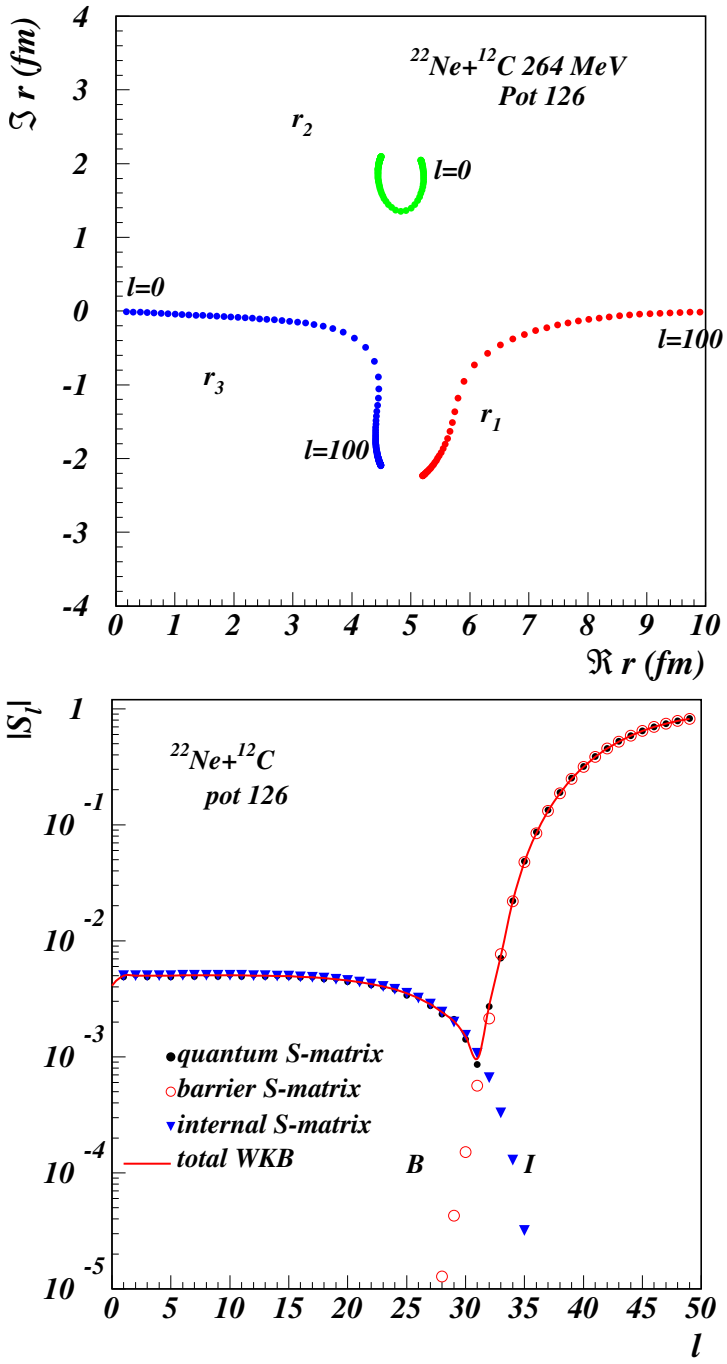

FIG. 46. Trajectories of the complex turning points for ^{22}Ne+^{12}C elastic scattering using the potential $V = 126$ of Table V are shown in the upper figure. The lower figure proves that the S matrix is dominated by the barrier component after $\ell_g = 31$, therefore the reaction mechanism has a strong absorption profile.

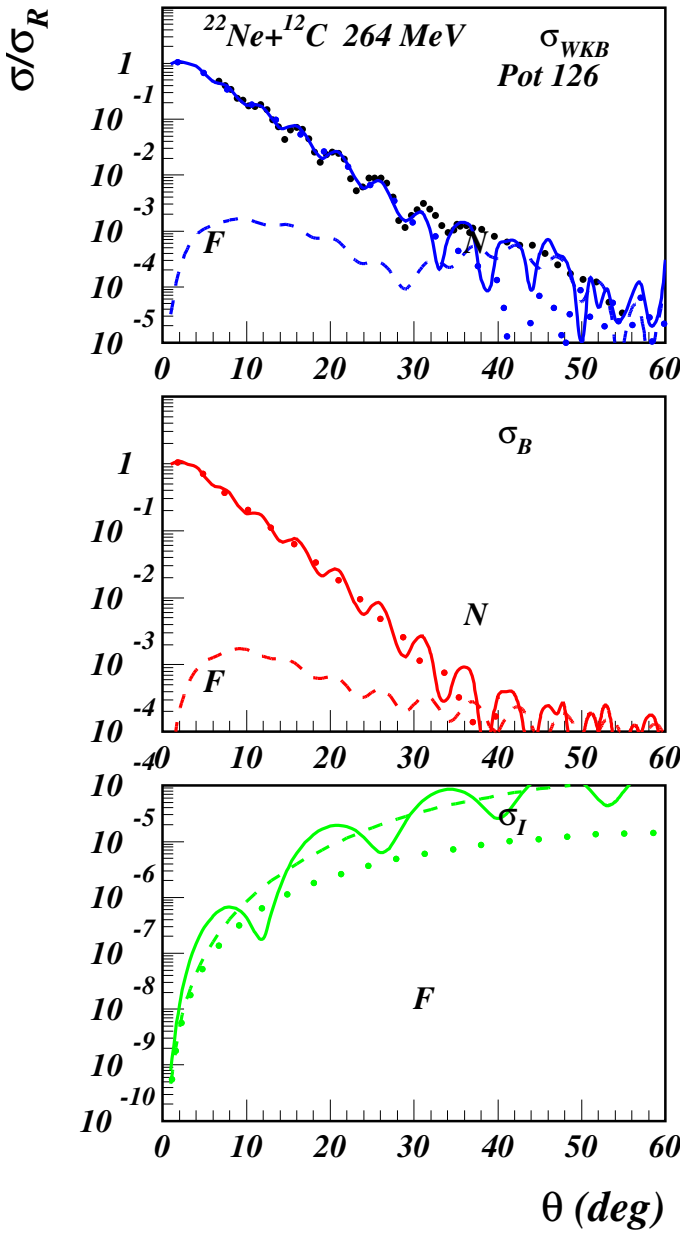

FIG. 47. The semiclassical calculations have been checked by comparing the exact quantum-mechanical result in Fig. 46, upper panel, with the barrier, middle panel, and internal barrier, lower panel, components of the ^{22}Ne+^{12}C elastic scattering cross section. Each component is further decomposed into far-side (dashed) and near-side (dotted) components. The semiclassical B/I expansion describes an exact decomposition of the quantum results.

potentials that give a good description for both mechanisms simultaneously completely failed. Moreover, the inelastic scattering cross section data do not have any phase difference with the calculations, especially at forward angles. The contribution of the excited states to the final result was studied. The cross section of ^{22}Ne+^{13}C $\left(\mathrm{J}^{\pi}=\frac{1}{2}^{+}, 3.09\mathrm{MeV}\right) \rightarrow {}^{23}$Ne+^{12}C leads to an angular distribution that has Fraunhofer oscillations that are out of phase with the direct g.s. to g.s. transfer reaction, so its contribution is neglected, while the calculated $^{22}\mathrm{Ne}\left(\mathrm{J}^{\pi}=2^{+}, 1.275\mathrm{MeV}\right)+$ $^{13}\mathrm{C} \rightarrow {}^{23}\mathrm{Ne}+{}^{12}\mathrm{C}$ reaction has an in-phase angular distribution. The calculation of the coupled-channel Born approximation (CCBA) [93], instead of the DWBA, also did not succeed in solving the angular shift. The CCBA was done using FRESCO, where the absolute values of the cross section in the direct transfer reaction are not constant and depend on the strength of the coupling. Therefore, to keep the results of the transfer reaction consistent with the elastic and inelastic scatterings, the 0.2^{o} shift will be counted as a systematic uncertainty in the value of the ANC. A similar angle shift was seen, but not resolved, for proton transfer from the p-shell to the sd-shell in the ^{13}C(^{7}Li,^{6}He)^{14}N [94] and ^{13}C(^{14}N, ^{13}C)^{14}N [95] reactions.

6. Extracting the ANCs

The asymptotic normalization coefficients were extracted by inserting the proper quantum numbers in Eq. (2.51), such as

$$\frac{d\sigma}{d\Omega}=C_{p_{1/2}}^{2}\left({}^{13}\mathrm{C}\right) C_{d_{5/2}}^{2}\left({}^{23}\mathrm{Ne}\right) \frac{\sigma^{DWBA}}{b_{p_{1/2}}^{2}\left({}^{13}\mathrm{C}\right) b_{d_{5/2}}^{2}\left({}^{23}\mathrm{Ne}\right)} \tag{4.16}$$

for the reaction ^{13}C(^{22}Ne,^{23}Ne)^{12}C reaction. The adopted value for the ANC $C_{p_{1/2}}^{2}\left({}^{13}\mathrm{C}\right)$ in the last section was used in this equation. In Fig. 50 the values extracted for the ANC $C_{d_{5/2}}^{2}$ are compared with those of the extracted spectroscopic factor $S_{d_{5/2}}$ for different geometries of the Woods-Saxon neutron binding potential: here r_o and a

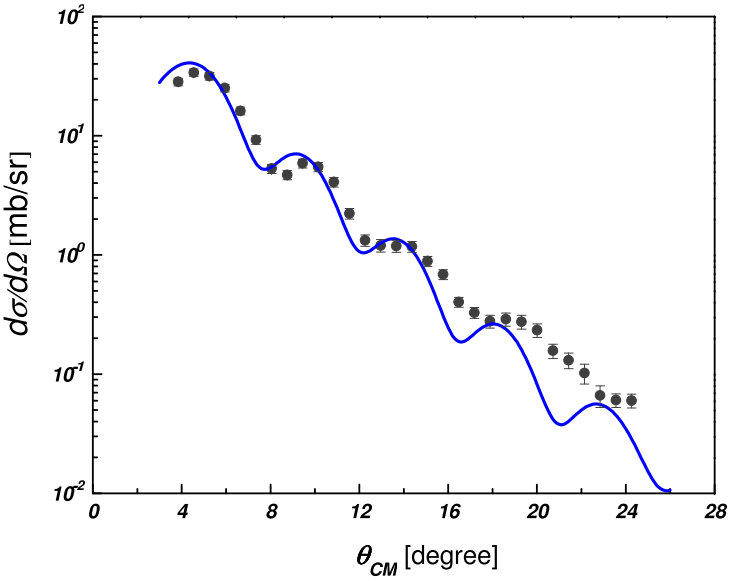

FIG. 48. The angular distribution for a neutron transfer to the ground state of ^{23}Ne from the ^{13}C(^{22}Ne,^{23}Ne)^{12}C reaction.

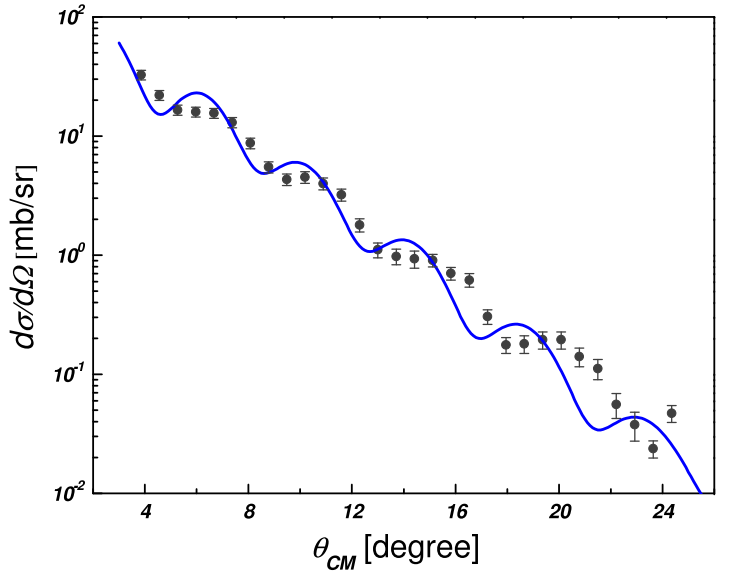

FIG. 49. Angular distribution for the first excited state of ^{23}Ne from the ^{13}C(^{22}Ne,^{23}Ne*(1.275 MeV)^{12}C reaction.

were varied over the ranges 1.1-1.35 fm^{-1} and 0.5-0.7 fm^{-1}, respectively. Again, for each geometry the depth of the potential was adjusted to reproduce the experimental neutron binding energy. The figure shows that the model dependent value of S varies by almost 45% around its mean value, while the ANC is almost constant, with a variation of less than 2% over the full range. Hence, the reaction is peripheral. Similar conclusions can be drawn from the comparison of the excited state ANC $C^2_{s_{1/2}}$ and $S_{s_{1/2}}$, as illustrated in Fig. 51.

The ANCs $C^2_{d_{5/2}}$ and $C^2_{s_{1/2}}$ were obtained by fitting the calculation to the data up to $\theta_{C.M.} = 16^o$. Beyond this angle other multi-step processes may be involved. The uncertainty in the value of the g.s. C^2 includes the (3.5%) from the determination of the ANC $C^2_{p_{1/2}}$ (^{13}C) of the other vertex of the reaction, (7.5%) from the measurement of the target thickness, (2%) from the geometry of the neutron binding potential used in the DWBA calculation, (1.5%) from calculating the cross section with several permutations of entrance versus exit optical potentials in Table V, and (3%) statistical errors. Therefore, the overall uncertainty in determining the C^2 is almost 9%. The systematic uncertainty due to the 0.2^o angle shift in the angular distributions was also calculated. The angles of the transfer reaction cross section were reduced by 0.56^o in the C.M. system. A new normalization between the DWBA and the data cross sections showed that the fit was dramatically improved up to $\theta_{C.M.} = 19^o$ but the value of $C^2_{d_{5/2}}$ was decreased by 14%. Similar calculations showed that the $C^2_{s_{1/2}}$ was changed by almost 20%.

In conclusion, the ANCs in ^{23}Ne are $C^2_{d_{5/2}} = 0.86 \pm 0.08 \pm 0.124$ fm^{-1} and $C^2_{s_{1/2}} = 18.22 \pm 1.82 \pm 3.76$ fm^{-1}. These values or their corresponding nuclear vertex constants $|G|^2$ have not previously been measured experimentally. However, as mentioned in

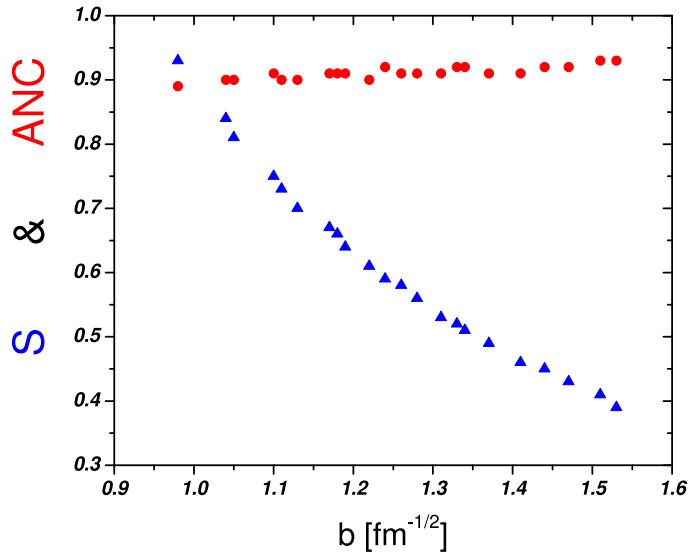

FIG. 50. The comparison between the spectroscopic factor $S_{d_{5/2}}$ (blue triangles) and the ANC $C^2_{d_{5/2}}$ (red dots) for the ground state of ^{23}Ne as a function of the single particle ANC $b_{d_{5/2}}$.

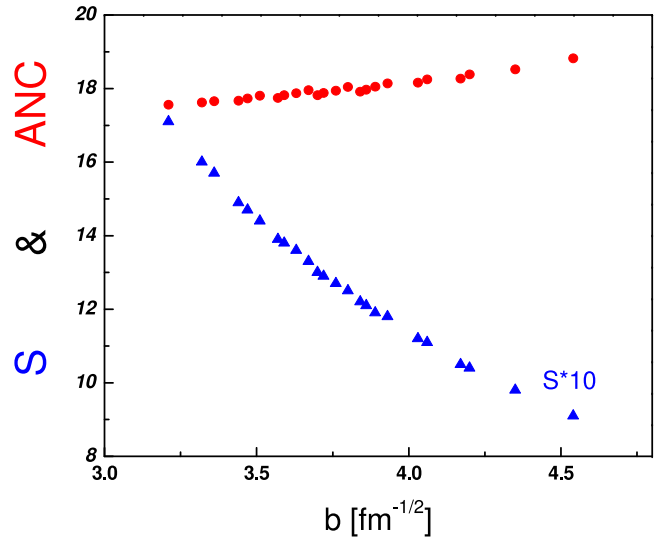

FIG. 51. The comparison between the spectroscopic factor $S_{s_{1/2}}$ (blue triangles) and the ANC $C^2_{s_{1/2}}$ (red dots) for the first excited state of ^{23}Ne as a function of the single particle ANC $b_{s_{1/2}}$. Note that $S_{s_{1/2}}$ has been multiplied by 10.

the second Chapter, the calculated value for $C^2_{d_{5/2}}$ is 0.71-0.81 fm^{-1} and for $C^2_{s_{1/2}}$ is 16.30-18.49 fm^{-1} as reported in [59] and [65], respectively. The experimental results are consistent with these calculations.

D. The ^{13}C(^{17}O,^{18}O)^{12}C Experiment

To extract the ANCs for the first two $J^\pi = 2^+$ states in ^{18}Ne, which are important to estimate the reaction rate of ^{17}F$(p,\gamma)^{18}$Ne in ONe novae, the ^{13}C(^{17}O,^{18}O)^{12}C reaction has been measured to determine the ANCs of the mirror states in ^{18}O. Following the same procedure as in the previous two sections, the analysis of the experimental results is presented here, while the astrophysical part will be discussed in the next chapter.

1. Elastic Scattering of ^{17}O+^{13}C and ^{18}O+^{12}C

To obtain the right optical potentials for the entrance and exit channels, the elastic scattering measurements were successfully carried out with two different beams. First, the ^{17}O beam at 12 MeV/nucleon impinged on a ^{13}C target. The elastic scattering angular distribution was measured for the angular range 2^o-27^o in the laboratory system. The $4^o \times 1^o$ wide-opening mask and the 5-finger mask were used for each spectrometer angle to double-check the absolute values of the cross section and the quality of the angle calibration. RAYTRACE was used to calculate the position of the focal plane, mainly at large angles when it was located far in front of the Oxford detector. The position, or energy, calibration was discussed at the beginning of the current chapter. Second, following the same steps, a ^{12}C target was bombarded by an ^{18}O beam with 12 MeV/nucleon total laboratory energy. The elastic scattering cross section was measured at 4^o-22^o spectrometer angles, allowing one degree overlap

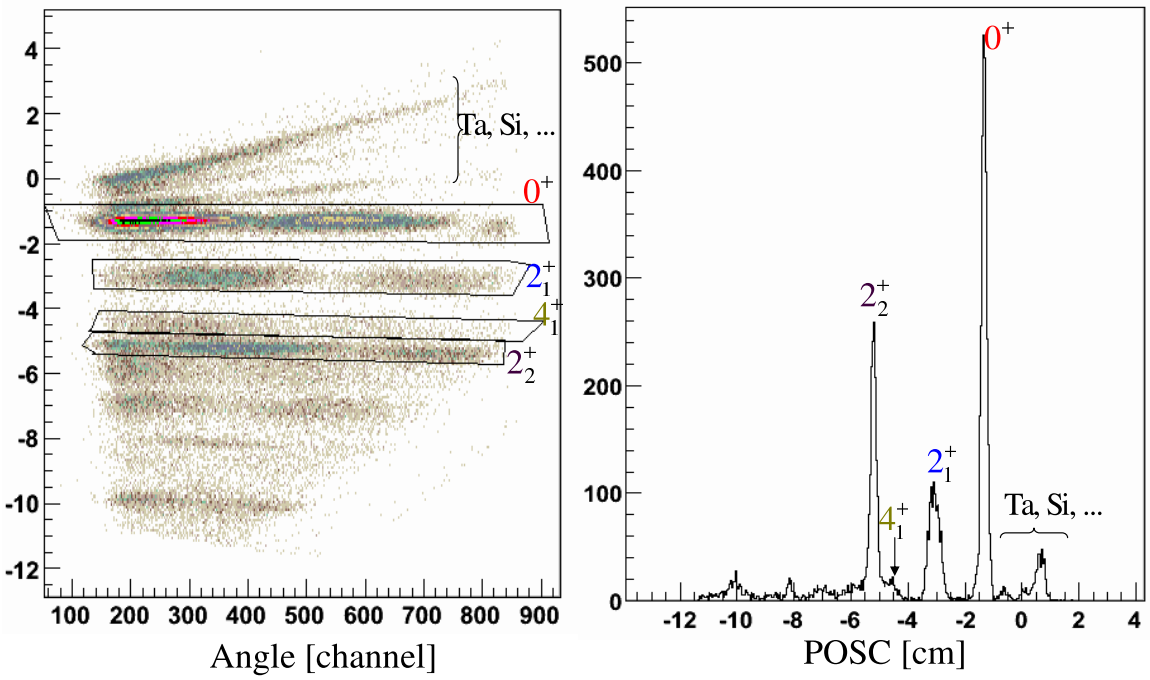

FIG. 52. The picture of the raw data for the ^{18}O+^{12}C elastic scattering in the focal plane, and the projection of the ground and low-lying excited states on the POSC axis.

between consecutive MDM settings. The quality of the angular resolution, $\Delta\theta_{res}$, of the detector in both cases was 0.23^o at small angles, then it decreased to 0.40^o at larger angles. An example of the raw data for ^{18}O+^{12}C scattering at 7^o is illustrated in Fig. 52. The high purity of the target allowed measurement of the elastic scattering down to $\theta_{lab} = 2.4^o$ without contamination from heavy elements in the target. In addition to the elastic scattering, the inelastic scattering for the excited state ($J^\pi = 5/2^-$, 3.842 MeV) of ^{17}O, and first ($J^\pi = 2^+$, 1.982 MeV), second ($J^\pi = 4^+$, 3.554 MeV), and fourth ($J^\pi = 2^+$, 3.920 MeV) excited states of ^{18}O were observed and measured. The elastic scattering angular distributions for ^{17}O+^{13}C and ^{18}O+^{12}C are shown in Figs. 53 and 54, respectively.

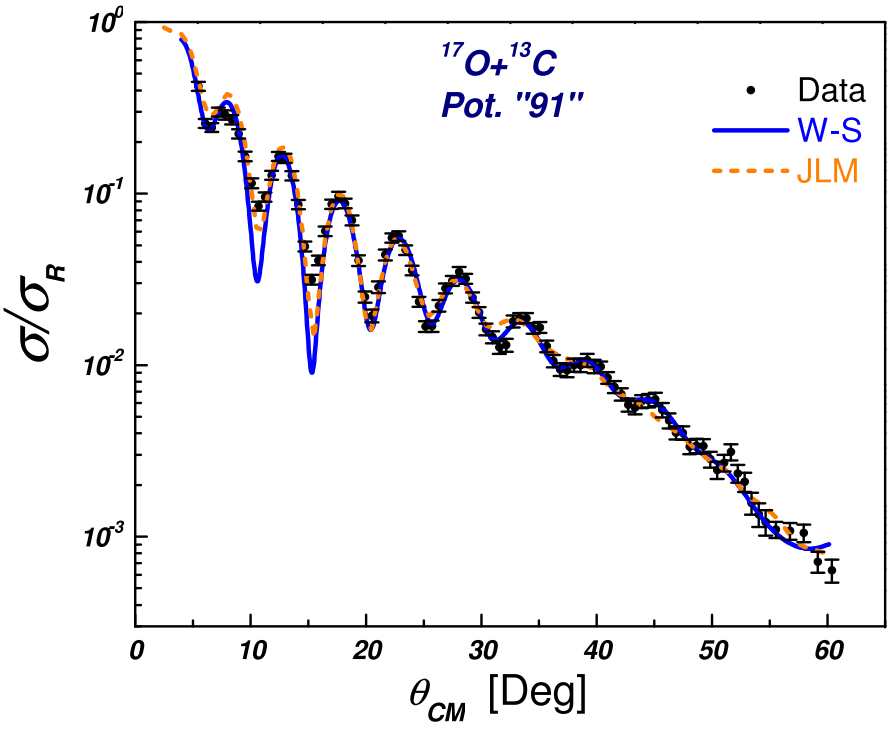

FIG. 53. The angular distribution for the elastic scattering of ^{17}O+^{13}C. The data are well described by the Woods-Saxon and double folding potentials. The optical potentials related to $V = 91$ MeV of Table VI are used in PTOLEMY to get the best fit.

2. Optical Model Potentials

Using the chi square as criterion to get the best fit of the data, five distinct families of potentials with standard Woods-Saxon volume form factors were obtained for ^{17}O+^{13}C scattering, and four sets for the ^{18}O+^{12}C case. Their parameters are presented in Table VI, where again only central potential terms have been included in the OPTIMINIX code. All of the potentials give relatively small χ^2, but only those with the smallest values for the entrance and exit channels were adopted later in the DWBA calculations of the neutron transfer reaction, while the others will be used to determine the uncertainty in the choice of the OMP either in the entrance or exit

TABLE VI. The parameters of the Woods-Saxon optical model potentials obtained from the analysis of the elastic scattering data for ^{17}O+^{13}C and ^{18}O+^{12}C, where $r_c = 1$ fm for all potentials.

Channel	Pot	V [MeV]	W [MeV]	r_V [fm]	r_W [fm]	a_V [fm]	a_W [fm]	χ^2	σ_R [mb]	J_V [MeV fm^3]	R_V [fm]	J_W [MeV fm^3]	R_W [fm]
^{17}O+^{13}C	1	91.76	26.89	0.90	1.10	0.86	0.71	4.4	1678	209	4.69	85	4.97
	2	141.75	26.44	0.84	1.14	0.83	0.65	5.0	1660	264	4.45	100	4.98
	3	200.00	21.95	0.70	1.16	0.95	0.65	4.9	1655	276	4.44	88	5.05
	4	266.85	22.46	0.67	1.18	0.92	0.62	5.2	1642	323	4.26	92	5.05
	5	396.30	25.16	0.57	1.14	0.95	0.65	4.9	1647	353	4.14	95	4.97
^{18}O+^{12}C	1	78.00	24.31	0.91	1.15	0.87	0.71	6.2	1724	186	4.74	98	5.11
	2	89.06	26.20	0.88	1.16	0.90	0.70	5.0	1755	200	4.74	108	5.12
	3	189.76	27.18	0.69	1.16	0.96	0.69	8.6	1748	259	4.43	111	5.10
	4	217.55	21.96	0.86	1.36	1.42	0.97	14.0	1695	242	4.24	94	5.20

channel. The elastic scattering fits with those potentials are plotted in Fig. 53 and Fig. 54. The data have also been fitted with the double folding potential using the JLM effective interaction. The adjusted OMPs give a good description of the data at all angles. They were converted to their equivalents of the Woods-Saxon form and included in Table VI. The third and fourth potentials for ^{17}O+^{13}C and the first potential for ^{18}O+^{12}C were obtained from this conversion.

The quality of the extracted optical potentials was checked by studying the inelastic scattering data. The position of the detected excited states in ^{17}O and ^{18}O outgoing particles were reconstructed from the kinematics of the reaction and RAYTRACE. The angular distributions of the inelastic scattering are shown in Fig. 55. It is clear from the figure that the inelastic scattering data are also described well with the phenomenological potentials.

3. Strong Absorptive Optical Potentials

The refractive and absorptive parts of the optical potentials were studied in terms of the far-side and near-side decomposition of the nuclear scattering amplitude. The corresponding parameters of the potentials $V = 91$ MeV and $V = 89$ MeV were used for ^{17}O+^{13}C and ^{18}O+^{12}C scattering, respectively, and their f^+/f^- decompositions are plotted in Fig. 56, where the dashed line represents the f^+ amplitude, the dotted line the f^- amplitude, and the solid line is their coherent interference. The angular range where both amplitudes are comparable is characterized by a typical Fraunhofer diffraction pattern with deep destructive interference at $\theta = 14^o$ for ^{17}O+^{13}C and $\theta = 17^o$ for ^{18}O+^{12}C. At large angles, the far-side component dominates the angular distribution with strongly damped absorption. The radial sensitivity of the OMPs was tested again by perturbing the real potential around its parameters using Eq.

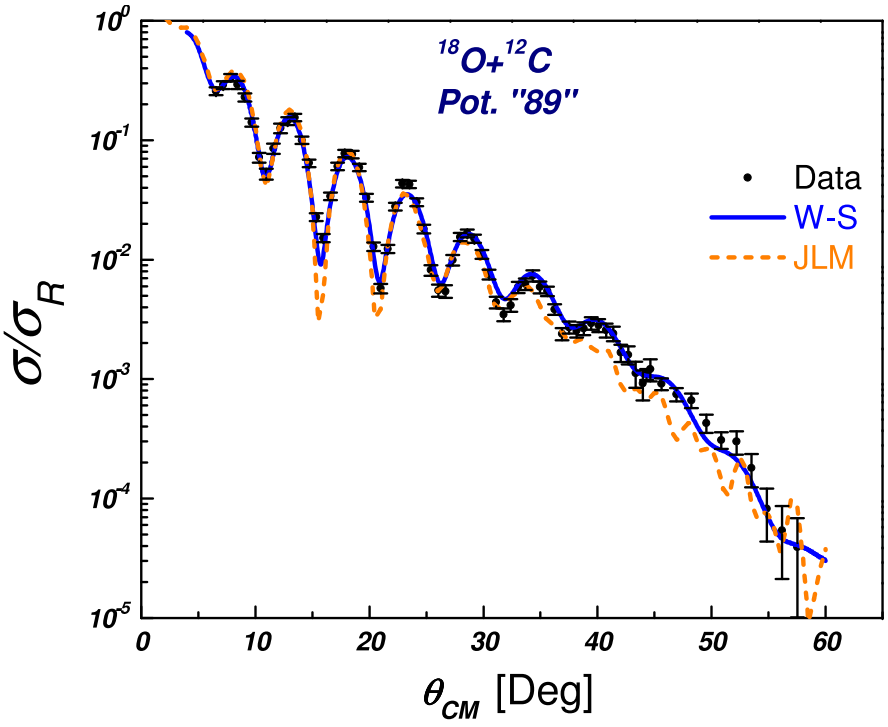

FIG. 54. The fits of the elastic scattering of ^{18}O on ^{12}C. The Woods-Saxon form has been calculated with optical potential $V = 89$ MeV presented in Table VI.

(4.10). The calculations for both systems show an exceptional spike of the optical model potential sensitivity at the surface. The radial sensitivity of the potential is maximized near 6.0 fm, well inside the strong absorption radius of 7.25 fm. This gives the first indication that the nuclear reaction will be peripheral.

4. Semiclassical Approximation

The semiclassical uniform approximation was used to explore the strong absorption profile for the elastic scattering of ^{17}O+^{13}C. The complex turning points that represent the reaction are illustrated in Fig. 57. Those points, which are located near the singular points of the potential, were obtained by extrapolating the Woods-Saxon potential to complex r-values. Clearly the interior turning point r_3 is well separated

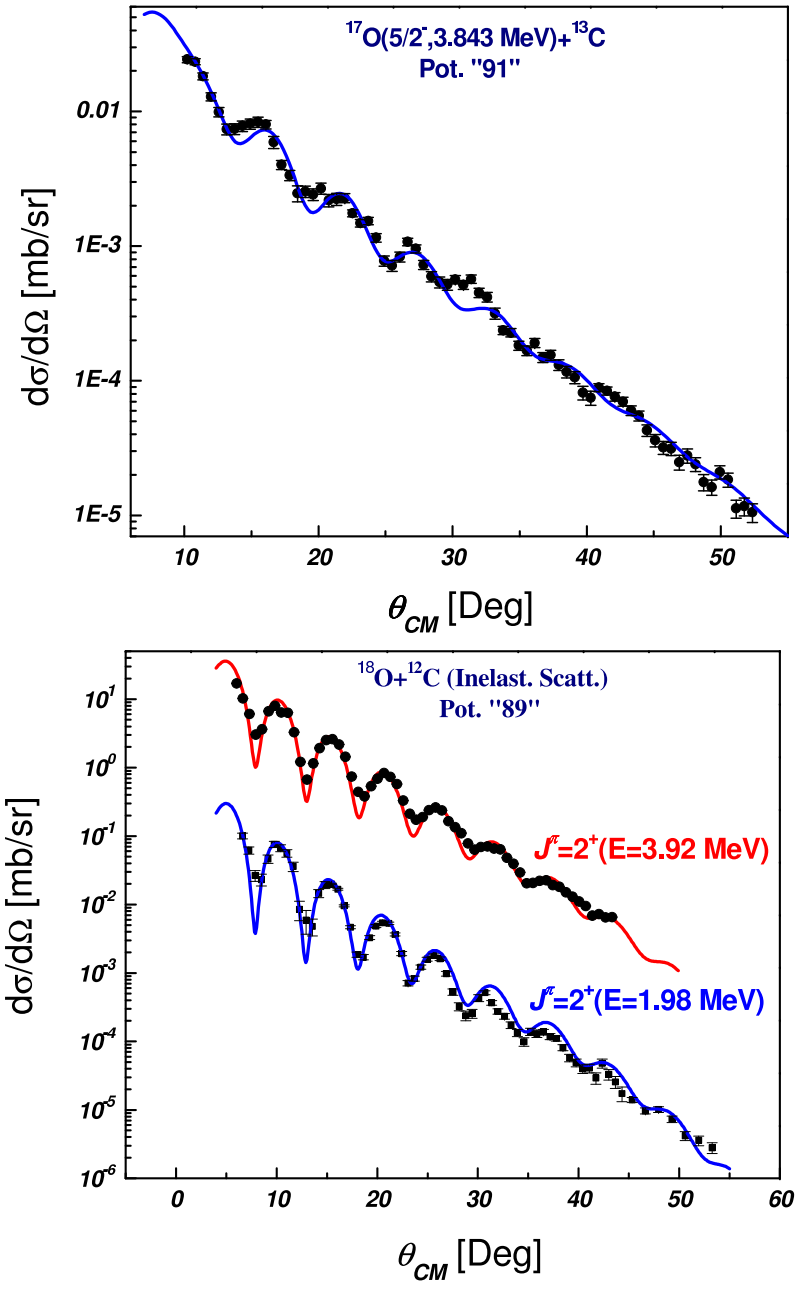

FIG. 55. The upper figure shows the inelastic scattering of $^{17}O^{*}+^{13}C$, while the lower one shows the inelastic scattering of $^{18}O^{*}+^{12}C$. The fits of the inelastic scattering data have been calculated with the optical potentials $V = 91$ MeV for $^{17}O+^{13}C$ and $V = 89$ MeV for $^{18}O+^{12}C$.

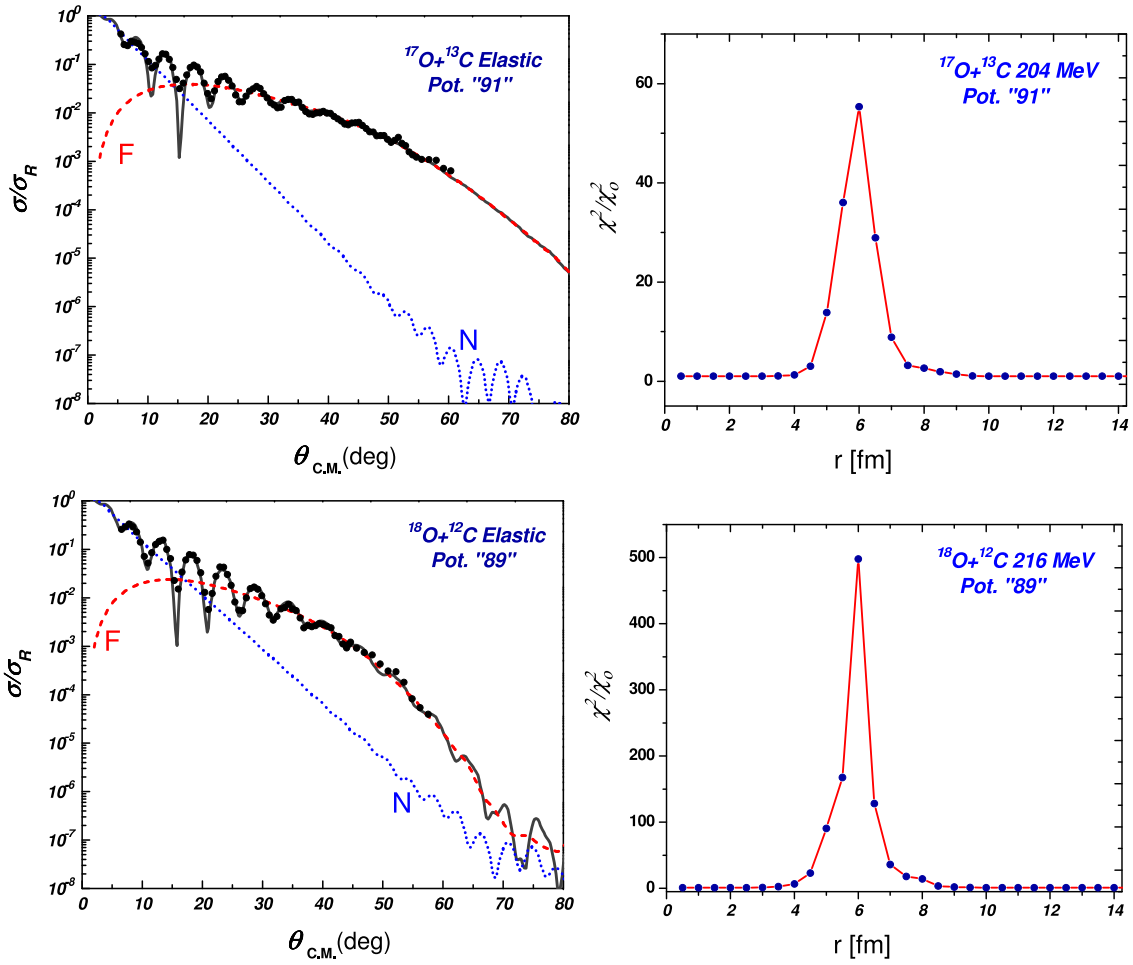

FIG. 56. Woods-Saxon optical model and radial sensitivity analyses of the elastic scattering for ^{17}O+^{13}C, upper figures, and ^{18}O+^{12}O, lower figures. The far-side and near-side decomposition and the Gaussian spike superimposed test confirm the strong absorption profiles in both scattering channels.

from the two turning points r_1 and r_2 in the barrier region for all values of ℓ. These isolated points do not play a significant role in the WKB method, but they show that the semiclassical approximation is quantitatively good for heavy ion scattering. A comparison between barrier and internal barrier components of the WKB in the lower part of Fig. 57 shows that they interfere near the grazing angular momentum $\ell_g = 27$. Beyond that, the WKB $|S_{\ell_B}|$-matrix resembles a strong absorption profile and perfectly reproduces the quantum S-matrix. The average value of $|S_\ell|$ for $\ell < \ell_g$ is of order of 10^{-4}, which indicates a negligible internal, refractive contribution to the reaction mechanism. The decompositions between the F/N amplitudes for the barrier and internal barrier and their coherent sum are shown in Fig. 58, where the barrier amplitudes dominate the measured range of the angular distribution. Hence the elastic scattering is strongly absorptive.

5. Measuring the Neutron Transfer Reaction

The neutron transfer reaction ^{13}C(^{17}O,^{18}O)^{12}C has been measured in the laboratory frame for the angular range $2^o - 13^o$, which is equivalent to $5^o - 31^o$ in the C.M. The astrophysically important excited states of ^{18}O, $J^\pi = 2_1^+$, 4_1^+, and 2_2^+, were populated as shown in Fig. 59. It is clear that studying the first $J^\pi = 2_1^+$ (E = 1.982 MeV) state is straight forward. However, due to the limited experimental energy resolution likely dominated by kinematic broadening, $\Delta E_{res} = 350$ keV, it is difficult to obtain direct information about the $J^\pi = 4_1^+$ (E = 3.555 MeV), $J^\pi = 2_2^+$ (E = 3.920 MeV) and $J^\pi = 1^-, E^* = 4.45$ MeV excited states, because there is an overlap between their peaks.

To disentangle the 2_2^+ state from the strongly populated 4^+ state, RAYTRACE was used to determine the expected positions of the low-lying states in ^{18}O along the

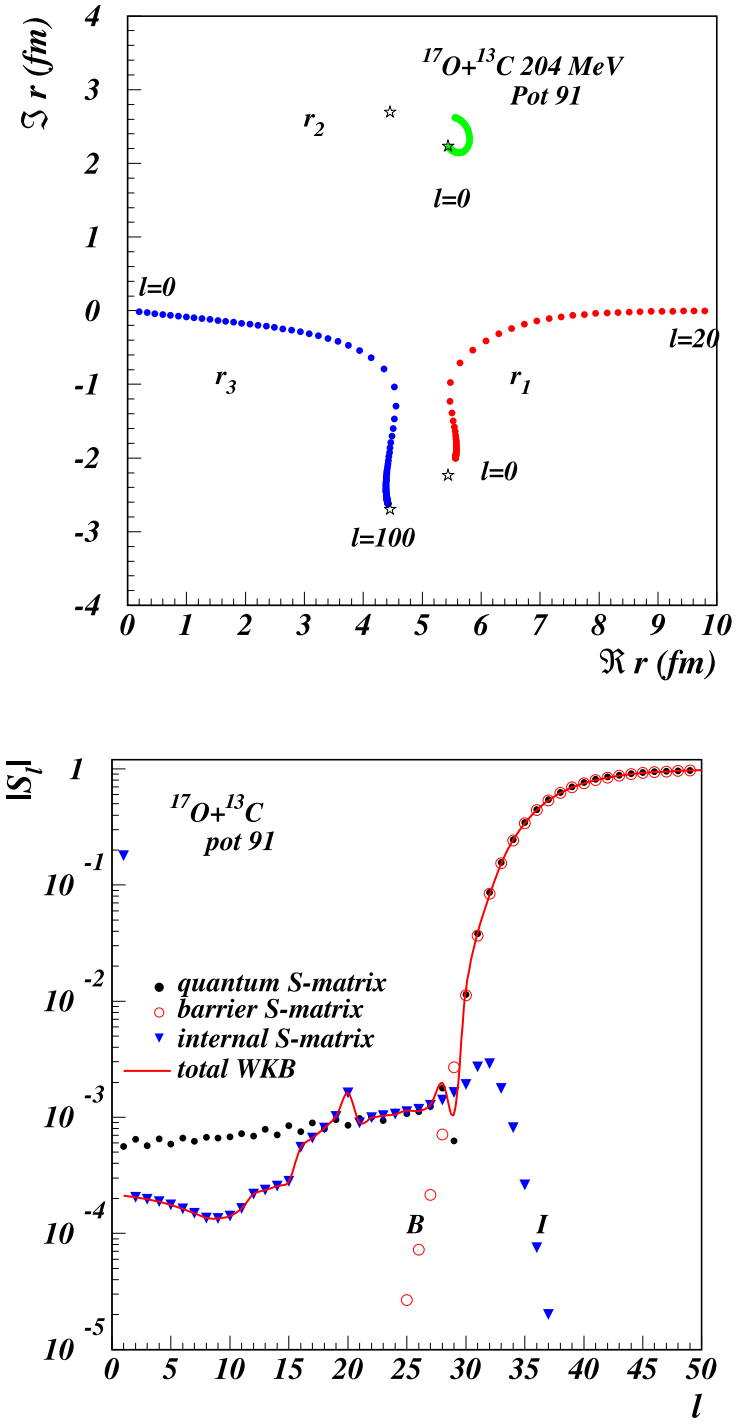

FIG. 57. The upper panel shows the trajectories of the complex turning points for ^{17}O+^{13}C, which are calculated in the semiclassical WKB approximation for the optical potential $V = 91$ MeV. Below, the S matrix for the barrier and internal barrier components as a function of the orbital angular momentum.

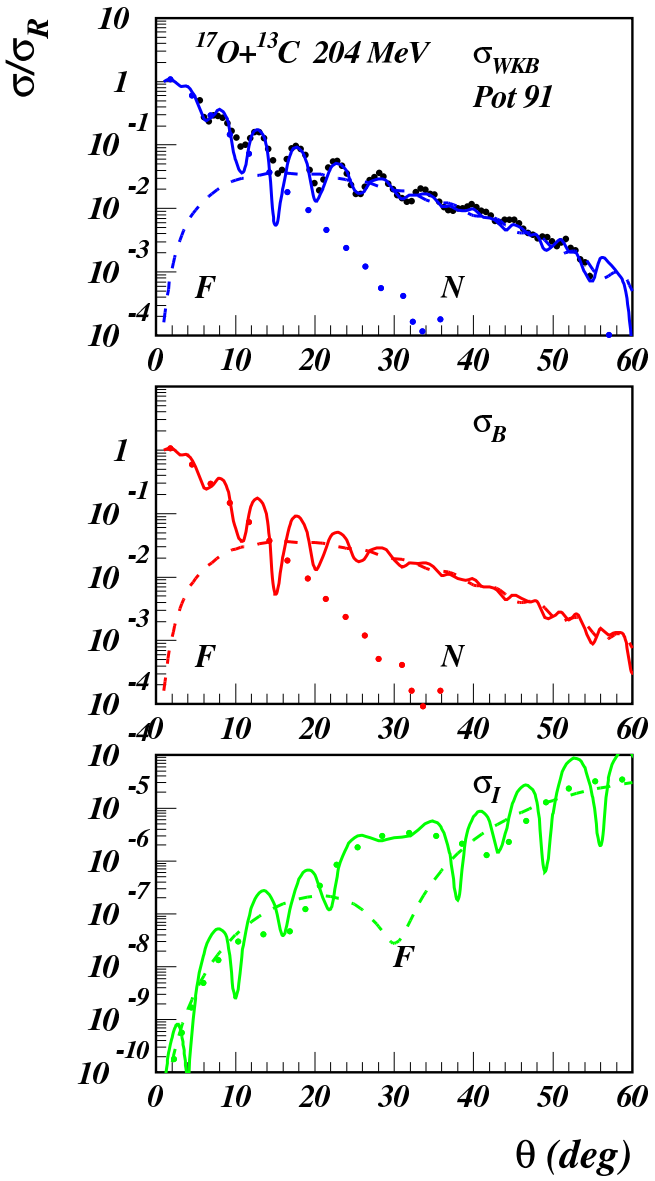

FIG. 58. The semiclassical calculations have been checked by comparing the barrier, middle panel, and internal barrier, lower panel, components of the elastic scattering cross section for ^{17}O+^{13}C. The decomposition of the two amplitudes, upper panel, shows the dominance of the barrier contribution at forward angles. Each component is further decomposed into far-side (dashed), near-side (dotted), and their coherent sum (solid).

dispersive x-axis in the focal plane of the detector, as illustrated in Fig. 59. Using the information about the FWHM of the $J^\pi = 2_1^+$ peak and the known positions of the other states in ^{18}O, a multi-Gaussian macro was written to extract the angular distribution of the inelastic transfer reactions. The spectrum obtained with the $4^o \times 1^o$ wide-mask was divided into eight 0.5^o bins. The measurements at 4^o, 6^o, and 8^o allowed a self-consistency check of the data for at least two bins. The transition to the ground state of ^{18}O was also observed, and its ANC is determined in the following part.

6. Extracting the ANCs

The angular distributions for transfer to the $J^\pi = 0_1^+$, 2_1^+, 4_1^+, and 2_2^+ states in ^{18}O, are shown in Figs. 60-63, respectively. In our transfer calculations, the 2^+ states result from the coupling of $1d_{5/2}$ or $2s_{1/2}$ neutrons to the $\frac{5}{2}^+$ground state of ^{17}O, while the 0_1^+ and 4_1^+ states can only be obtained from adding a $1d_{5/2}$ neutron to the $\frac{5}{2}^+$ core configuration. Therefore, the angular distribution for each 2^+ state is

$$\frac{d\sigma}{d\Omega} = \frac{C^2_{p_{1/2}}\left(^{13}C\right)}{b^2_{p_{1/2}}\left(^{13}C\right)} \left\{ C^2_{\frac{5}{2},\frac{5}{2}}\left(^{18}O\right) \frac{\sigma^{DWBA}_{\frac{5}{2},\frac{5}{2}}}{b^2_{\frac{5}{2},\frac{5}{2}}\left(^{18}O\right)} + C^2_{\frac{5}{2},\frac{1}{2}}\left(^{18}O\right) \frac{\sigma^{DWBA}_{\frac{5}{2},\frac{1}{2}}}{b^2_{\frac{5}{2},\frac{1}{2}}\left(^{18}O\right)} \right\}, \qquad (4.17)$$

while the ANCs for the 0^+ and 4^+ states are extracted using a relation similar to Eq. (4.16). To check the peripherality of the reaction, a comparison between the ANC for the (ds) configuration of the 2_1^+ state versus its corresponding spectroscopic factor for several geometries of the Woods-Saxon potential is illustrated in Fig. 64. The spectroscopic factor varies by almost 23% around the average, whereas the ANC varies by less than 4%, which demonstrates that only the asymptotic part of the wave function contributes in the DWBA calculations and the reaction is peripheral at 12 MeV/A beam energy.

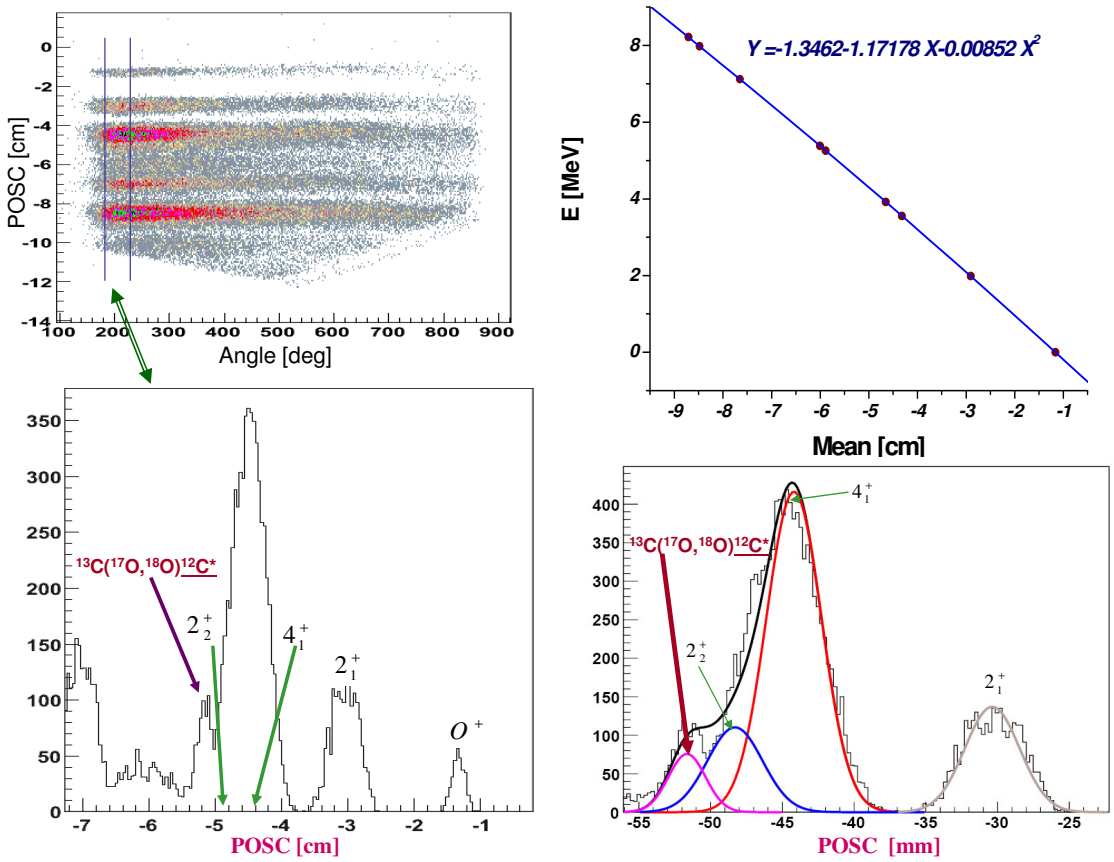

FIG. 59. The procedure that has been followed to disentangle the 2_2^+ state from 4^+ state in the current experiment as it is described in the text. The upper left panel shows the (Angle,POSC) histogram for the transfer reaction ^{13}C(^{17}O,^{18}O)^{12}C when the MDM was at 6^o. RAYTRACE was used to find the relation between the energy of the excited states in ^{18}O and their predicted positions in the detector as illustrated in upper right panel. The lower panels show the expected positions of the 2_2^+ and 4^+ states, and the multi-Gaussian fit that was used to extract their angular distributions.

Uncertainties in the values of the ANCs include 3.5% in the $C^2_{p_{1/2}}$ (^{13}C) that represents the other vertex of the reaction, 7.5% in the thickness of the target, and almost 3% statistical errors. The uncertainties in the selection of the optical potential families, which represent the entrance and exit channels of the reaction, and the geometry of the neutron binding potential used in the DWBA calculation are not the same for all arrangements, but their average values are 2.5% and 3.5%, respectively. The total uncertainty is around 10%.

For the 2^+_1 state, the ANCs were obtained by normalizing the calculated DWBA angular distributions for the (dd) and (ds) configurations simultaneously to the data at C.M. angles between 4^o and 30^o. The resulting ratio of the spectroscopic factors $S(2^+_1)$ $\ell = 0/\ell = 2$ is 0.25, which agrees with the measured ratio 0.2 ± 0.04 reported in [74] and [96]. Weighing the calculations by χ^2 for both configurations simultaneously gives $C^2_{2^+_1}(dd) = 2.06 \pm 0.21$ fm^{-1} and $C^2_{2^+_1}(ds) = 6.55 \pm 0.69$ fm^{-1}. Microscopic cluster model calculations using two effective NN interactions in the form of V2 and MN potentials estimate that $C^2_{2^+_1}(dd) = 3.77$ and 3.00 fm^{-1} [97], respectively, which are slightly larger than the measured value. The same calculations predict that $C^2_{2^+_1}(ds) = 6.15$-7.72 fm^{-1}, which agrees well with the experimentally obtained value.

The ANCs for 2^+_2 state were obtained using the ratio between the spectroscopic factors $S(2^+_2)$ $\ell = 0/\ell = 2$ measured in a ^{17}O$(d,p)^{18}$O reaction, 0.53 ± 0.07 [74]. This ratio was fixed, then the normalizing procedure was performed with one fit parameter that related to the (dd) configuration as

$$\frac{d\sigma}{d\Omega}\Bigg/\frac{C^2_{p_{1/2}}(^{13}C)}{b^2_{p_{1/2}}(^{13}C)} = \frac{C^2_{2^+_2}(dd)}{b^2_{2^+_2}(dd)}\left\{\sigma^{DWBA}_{dd} + 0.53\sigma^{DWBA}_{ds}\right\}. \tag{4.18}$$

Varying the spectroscopic factors ratio by 15% changes the extracted ANCs for the

(dd) and (ds) configurations by almost 4%. This additional uncertainty is included in the total accuracy of the final results. Thus, the ANCs are $C^2_{2^+_2}(dd) = 0.49 \pm 0.06$ fm^{-1} and $C^2_{2^+_2}(ds) = 4.47 \pm 0.54$ fm^{-1}. The microscopic cluster model calculations predict a smaller ANC value for the (dd) configuration, around 0.31 fm^{-1}. They also estimate that $C^2_{2^+_2}(ds) \approx 12$ fm^{-1}, which is almost three times larger than the measured value.

The ANCs for the 2^+ states are most important in determining the astrophysical reaction rate for $^{17}\mathrm{F}(p,\gamma)^{18}\mathrm{Ne}$ in the next Chapter. The ANCs for the 0^+ and 4^+ states in ^{18}O are $C^2_{0^+}(dd) = 7.33 \pm 0.67$ fm^{-1} and $C^2_{4^+}(dd) = 1.05 \pm 0.10$ fm^{-1}, respectively.

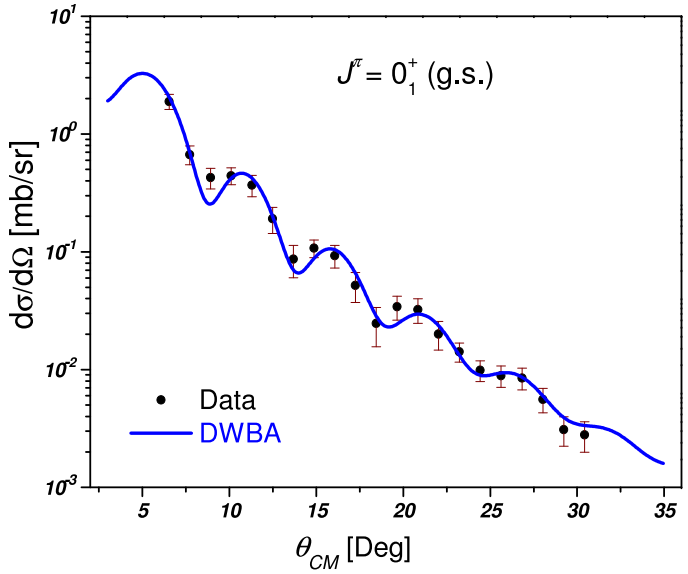

FIG. 60. The angular distribution for the ground state of ^{18}O that resulted from the neutron transfer reaction ^{13}C(^{17}O,^{18}O)^{12}C. Only the (dd) configuration is included in the DWBA calculations.

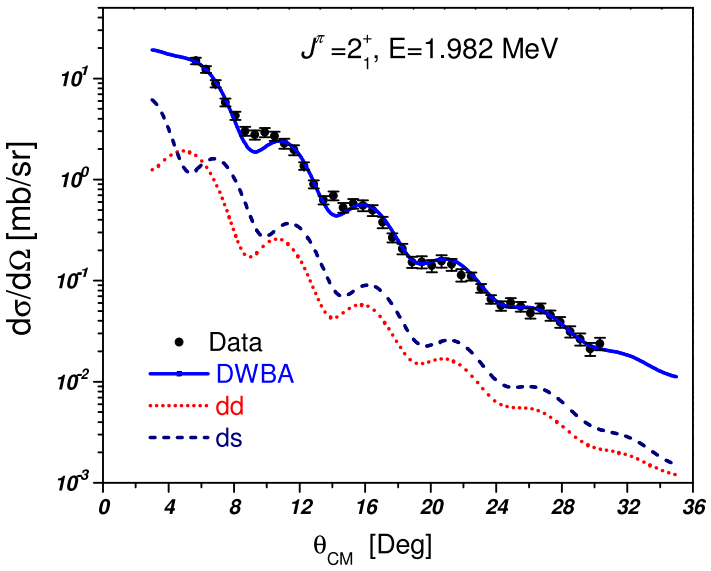

FIG. 61. The cross section values for the first excited state in ^{18}O, $J^\pi = 2^+_1$ at 1.982 MeV, which is populated in ^{13}C(^{17}O,^{18}O)^{12}C reaction. The best DWBA fit is due to the combination of the $p_{1/2} \rightarrow d_{5/2}$ (red dots) and $p_{1/2} \rightarrow s_{1/2}$ (dashed navy) components.

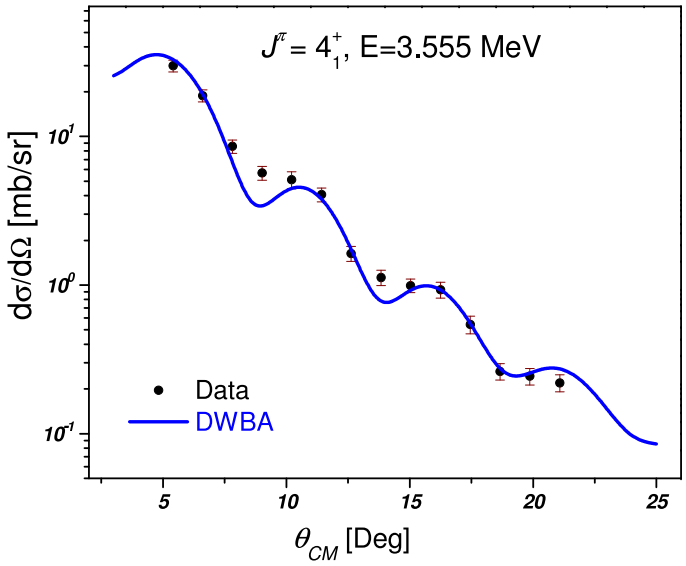

FIG. 62. Same as Fig. 60, but for the $J^\pi = 4^+$ state in ^{18}O at 3.555 MeV.

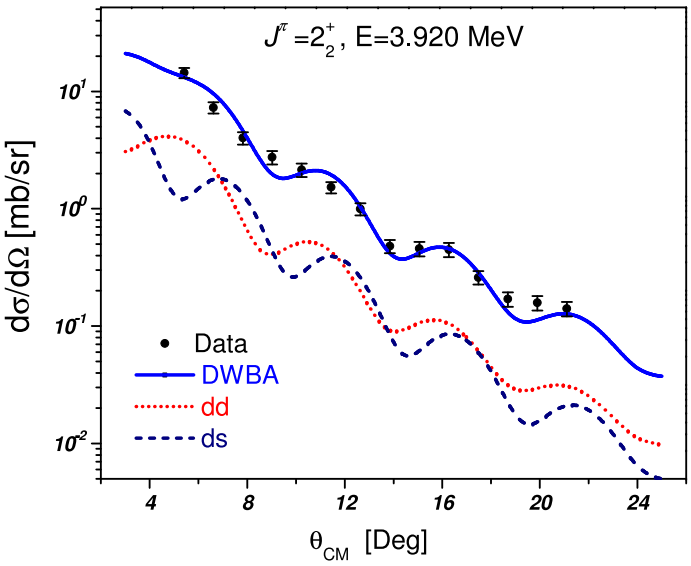

FIG. 63. Same as Fig. 61, but for the $J^\pi = 2^+_2$ state in ^{18}O at 3.920 MeV.

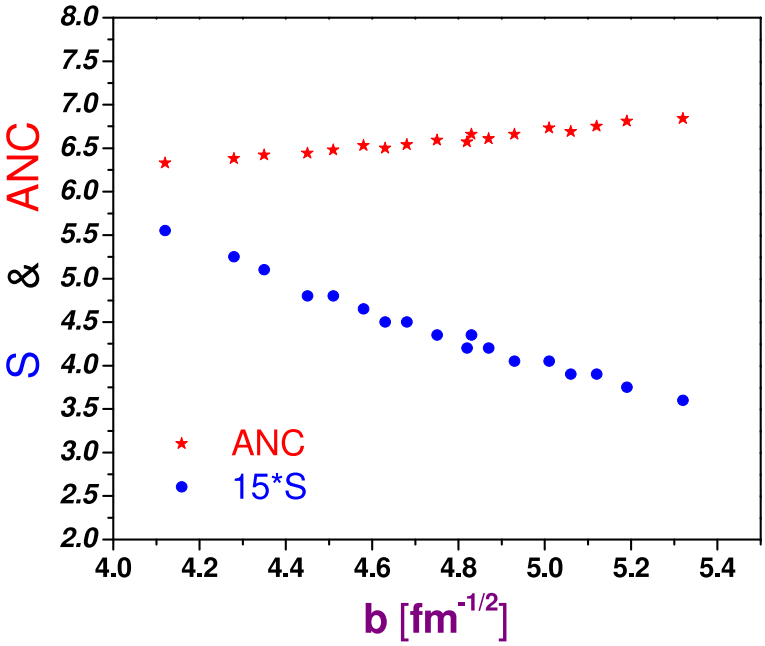

FIG. 64. Comparison of the spectroscopic factors (dots) and of the ANCs (stars) extracted for the $p_{1/2} \rightarrow s_{1/2}$ configuration of the 2^+ state at 1.982 MeV as a function of the single-particle ANC, $b_{2^+}(ds)$.

CHAPTER V

ASTROPHYSICAL REACTION RATES AND CONCLUSIONS

A. The ^{22}Mg(p,γ)^{23}Al Reaction Rate

The ANCs in ^{23}Al were obtained from those measured in ^{23}Ne using their identical spectroscopic factors:

$$S_{nlj}(^{23}\mathrm{Al}) = S_{nlj}(^{23}\mathrm{Ne}) \Longrightarrow \frac{C^2_{n\ell j}}{b^2_{n\ell j}}\left(^{23}\mathrm{Al}\right) = \frac{C^2_{n\ell j}}{b^2_{n\ell j}}\left(^{23}\mathrm{Ne}\right) \tag{5.1}$$

The single-particle ANCs, b, in ^{23}Al were calculated using Eq. (2.48) for a proton bound in a Woods-Saxon potential with the same geometry, $r_o = 1.25$ fm and $a = 0.65$ fm, and the same spin-orbit interaction that were used for a neutron bound in ^{23}Ne. Only the depth of the central potential was adjusted to reproduce the experimental proton binding energy in ^{23}Al. The values obtained for the depth of the nuclear potential by imposing this procedure are similar to the depths of the nuclear potentials found for ^{23}Ne. This is a very good confirmation of the charge symmetry assumption made here. The value of $b_{\ell j}$ strongly depends on the geometrical parameters r_o and a assumed for the potentials. However, the ratio $b^2_{\ell j}(^{23}\mathrm{Al})/b^2_{\ell j}(^{23}\mathrm{Ne})$ is independent of these parameters of the potential that bind the proton or the neutron around its corresponding core. We find that this ratio is equal to 120.0 for $1d_{5/2}$ (the major component of the $J^\pi = \frac{5}{2}^+$ ground state), and 401.65 for $2s_{1/2}$ (the major component of the $J^\pi = \frac{1}{2}^+$ first excited state). Inserting these ratios and the values of the ANCs in ^{23}Ne, which were obtained in the previous Chapter, into Eq. (5.1), we find $C^2_{d_{5/2}}(^{23}\mathrm{Al}) = (1.25 \pm 0.14) \times 10^4$ fm^{-1} and $C^2_{s_{1/2}}(^{23}\mathrm{Al}) = (2.94 \pm 0.35) \times 10^6$ fm^{-1}. An additional 3% uncertainty is assigned to account for possible charge-symmetry

breaking effects [100]. This is the first measurement of its kind to extract the ANCs in ^{23}Al. Their values are used to determine the reaction rate for $^{22}\mathrm{Mg}(p,\gamma)^{23}\mathrm{Al}$, which includes contributions from direct capture to the $J^\pi = \frac{5}{2}^+$ ground state and resonant capture to the $J^\pi = \frac{1}{2}^+$ state.

Estimating the direct capture reaction rate starts with the calculation of the astrophysical S-factor. It was obtained using the RADCAP code [98]. The central depth of the proton binding nuclear potential V_o was adjusted so that the binding energy of the ground state E_p in ^{23}Al is reproduced. The newest value of E_p is 145 keV [55]. The other parameters were fixed in order to maintain the same geometry of the optical potential. Hence, the S-factor can be obtained from $C^2_{d_{5/2}}$ using Eq. (2.53). The bound state wave function was then calculated and used to determine the S-factor at each energy E for a direct, one-step transition from a continuum state to the $1d_{5/2}$ single particle bound state, using Eq. (2.12). The cross section $\sigma_{p\gamma}$ was calculated assuming $E1$ capture only and is proportional to the square of the particular single particle ANC used $b^2_{d_{5/2}}$. However, RADCAP assumes that the spectroscopic factor of the reaction is unity. Therefore, the values obtained must be multiplied with the spectroscopic factor determined from the data of the transfer experiment $S_{d_{5/2}} = \frac{C^2_{d_{5/2}}}{b^2_{d_{5/2}}}$. The dependence of b and the bound state wave function on the geometries of the Woods-Saxon shape factors out, so the value of the ANC $C^2_{d_{5/2}}$ determines the astrophysical S-factor. The S-factor calculation was done for the energy range $E = 0.01$ to 3.0 MeV, in steps $\Delta E = 0.02$ MeV. The calculated energy dependence of the S-factor for the direct proton capture reaction $^{22}\mathrm{Mg}(p,\gamma)^{23}\mathrm{Al}$ is illustrated in Fig. 65, and can be parameterized with a simple polynomial dependence

$$S(E) = 961 + 541E + 33.4E^2, \tag{5.2}$$

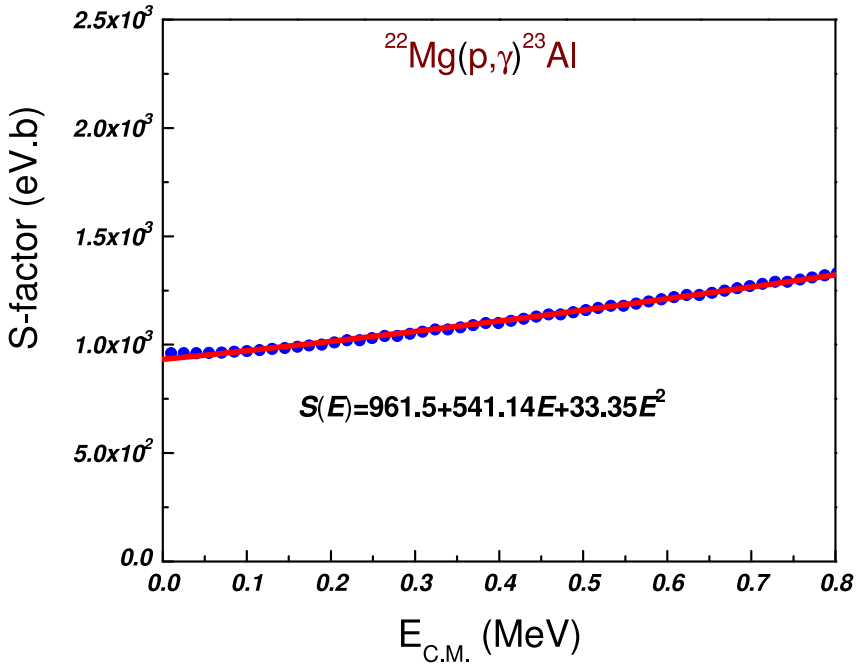

FIG. 65. The dependence of the S-factor on the C.M. energy for the ^{22}Mg$(p,\gamma)^{23}$Al reaction. The curve is almost flat at astrophysical stellar energies. Fitting it with a second degree polynomial function gives $S(0) = 961 \pm 105$ eV b.

where S is in eV b and E in MeV. The $S_{1-22}(0) = 961 \pm 105$ eV b. It was reported in [53] that $S_{1-22}(0) = 663$ eV b, which is almost 30% less than our value. This is due to different values of spectroscopic factors and E_p that were used in each calculation. The central energy of the Gamow peak for $p + {}^{22}$Mg is at $E_o = 0.63T_9^{2/3}$ [MeV]. Inserting this equation into Eq. (2.20), I find for the effective S-factor S_{eff} in terms of T_9

$$S_{eff}\,(T_9) = 961\left[1 + 0.02T_9^{1/3} + 0.36T_9^{2/3} + 0.05T_9 + 0.01T_9^{4/3} + 0.01T_9^{5/3}\right]. \qquad (5.3)$$

Then, substituting this equation and Eq. (2.19) into Eq. (2.22), the direct capture

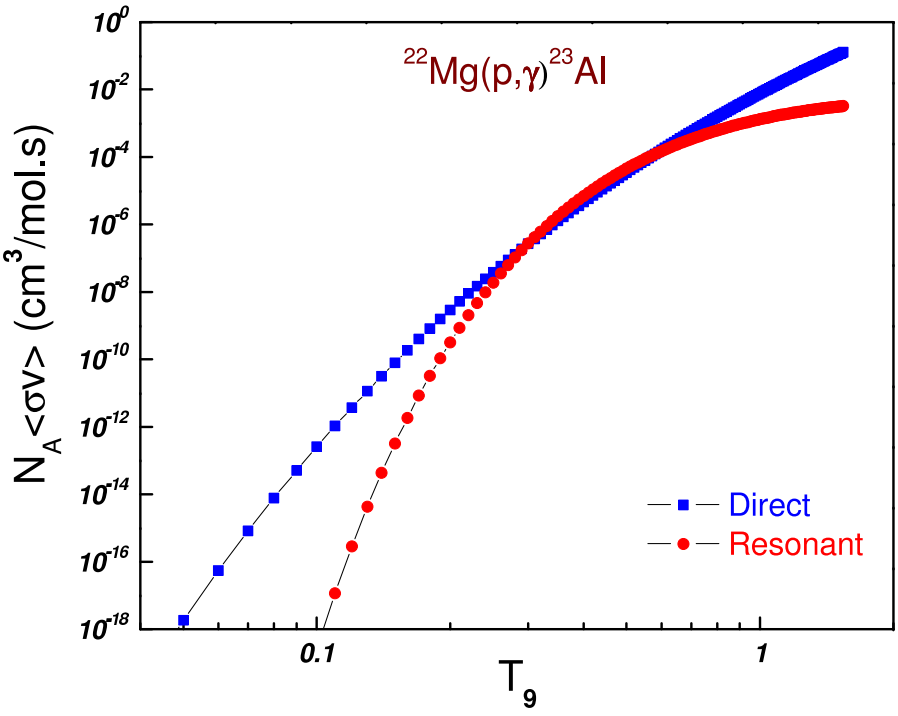

FIG. 66. The direct and resonant capture rate contributions to the ^{22}Mg(p,γ)^{23}Al reaction. The two rates are competitive for temperatures, T_9 = 0.2-0.45, in ONe novae. Otherwise the direct capture dominates the reaction rate.

reaction rate for ^{22}Mg(p, γ)^{23}Al can be evaluated as a function of T_9 using

$$N_A \langle \sigma v \rangle = 37.78 \tau^2 S_{eff}(T_9)\, e^{-\tau} \quad \left[\frac{\text{cm}^3}{\text{mole.s}}\right], \tag{5.4}$$

where $\tau = \frac{21.92}{T_9^{1/3}}$ and S_{eff} is in units of [eV b]. The calculated reaction rate is shown in Fig. 66 as a function of the temperature T_9.

In addition to the direct radiative proton capture calculated above, there is a resonant contribution through the first excited state of ^{23}Al. This resonant contribution to the reaction rate has been estimated using Eq. (2.24). The measured excitation energy for $J^\pi = \frac{1}{2}^+$ in ^{23}Al is 0.528 MeV [53], so the resonance energy, $E_r = E_x - S_p = 528 - 145 =$

0.383(27) MeV. The resonant strength is

$$\omega\gamma = \frac{\Gamma_p \Gamma_\gamma}{\Gamma_p + \Gamma_\gamma}. \tag{5.5}$$

Since for this reaction $\Gamma_p \gg \Gamma_\gamma$, the strength of the resonance is simply equal to Γ_γ. It can be calculated for an $E2$ transition to the ground state of ^{23}Al using [98]

$$\Gamma_\gamma = 8.13 \times 10^{-7} E_\gamma^5[\mathrm{MeV}] \quad \mathrm{B(E2\uparrow)[e^2fm^4]}, \tag{5.6}$$

where $B(E2\uparrow) = 21$ e^{2}fm^4 was calculated using RADCAP. The value calculated from the data of this experiment using the ANCs, or more precisely the spectroscopic factors of the initial $J^\pi = \frac{1}{2}^+$ and final $J^\pi = \frac{5}{2}^+$ states, is $\Gamma_\gamma = 3.9 \pm 0.6 \times 10^{-7}$ eV. This value is slightly smaller than (5.5×10^{-7} eV) predicted in [53], but of the same order of magnitude. Experimental studies of Coulomb dissociation of ^{23}Al at RIKEN give a similar estimate $\Gamma_\gamma = 7.2 \pm 1.4 \times 10^{-7}$ eV [57], while calculations using single-particle wave functions for the $E2$ transition predict 6.0×10^{-7} eV [55]. It should be noted that all calculations referred to above use only the single particle parts from the wave functions of the initial and final state to evaluate the reduced $E2$ transition rate. Consequently, the neglect of collective components leads to underestimation of the $B(E2\uparrow)$ and of the partial gamma-width. The experimental value $\Gamma_\gamma = 7.2 \pm 1.4 \times 10^{-7}$ eV is used in estimating the reaction rate for the resonant term. Hence, Eq. (2.24) for ^{22}Mg(p, γ)^{23}Al becomes

$$N_A \langle \sigma v \rangle = 1.2 \times 10^{-1} T_9^{2/3} \exp\left(-\frac{4.41}{T_9} \right). \tag{5.7}$$

The estimated resonant reaction rate is shown in Fig. 66. In the range $T_9 = 0.2$-0.4, which is typical for ONe novae, the direct and resonant terms are comparable, while for $T_9 > 0.6$ or $T_9 < 0.2$, the direct capture dominates the reaction rate.

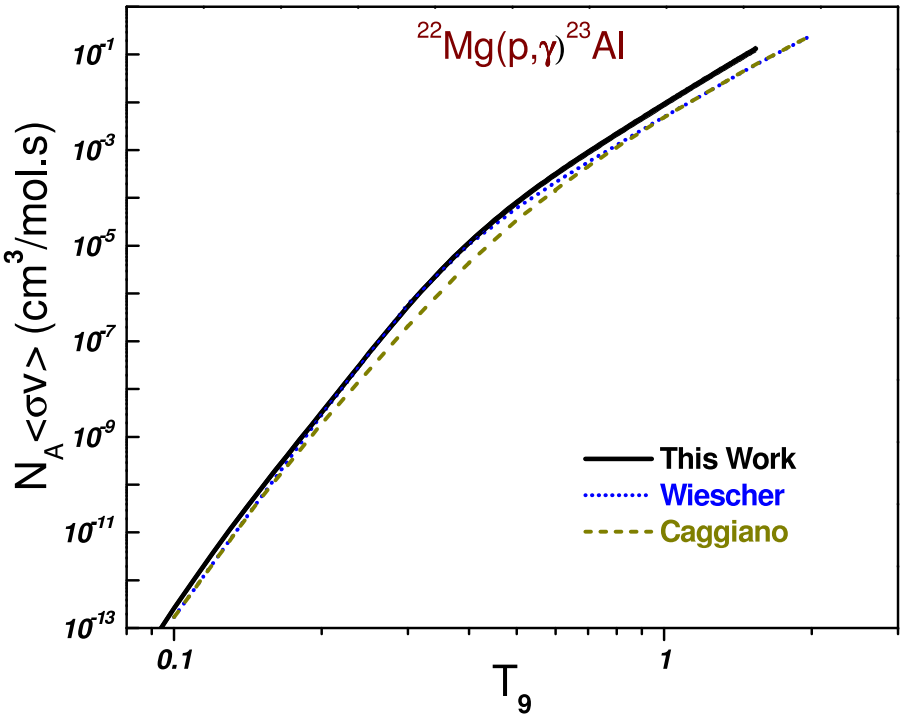

FIG. 67. Comparison between the estimated reaction rate in this work with the previously determined rates by Caggiano [53] and Wiescher [52]. Our rate is similar to that of Wiescher, and almost two times larger than the estimate by Caggiano.

The total reaction rate, which includes the direct and resonant terms, is compared with previous estimates by Wiescher [52] and Caggiano [53] in Fig. 67. The new reaction rate is similar to Wiescher's estimate and is almost two times larger than Caggiano's determinations. This difference is mainly due to the binding energy of the proton in ^{23}Al and the spectroscopic factors, or their equivalent ANCs, that are used in the reaction rate calculations.

The astrophysical implications of the new reaction rate for the nucleosynthesis of ^{22}Na can be inferred from the work of Caggiano and Wiescher. It was shown in [53] that the production of ^{22}Na compensates the loss of ^{22}Mg. This leads to a small mass

fraction increase of ^{23}Al, but it explains less than half of the ^{22}Mg loss. However, the low Q value of the ^{22}Mg(p,γ)^{23}Al reaction makes the proton capture process balance with its photodisintegration reaction ^{23}Al(γ,p)^{22}Mg.

The ^{23}Al(p,γ)^{24}Si reaction has been studied to determine the 2p-capture rate on ^{22}Mg [99] and understand the low production of ^{23}Al. The latter shows that the depletion of ^{22}Mg is larger by a factor of two than its β-decay to ^{22}Na only when $T_9 \approx 0.45$ and the density is in the excess of 10^4 g/cm^3. These conditions may occur in massive novae such as 1.35 M$_\odot$ ONe WD novae. For 1.25 M$_\odot$, where $T_9 \approx 0.35$ and $\rho \approx 10^2 - 10^4$ g/cm^3, the 2p-capture process produces limited amounts of ^{23}Al and ^{24}Si that could not explain the missing long-lived γ-ray emitter ^{22}Na. Wiescher [52] and José [101] suggested that the ^{22}Mg(p,γ)^{23}Al reaction is more important in X-ray bursts, where the extreme temperature and density conditions increase the probability of the proton capture and reduce the β-decay of ^{22}Mg. Nevertheless, our reaction rate for ^{22}Mg(p,γ) still has some impact on the nucleosynthesis of ^{22}Na and should be included in the library of the reaction rates for novae.

B. The Reaction Rate for ^{17}F(p,γ)^{18}Ne

The ANCs of the low-lying states in ^{18}Ne are determined from those of their corresponding states in the mirror nucleus ^{18}O, using a procedure identical to the one explained in the previous section. A slight complication occurs from the fact that ^{23}Al is an even-N, odd-Z nucleus and, therefore, for our purposes its states are described as one proton coupled to an even-even core, while ^{18}Ne is an even-Z nucleus, and its states can have more than one proton orbital involved. Another difference is that there is more than one proton bound state in ^{18}Ne and direct radiative proton

capture can proceed via any and all of them. The orbitals we considered relevant for the 2-proton states in ^{18}Ne are $1d_{5/2}$, $2s_{1/2}$ and $1d_{3/2}$. Because the ground state of ^{17}F is $J^\pi = 5/2^+$ (almost pure $1d_{5/2}$), we are always interested only in final state configurations containing two protons of which one is in the $1d_{5/2}$ orbital. Therefore, the 0^+ ground state and the 4^+ second excited state at 3.38 MeV can only be made of $(1d_{5/2})^2_J$ configurations, but the two 2^+ excited states can be made of $(1d_{5/2}1d_{5/2})_{2^+}$ and $(1d_{5/2}2s_{1/2})_{2^+}$ contributions. The ANCs reported below reflect these assumptions and similarly the calculated astrophysical S-factors.

The ANCs obtained for the four proton bound states in ^{18}Ne from the ANCs of the corresponding states in the mirror ^{18}O nucleus are listed in Table VII. The binding energies included in the second column are calculated as $BE = S_p - E^*$. The ANC values are smaller than the calculated ANCs predicted in [72] and differ by a factor of 2-6 with other calculations using the same approach [97].

TABLE VII. The binding energies (B.E.), the proton orbitals, and the ANCs of the low-lying levels in ^{18}Ne.

J^π	B.E. (MeV)	Proton orbital	$C^2_{\ell j}$ (fm^{-1})
0^+_1	3.92	$d_{5/2}$	10.76±0.97
2^+_1	2.04	$d_{5/2}$	2.17±0.24
		$s_{1/2}$	14.29±1.71
4^+_1	0.54	$d_{5/2}$	2.17±0.22
2^+_2	0.31	$d_{5/2}$	2.69±0.32
		$s_{1/2}$	126.9±16.5

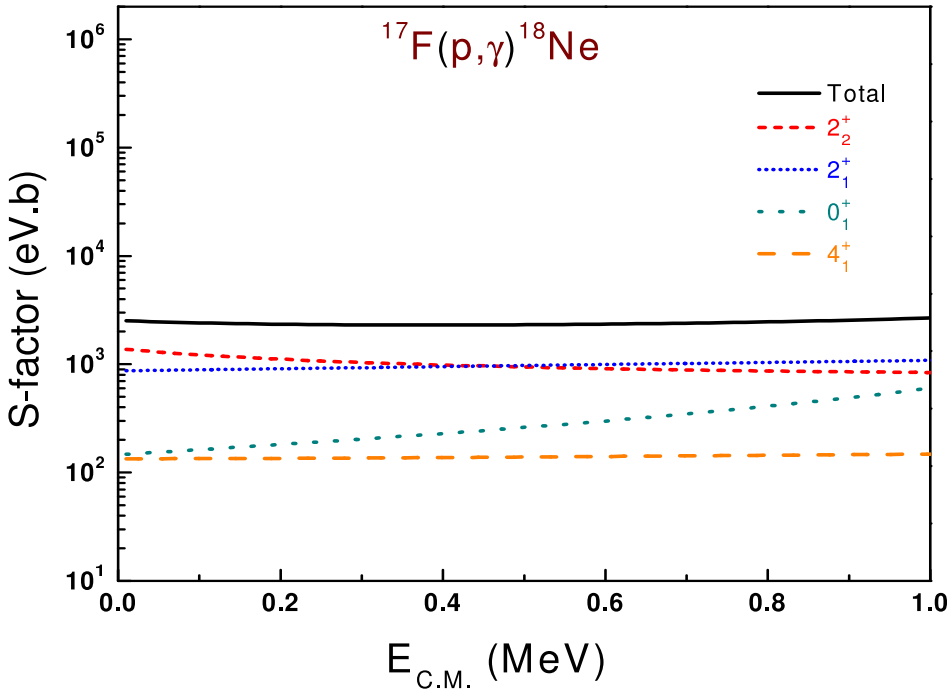

FIG. 68. The S-factor components of the ^{17}F$(p,\gamma)^{18}$Ne reaction. $S(0)$ of the $J^\pi = 2^+_2$ state makes the major contribution to the reaction rate, and is almost 50% larger than the 2^+_1 contribution. The other components are one order of magnitude smaller than the major one. The total $S(0) = 2.5 \pm 0.4$ keV b.

The astrophysical S-factors calculations for each (ℓ,j) configuration of Table VII were done depending on their corresponding ANCs. The geometry of the Woods-Saxon potential were fixed using $r_o = 1.25$ fm and $a = 0.65$ fm. Since the reaction rate for ^{17}F$(p,\gamma)^{18}$Ne in ONe novae is dominated by the direct capture terms, only the $E1$ electromagnetic transitions are included in the RADCAP calculations. The calculated S factors as functions of the C.M. energy for the $J^\pi = 0^+_1$, 2^+_1, 4^+_1, and 2^+_2 bound states of ^{18}Ne are plotted in Fig. 68, where $S(E)$ for the 2^+_1 and 2^+_2 states is the sum of their (dd) and (ds) components. It should be noted that the $(1d_{5/2}2s_{1/2})_{2^+}$ component contributes most in the proton capture. This is easy to understand due to the lack of a centrifugal barrier for the $2s_{1/2}$ orbital in the final state which extends further from

the core into the asymptotic region where the proton capture happens. The figure shows that the transitions to $J^\pi = 2^+_{1,2}$ dominate the direct capture reaction rate over the other contributions. The $J^\pi = 2^+_2$ state makes the larger contribution at $E < 400$ keV. The dependence of the total S factor (in keV b) on E (in MeV) is well fit by

$$S(E) = 2.5 - 1.11E + 1.55E^2 - 0.31E^3. \tag{5.8}$$

The value of the S factor at zero energy is $S(0) = 2.5 \pm 0.4$ keV b. This value is in good agreement with $S(0) = 2.9 \pm 0.4$ keV b reported in [67] and is smaller than $S(0) = 3.5$ keV b calculated in [72]. Using the central energy of the Gamow peak for $p + {}^{17}\mathrm{F}$, $E_o = 0.52T_9^{2/3}$ MeV, then substituting $S(E)$ in Eq. (2.20), we find

$$S_{eff}\left(T_9\right) = 2507\left[1 + 0.02T_9^{1/3} - 0.23T_9^{2/3} - 0.09T_9 + 0.17T_9^{4/3} + 0.07T_9^{5/3}\right],$$

where $S_{eff}(T_9)$ is in eV b. Then, using $\tau = \frac{18.03}{T_9^{1/3}}$, the estimated direct capture reaction rate for $^{17}\mathrm{F}(p,\gamma)^{18}\mathrm{Ne}$ is given by

$$N_A\left\langle\sigma v\right\rangle = 51\tau^2 S_{eff}\left(T_9\right)e^{-\tau} \quad \left[\frac{\mathrm{cm}^3}{\mathrm{mole}\cdot\mathrm{s}}\right]. \tag{5.9}$$

The total direct capture rate is plotted in Fig. 69. The uncertainty in the reaction rate is dominated by the 20% overall uncertainty of the extracted ANCs.

This is the first time to evaluate the direct capture reaction rate of $^{17}\mathrm{F}(p,\gamma)^{18}\mathrm{Ne}$ through the measurement of the ANCs in the mirror nuclear system. Previous estimates by García were determined using shell model calculations and spectroscopic factors measured in the $^{17}\mathrm{O}(p,\gamma)$ direct capture reaction [67]. On the other hand, the transitions through the resonance states $J^\pi = 1^-$ ($E_r = 595, \Gamma_\gamma = 1.5 \times 10^{-5}$), 3^+ ($E_r = 600, \Gamma_\gamma = 2.5 \times 10^{-5}$), and 0^+ ($E_r = 666, \Gamma_\gamma = 1.0 \times 10^{-5}$) in ^{18}Ne, where all the numbers are in units of keV and adopted from Ref. [71], are also important

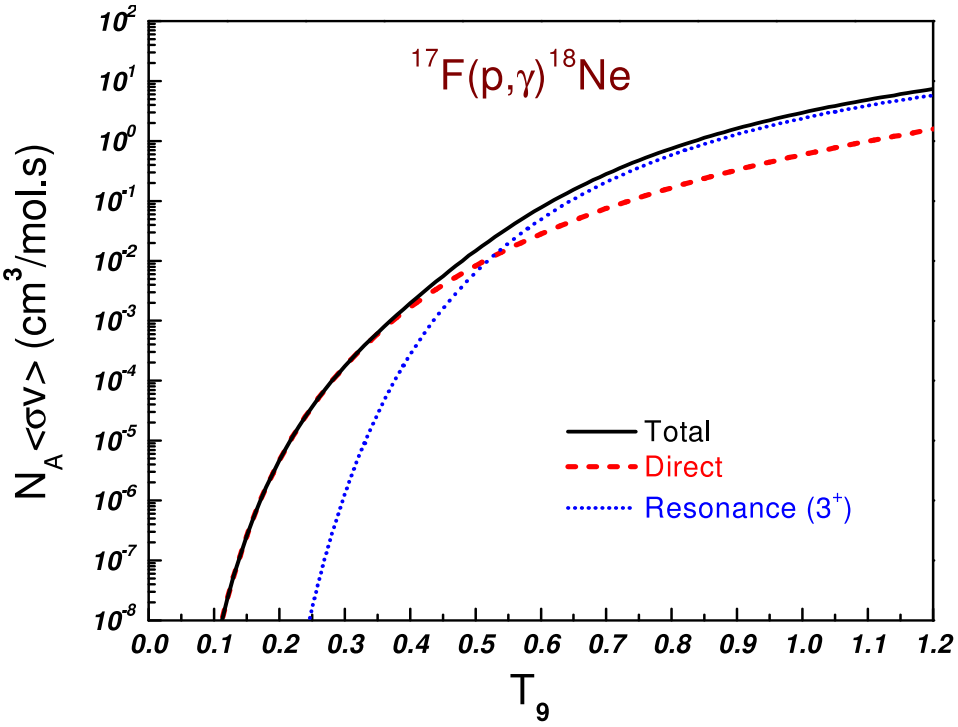

FIG. 69. The (black) solid line represents the total rate for the ^{17}F(p,γ)^{18}Ne reaction. The direct capture reaction, (red) dashed line, is estimated using the extracted ANCs for the low-lying states in ^{18}Ne and the determined S-factor, while the (blue) dotted line shows the contribution from the resonant 3^+ state in ^{18}Ne. The partial width and the resonant energy of the state were taken from Bardayan et al. [69].

in understanding the HCNO cycle. The resonant contributions are calculated using Eq. (2.24). The contribution of the 3^+ resonance, which is the major component, is plotted in Fig. 69 to compare it with the direct capture reaction rate. The present results show that the thermonuclear reaction rate is dominated by the direct capture component by a factor up to 10^4 over the resonant contribution for $T_9 = 0.2$-0.4. The resonant contribution is more significant for temperatures in excess of $T_9 \approx 0.5$ that characterize X-ray bursts or neutron stars.

The astrophysical implications of our direct capture reaction on the nucleosynthesis of the HCNO cycle materials can be explained following the approach that is discussed in Ref. [102] for 1.25 $M_\odot$ and 1.35 $M_\odot$ ONe WD novae. For temperatures less than $T_9 = 0.4$, two main hypotheses for the ^{17}F(p,γ)^{18}Ne reaction may affect the synthesis of ^{18}F. If the reaction is fast, ^{18}F will be produced in a large amount in the outer zone of the WD envelope, where the low temperatures decrease the probability of its destruction via ^{18}F(p,α)^{15}O, and in small fractions in the lower and hotter zone of the envelope. If the reaction is slow, more ^{18}F will be produced in the hotter zone via the ^{17}F($\beta\nu$)^{17}O(p,γ)^{18}F and ^{17}F(p,γ)^{18}Ne($\beta\nu$)^{18}F reaction paths. This will lead to larger amounts of ^{18}F overall, but under the same conditions the high temperature of the zone speeds up its destruction and increases the abundance of ^{15}O by almost 62% [102]. Therefore, the slow ^{17}F(p,γ)^{18}Ne rate dominates the synthesis of ^{18}F. The slow rate also allows more production of ^{17}F and its β-decay daughter ^{17}O.

Our direct reaction rate is on average 12% lower than the García [67] and Bardayan [71] calculations for temperatures less than $T_9 = 0.4$. The $\pm$20% uncertainty covers the central values of the previous calculations, but it is more important because it is evaluated from measured values that provide a significant reduction in the uncertainty of the rate. The astrophysical analysis by Parete-Koon [102] implies that the new rate of ^{17}F(p,γ)^{18}Ne is slow. This allows more production of ^{18}F to occur in the envelope and increases the possibility of its observation. As a consequence, the abundance of ^{18}O will be slightly increased.

When the mass of the WD increases from 1.25 $M_\odot$ to 1.35 $M_\odot$, the temperature of its inner zone drops from $T_9 = 0.46$ to $T_9 = 0.01$ in less than a minute [102], whereas it needs five minutes in the case of a 1.25 $M_\odot$ WD. This fast change indicates that

our rate will produce less ^{18}F and ^{18}O in comparison with García and Bardayan. But the mass fractions of the production of ^{17}F and ^{17}O will increase.

C. Conclusion

The asymptotic normalization coefficient technique has been used to determine the reaction rates for ^{17}F(p,γ)^{18}Ne and ^{22}Mg(p,γ)^{23}Al and to investigate their astrophysical consequences on the nucleosynthesis of ^{18}F and ^{22}Na in ONe WD novae. The experimental difficulties of the direct measurements when radioactive beams or targets are involved have been avoided by measuring the ANCs in the mirror systems. Charge symmetry implies that the spectroscopic factors of the pairs of mirror nuclei {^{18}Ne,^{18}O} and {^{23}Al,^{23}Ne} are the same. Therefore, the stable beam and target experiments ^{13}C(^{17}O, ^{18}O)^{12}C and ^{13}C(^{22}Ne, ^{23}Ne)^{12}C have been performed to extract the ANCs of the low-lying states in ^{18}O and ^{23}Ne. The results have then been applied to the corresponding states in ^{18}Ne and ^{23}Al, respectively.

In the procedure described above, the ANC of ^{13}C, which represents the other vertex in the above neutron transfer experiments, must be known. Therefore, we carried out the neutron-exchange reaction ^{13}C(^{12}C, ^{13}C)^{12}C to extract the ANC for the ground state in ^{13}C. This peripheral exchange reaction has been chosen because it has identical entrance and exit channels. The analysis has been done in the framework of the phenomenological optical model potential, where the measured elastic scattering angular distributions have been fit with Woods-Saxon potentials to obtain the optical model parameters. The OMPs were then used in the DWBA codes to predict the angular distribution for the transfer of a $1p_{1/2}$ neutron to a $1p_{1/2}$ orbital. Our ANC agrees within one sigma with the average of all previous measurements. We combine

it with them to get $C^2_{p_{1/2}}(^{13}\mathrm{C})$=2.31 $\pm$ 0.08 fm^{-1}, the value we use in the analysis of the other neutron transfer reactions.

We have successfully populated the $J^\pi = \frac{5}{2}^+$ ground state and the $J^\pi = \frac{1}{2}^+$ first excited state of ^{23}Ne in the neutron transfer reaction $^{13}\mathrm{C}(^{22}\mathrm{Ne}, ^{23}\mathrm{Ne})^{12}\mathrm{C}$. The ANCs $C^2_{d_{5/2}}(^{23}\mathrm{Ne}) = 0.86 \pm 0.08$ fm^{-1} and $C^2_{s_{1/2}}(^{23}\mathrm{Ne}) = 18.2 \pm 1.8$ fm^{-1} are used to determine their corresponding ANCs in ^{23}Al. The value $C^2_{d_{5/2}}(^{23}\mathrm{Al}) = (1.25 \pm 0.14) \times 10^4$ fm^{-1} is involved in determining the S-factor for the $^{22}\mathrm{Mg}(p,\gamma)^{23}\mathrm{Al}$ reaction, which gives $S_{1-22}(0) = 0.961 \pm 105$ eV b. Then it is used with $C^2_{s_{1/2}}(^{23}\mathrm{Al}) = (2.94 \pm 0.35) \times 10^6$ fm^{-1} to determine the partial width of the resonant state. The estimated capture reaction rate, which is the sum of the direct and resonant contributions, is higher in this work than in previous estimates, but it compensates only for a small amount of the lost production of ^{22}Na in ONe novae. It is concluded that the radioactive proton capture by ^{22}Mg overcomes its β-decay only in massive novae M $\approx$ 1.35 M$_\odot$, where extreme temperature and density conditions may occur.

The elastic scattering for $^{13}\mathrm{C}+^{17}\mathrm{O}$ and $^{18}\mathrm{O}+^{12}\mathrm{C}$ were successfully performed to obtain the OMPs that give the best description of the input and exit channels of the $^{13}\mathrm{C}(^{17}\mathrm{O}, ^{18}\mathrm{O})^{12}\mathrm{C}$ reaction. Yields of the four lowest-lying levels of ^{18}O in the neutron transfer reaction were disentangled. Shell model calculations were taken into account to determine the right configurations and the ANCs of the $J^\pi = (0^+_1, 2^+_1, 4^+_1, 2^+_2)$ states in ^{18}O. Then, they were used to obtain their corresponding ANCs in ^{18}Ne to determine the astrophysical S-factor. We found $S_{1-17}(0) = 2.5 \pm 0.4$ keV b and showed that the reaction rate of $^{17}\mathrm{F}(p,\gamma)^{18}\mathrm{Ne}$ is dominated by direct capture to the 2^+_2 and 2^+_1 states in ^{18}Ne. This is the first time to evaluate the direct capture reaction using measured asymptotic normalization coefficients. In comparison with the previous calculations,

our reaction rate is slower. Models of ONe novae imply that ^{17}F(p,γ)^{18}Ne is the main process that produces ^{18}F, and its abundance is enhanced in 1.25 $M_{\odot}$ novae when the reaction is slow. This supports overabundance observations of ^{17}O and ^{18}O in novae.

It has been shown that estimating reaction rates through measurements of ANCs in the mirror nuclear systems can be done. Our results agree within uncertainties with other measured and calculated results. Therefore, they can be inserted into the nuclear reaction rate library to study their influence on the abundance of the CNO, NeNa, and MgAl materials in novae.

More secrets and wonders about the nucleosynthesis of elements in the universe will be revealed with the improvement of the radioactive beam facilities and the future observations of the international γ-ray astrophysical laboratory. In the meantime, we keep looking to the sky above us, inspiring how it was made and adorned, and discovering its beauty.

REFERENCES

[1] R. A. Alpher, H. Bethe, and G. Gamow. Phys. Rev. **73**, 803 (1948).

[2] J. Bernstein, L. S. Brown, and G. Feinberg, Rev. Mod. Phys. **61**, 25 (1989).

[3] D. N. Schramm, and M. S. Turner, Rev. Mod. Phys. **70**, 303 (1998).

[4] J. Yang, M. S. Turner, G. Steigman, D. N. Schramm, and K. A. Olive, Astrophys. J. **281**, 493 (1984).

[5] A. Kashlinsky, and M. J. Rees, Mon. Not. R. Astr. Soc. **205**, 955 (1983).

[6] B. J .Carr, J. R. Bond, and W. D. Arnett, Astrophys. J. **277**, 445 (1984).

[7] A. Heger, and S. E. Woosley, Astrophys. J **567**, 532 (2002).

[8] J. N. Bahcall, *Solar Modeling* (World Scientific, Singapore, 1994).

[9] C. E. Rolfs, and W. S. Rodney, *Cauldrons in the Cosmos* (University of Chicago Press, Chicago, 1988).

[10] P. Gil-Pons, and E. García-Berro, Astron. Astrophys. **375**, 87 (2001).

[11] B. W. Carroll, and D. A. Ostlie, *An Introduction to Modern Astrophysics* (W. W. Norton and Company, New York, 1994).

[12] J. José, and M. Hernanz, Nucl. Phys. A **621**, 491 (1997).

[13] M. A. Garlic, http://www.space-art.co.uk. Image copyright and courtesy M. A. Garlic. (Accessed: August 2006).

[14] R. D. Gehrz, J. W. Truran, R. E. Williams, and S. Starrfield, Publ. Astron. Soc. Pac. **110**, 3 (1998).

[15] S. A. Glasner, E. Livne, and J. W. Truran, Astrophys. J. **475**, 754 (1997).

[16] S. Wanjo, M. Hashimoto, and K. Nomoto, Astrophys. J. **523**, 409 (1999).

[17] R. K. Wallace, S. E. Woosley, Astrophys. J. Supp. **45**, 389 (1981).

[18] H. A. Bethe, Phys. Rev. **55**, 434 (1939).

[19] D. D. Clayton, *Principles of Stellar Evolution and Nucleosynthesis* (The Univeresity of Chicago Press, Chicago, 1983).

[20] J. C. Blackmon, D. W. Bardayan, C. R. Brune, F. Carstoiu, A. E. Champagne, *et al.*, Nucl. Phys. A **746**, 365c (2004).

[21] J. José, and M. Hernanz, Astrophys. J. **494**, 680 (1998).

[22] P. M. Endt, Nucl. Phys. A. **251**, 1 (1990).

[23] C. Rowland, C. Illiadis, A. E. Champagne, C. Fox, J. José, and R. Runkle, Astrophys. J. **615**, L37 (2004).

[24] M. Livio, and J. W. Truran, Astrophys. J. **425**, 797 (1994).

[25] A. F. Iyudin, O. Reimer, K. Bennett, H. Bloemen, W. Hermsen, G. Kanbach, M. Phol, J. Ryan, V. Schönfelder, and A. Strong, Astron. Astrophys. **300**, 422 (1995).

[26] S. Bishop, R. E. Azuma, L. Buchmann, A. A. Chen, M. L. Chatterjee, *et al.*, Phys. Rev. Lett. **90**, 162501 (2003).

[27] S. Seuthe, C. Rolfs, U Schröder, W. H. Schulte, E. Somorjai, *et al.*, Nucl. Phys. A. **514**, 471 (1990).

[28] M. Wiescher, J. Görres, B. Sherrill, M. Mohar, J. S. Winfield, and B. A. Brown, Nucl. Phys. A. **484**, 90 (1988).

[29] J. José, A. Coc, and M. Hernanz, Astrophys. J. **520**, 347 (1999).

[30] M. Hernanz, J. José, A. Coc, J. Gomez-Gomar, and J. Isern, Astrophys. J. **526**, L197 (1999).

[31] A. Coc, M. hrenanz, J. José, and J. Thibaud, Astron. Astrophys. **357**, 561 (2000).

[32] C. Iliadis, A. Champagne, J. José, S. Starrfield, and P. Tupper, Astrophys. J. Supp. **142**, 105 (2002).

[33] W. A. Fowler, G. R. Caughlan, and B. A. Zimmerman, Ann. Rev. Astr. Ap. **5**, 525 (1967).

[34] J. M. Blatt and V. F. Weisskoph, *Theoretical Nuclear Physics* (Dover Publications, INC, Mineola, NY, 1991).

[35] G. Baur, C. A. Bertulani, and H. Rebel, Nucl. Phuys. A **458**, 188 (1986).

[36] G. Baur, Phys. Lett. B **178**, 135 (1986).

[37] H. M. Xu, C. A. Gagliardi, R. E. Tribble, A. M. Mukhamedzhanov, and N. K. Timofeyuk, Phys. Rev. Lett **73**, 2027 (1994).

[38] N. K. Glendenning, *Direct Nuclear Reaction* (Academic Press, INC, New York, 1983).

[39] R. D. Woods and D. S. Saxon, Phys. Rev. **95**, 577 (1954).

[40] M. A. Melkanoff, J. S. Nodvic, D. S. Saxon, and R. d. Woods, Phys. Rev. **106**, 793 (1957).

[41] F. Carstoiu and R. J. Lombard, Ann. Phys. **86**, 262 (1992).

[42] X. Campi and D. W. L. Sprung, Nucl. Phys. A **194**, 401 (1972).

[43] J. P. Jeukenne, A. Lijeune and C. Mahaux, Phys. Rev. C **16**, 80 (1977).

[44] E. Bauge, J. P. Delaroche, and M. Girod, Phys. Rev. C **58**, 1118 (1998).

[45] F. Carstoiu, L.Trache, R. E. Tribble, and C. A. Gagliardi,Phys. Rev. C **70**, 054610 (2004).

[46] L. Trache, A. Azhari, H. L. Clark, C. A. Gagliardi, Y.-W. Lui, A. M. Mukhamedzhanov, R. E. Tribble, and F. Carstoiu, Phys. Rev. C **61**, 024612 (2000).

[47] A. M. Mukhamedzhanov, H. L. Clark, C. A. Gagliardi, Y.-W. Lui, L. Trache, *et al.*, Phys. Rev. C **56**, 1302 (1997).

[48] A. M. Mukhamedzhanov, C. A. Gagliardi, R. E. Tribble, Phys. Rev. C **63**, 024612 (2001).

[49] R. M. DeVries, Phys. Rev. C **8**, 951 (1973).

[50] C. A. Gagliardi, R. E. Tribble, A. Azhari, H. L. Clark, Y.-W. Lui, *et al.*, Phys. Rev. C **59**, 1149 (1999).

[51] M. Wiescher, J. Görres, F.-K. Thielemann, and H. Ritter, Astron. Astophys. **160**, 56 (1986).

[52] M. Wiescher, J. Görres, B. Sherrill, M. Mohar, J. S. Winfield, and B. A. Brown, Nucl. Phys. A **484**, 90 (1988).

[53] J. A. Caggiano, D. Bazin, W. Benenson, B. Davis, R. Ibbotson, *et al.*, Phys. Rev. C **64**, 025802 (2001).

[54] X. Z. Cai, H. Y. Zhang, W. Q. Shen, Z. Z. Ren, J. Feng, *et al.*, Phys. Rev. C **65**, 024610 (2002).

[55] V. E. Iacob, Y. Zhai, T. Al-Abdullah, C. Fu, J. C. Hardy, N. Nica, H. I. Park, G. Tabacaru, L. Trache, and R. E. Tribble, Phys. Rev. C **74**, 045810 (2006).

[56] A. Ozawa, K. Matsuta, T. Nagatomo, M. Mihara, K. Yamada, *et al.*, Phys. Rev. C **74**, 021301 (2006).

[57] T. Gomi, T. Motobayashi, K. Yoneda, S. Kanno, N. Aoi, *et al.*, Nucl. Phys. A **718**, 508c (2003).

[58] L. Trache, F. Carstoiu, C. A. Gagliardi, and R. E. Tribble, Eur. Phys. J. A 27, Suppl. **1**, 237 (2006).

[59] N. K. Timofeyuk and P. Descouvemont, Phys. Rev. C **71**, 064305 (2005).

[60] N. Timofeyuk, D. Baye, and P. Descouvemont, Nuc. Phys. A **620**, 29 (1997).

[61] X. D. Liu, M. A. Famiano, W. G. Lynch, M. B. Tsang, and J. A. Tostevin, Phys. Rev. C **69**, 064313 (2004).

[62] M. B. Tsang, J. Lee, and W. G. Lynch, Phys. Rev. Lett **95**, 222501 (2005).

[63] B. A. Brown and B. H. Wildenthal, Nucl. Data. Tab. **33**, 347 (1985).

[64] P. Mohr, H. Herndl, and H. Oberhummer, Phys. Rev. C **55**, 1591 (1997).

[65] N. K. Timofeyuk and P. Descouvemont, Phys. Rev. C **72**, 064324 (2005).

[66] M. Wiescher, J. Görres, and F.-K. Thielemann, Astophys. J. **326**, 384 (1988).

[67] A. García, E. G. Adelberger, P. V. Magnus, D. M. Markoff, K. B. Swartz, *et al.*, Phys. Rec. C **43**, 2012 (1991).

[68] R. Sherr and H. F. Fortune, Phys. Rev. C **58**, 3292 (1998).

[69] D. W. Bardayan, J. C. Blackmon, C. R. Brune, A. E. Champagne, A. A. Chen, *et al.*, Phys. Rev. Lett. **83**, 45 (1999).

[70] Y. Parpottas, S. M. Grims, S. Al-Quraishi, C. R. Brune, T. N. Massey, J. E. O'Donnell, J. E Oldendick, A. Salas, and R. T. Wheeler, Phys. Rev. C **72**, 025802 (2005).

[71] D. W. Bardayan, J. C. Blackmon, C. R. Brune, A. E. Champagne, A. A. Chen, *et al.*, Phys. Rev. C **62**, 055804 (2000).

[72] M. Dufour and P. Descouvemont, Nucl. Phys. A **730**, 316 (2004).

[73] R. Moreh and T. Daniels, Nucl. Phys. **74**, 403 (1965).

[74] T. K. Li, D. Dehnhard, Ronald E. Brown, and P. J. Ellis, Phys. Rev. C **13**, 55 (1976).

[75] D. H. Youngblood and J. D. Bronson, Nucl. Instrum. Methods Phys. Rev A **361**, 37 (1994).

[76] D. M. Pringle, W. N. Catford, J. S. Winfield, D. G. Lewis, N. A. Jelley, K. W. Allen, and J. H. Coupland, Nucl. Instrum. Methods Phys. Rev A **245**, 230 (1986).

[77] S. Kowalski and H. A. Enge, computer code RAYTRACE (unpublished), University of Oxford, England, UK, 1986.

[78] D. H. Youngblood, Y.-W. Lui, H. L. Clark, P. Oliver, and G. smiler, Nucl. Instrum. Methods Phys. Rev A **361**, 539 (1995).

[79] J. S. Winfield, D. M. Pringle, W. N. Catford, D. G. Lewis, N. A. Jelley, and K. W. Allen, Nucl. Instrum. Methods Phys. Rev A **251**, 297 (1986).

[80] J. F. Ziegler, computer code TRIM (unpublished), http://www.srim.org, 1998.

[81] F. Carstoiu, computer code OPTIMINIX (unpublished), Institute of Physics and Nuclear Engineering, Bucharest, Romania, 1996.

[82] M. Rhoades-Brown, M. McFarlane, and Steven Pieper, Phys. Rev. C **21**, 2417 (1980); **21**, 2436 (1981).

[83] G. R. Satchler and Dao T. Khoa, Phys. Rev. C **55**, 285 (1997).

[84] J. G. Cramer and R. M. DeVries, Phys. Rev. C **22**, 91(1980).

[85] D. M. Brink and N. Takigawa, Nucl. Phys. A **279**, 159 (1977).

[86] G. R. Satchler, *Direct Nuclear Reaction* (Oxford University Press, New York, 1983).

[87] I. J. Thompson, Comput. Phys. Reb. **7**, 167 (1988).

[88] F. Delaunay, F. M. Nunez, W. G. Lynch, and M. B. Tsang, Phys. Rev. C **72**, 014610 (2005).

[89] H. P. Gubler, G. R. Platner, I. Sick, A. Traber, and W. Weiss, Nucl. Phys. A **284**, 114 (1977).

[90] A. M. Mukhamedzhanov and N. Timofeyuk, Sov. J. Nucl. Phys. **51**, 431 (1990) [Yad. Fiz. 51, 679 (1990)].

[91] J. Raynal, Phys. Rev. C **23**, 2571 (1981).

[92] S. Raman, C. W. Nestor, JR., P. Tikkanen, Atom. Data. and Nucl. Data. Tab. **78**, 1 (2001).

[93] F. M. Nunez and D. Y. Pang, private communication, NSCL, Michigan State University, September 2005.

[94] J. Cook, M. N. Stephens, and K. W. Kemper, Nucl. Phys. A **466**, 168 (1987).

[95] L. Trache, A. Azhari, H. L. Clark, C. A. Gagliardi, Y.-W. Lui, A. M. Mukhamedzhanov, R. E. Tribble, and F. Carstoiu, Phys. Rev. C **58**, 2715 (1998).

[96] R. L. Lawson, F. J. D. Serduke, and H. F. Fortune, Phys. Rev. C **14**, 1245 (1976).

[97] N. K. Timofeyuk, private communications, Department of Physics, University of Surry, England, UK, November 2006.

[98] C. A. Bertulani, Comp. Phys. Comm. **156**, 123 (2003).

[99] H. Schatz, J. Görres, H. Herndl, N. I. Kaloskamis, E. Stech, *et al.*, Phys. Rev. Lett **79**, 3845 (1997).

[100] L. Trache, A. Azhari, F. Carstoiu, H. L. Clark, Y.-W. Lui, A. Mukhamedzhanov, X. Tang, N. Timofeyuk, and R. E. Tribble, Phys. Rev. C **67**, 062801(R) (2003).

[101] J. José and M. Hernanz, Eur. Phys. J. A **27**, 107 (2006).

[102] S. Parete-Koon, W. R. Hix, M. S. Smith, S. Starrfield, D. W. Bardayan, M. W. Guidry, and A. Mezzacappa, Astophys. J. **598**, 1239 (2003).

VITA

Tariq Al-Abdullah was born in Kuwait in 1973. He recieved a Ph.D. in physics from Texas A&M University (TAMU) (2007). He holds a M.S. in physics from Yarmouk University (1998) and a B.S. in physics (major) and computer science (minor) from Yarmouk University (1995). Previously, he worked as a high school teacher(1995-1996), a teaching assistant in Yarmouk and JUST universities (1996-1998), a researcher in the Forensic Laboratory (1998-1999), and a teaching assistant in the Hashemite University (1999-2001).

Al-Abdullah is a member of the American Physics Society (APS). He attended and gave talks at the APS meetings in Chicago, IL 2004; Tampa, FL 2005; Maui, HI 2005; Nashville, TN 2006; and Jacksonville, FL 2007. Tariq was awarded a scholarship from the Hashemite University to obtain his Ph.D. degree at TAMU (2001-2004). While pursuing his Ph.D., he was awarded a Robert A. Welch Foundation Graduate Assistant Research fellowship to do a research in the Cyclotron Institute at TAMU (2002-2007).

Tariq will serve as a faculty member in the Physics Department at the Hashemite University in Jordan. His permanent address is: Department of Physics, The Hashemite University, P.O. Box 150459, Zarqa 13115, Jordan. e-mail:abdullatq@yahoo.com.